eman ta zabal zazu

Universidad del País Vasco

Euskal Herriko Unibertsitatea

TRANSLOCATION AND BIOLOGICAL FATE OF ENGINEERED NANOMATERIALS WITH BIOMEDICAL APPLICATIONS FOR NANOSAFETY EVALUATION

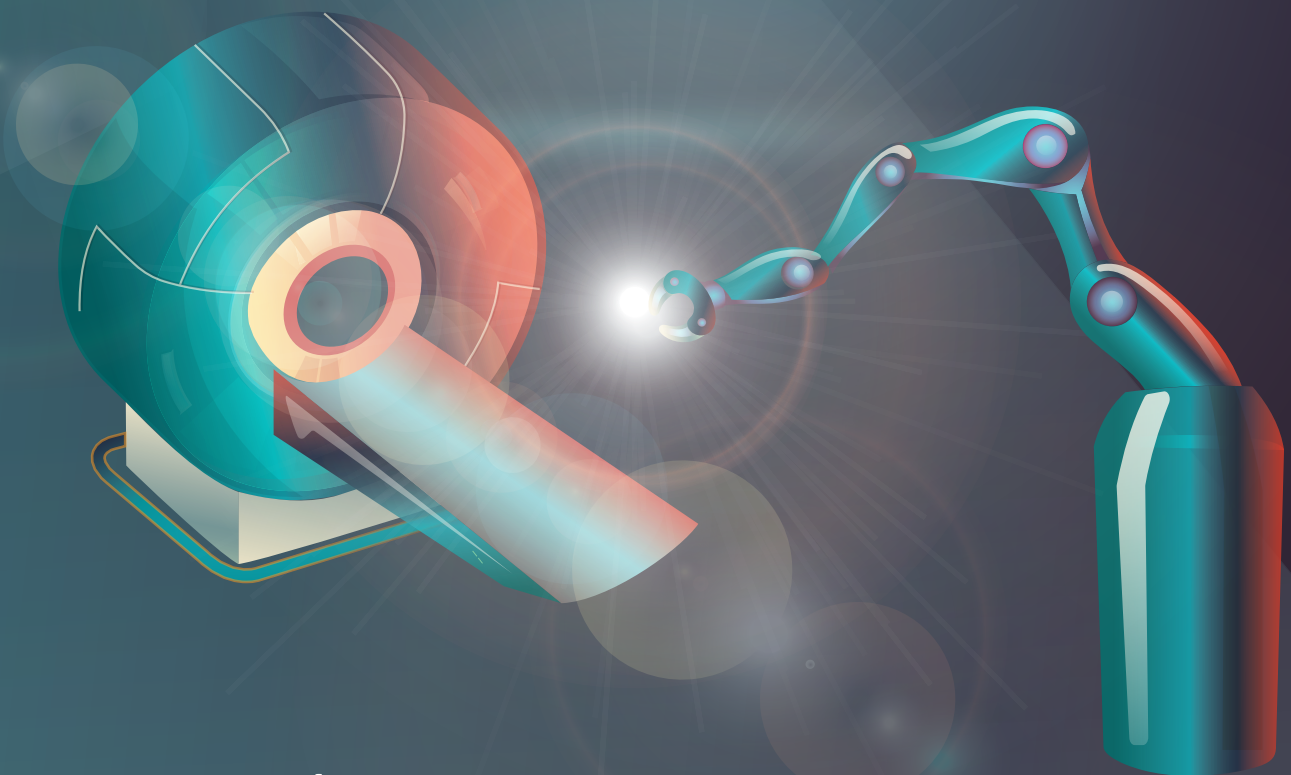

Ángel Manuel Martínez Villacorta

Tesis doctoral

2022

TRANSLOCATION AND BIOLOGICAL FATE OF ENGINEERED NANOMATERIALS WITH BIOMEDICAL APPLICATIONS FOR NANOSAFETY EVALUATION

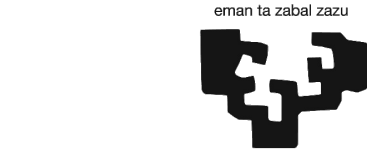

Universidad del País Vasco Euskal Herriko Unibertsitatea

Ángel Manuel Martínez Villacorta

Tesis Doctoral

2022

Dissertation presented to The Organic and Inorganic Chemistry Department of the University of the Basque Country (UPV/EHU) for the degree of Doctor in Synthetic and Industrial Chemistry, presented by Mr.

Ángel Manuel Martínez Villacorta

Thesis Supervisors from the Centre for Cooperative Research in Biomaterials:

CIC biomaGUNE MEMBER OF BASQUE RESEARCH & TECHNOLOGY ALLIANCE

Dr. Sergio Enrique Moya **&** **Dr. Jordi Llop Roig**

Soft Matter Nanotechnology Lab

Radiochemistry & Nuclear Imaging Lab

Tutor from the University of Basque Country (UPV/EHU), Department of Organic and Inorganic Chemistry, Faculty of Science and Technology:

Prof. Dr. María Esther Lete Expósito

Universidad del País Vasco

eman ta zabal zazu

Euskal Herriko Unibertsitatea

2022

The experimental part of this PhD thesis has been fully conducted in the Radiochemistry & Nuclear Imaging Lab. and the Soft Matter Nanotechnology Lab. at CIC biomaGUNE.

Mr. Ángel Manuel Martínez Villacorta has been funded by the Research Personnel Training grant BES-2014-070212 from the Ministry of Science, Innovation and Universities, entitled: "NanoFATE: Translocation, Biological Fate and Biointeractions of Engineered Nanoparticles with Biomedical Applications and for Nanosafety Evaluation."

"Where will wants not, a way opens"

J.R.R. Tolkien.

TABLE OF CONTENT

List of Acronyms

ACN	Acetonitrile	**O/W**	Oil in Water
ADME	Absorption, Distribution, Metabolism and Excretion	**OSEM**	Ordered Subset Expectation Maximization
API	Active Pharmaceutical Ingredient		
APTES	(3-Aminopropyl) triethoxysilane	**PAGE**	Polyacrylate gel electrophoresis
ATMP	Advanced Therapy Medicinal Product	**PBS**	Phosphate Buffer Saline
BDDCS	Biopharmaceutics Drug Disposition Classification System	**PC**	Protein Corona
BNCT	Boron Neutron Capture Therapy	**PEG**	Polyethylene glycol
BSA	Bovine Serum Albumin	**PEI**	Polyethyleneimine
COSAN	Cobaltabisdicarbollide	**PET**	Positron Emission Tomography
CT	X-ray Computed Tomography	**PGA**	Poly glycolic acid
CTAB	Hexadecyltrimethylammonium bromide	**PLA**	Poly lactic acid
DCM	methylene dichloride	**PLGA**	poly(D,L-lactic-*co*-glycolic) acid
DDS	Drug Delivery Systems	**PNPs**	Polymer Nanoparticles
DLS	Dynamic Light Scattering	**radio-TLC**	Radio Thin Layer Chromatography
EDXS	Energy Dispersive X-ray Spectroscopy	**RCC**	Radiochemical Conversion
EMA	European Medicines Agency	**RCF**	Relative Centrifugal Force
EPR	Enhanced Permeation Retention	**RCI**	Radiochemical Incorporation
ESE	Emulsification Solvent Evaporation	**RCP**	Radiochemical Purity
FBP	Filtered Back Projection	**RCY**	Radiochemical Yield
FDA	Food and Drug Administration	**RPM**	Rotations per minute
FT-IR	Fourier Transform Infrared	**SBF**	Simulated Body Fluid
GBM	Glomerular Basement Membrane	**SC**	Subcutaneous
IM	Intramuscular	**SDA**	Structure Director Agent
iTLC	Instant Tin-Layer Chromatography	**SDS**	Sodium dodecyl sulphate
IV	Intravenous	**SEM**	Scanning Electron Microscope
MCM	Mobil Composition of Matter	**SPE**	Solid Phase Extraction
MMD	Mass Median Diameter	**SPET**	Single Photon Emission Tomography
MMD	Mass Median Diameter	**TEM**	Transmission Electron Microscope
MPS	Mononuclear Phagocyte System	**TEOS**	Tetraethyl Orthosilicate
MSM	Mesoporous Silica Materials	**TFA**	Trifluoroacetic acid
NM	Nanomaterial	**TMOS**	Tetramethyl orthosilicate
NP	Nanoparticle	**W/O**	Water in Oil

I. Resumen

Desde hace décadas, los nuevos materiales con un tamaño en el rango del nanómetro (nanomateriales, NMs) han incrementado exponencialmente su presencia en casi todos los ámbitos de la vida cotidiana. Los NMs han demostrado tener gran potencial en numerosos ámbitos de aplicación, desde la medicina hasta la electrónica.

Concretamente en el ámbito de la medicina, se ha propuesto la utilización de los NMs como sistemas de liberación controlada de fármacos. Los NMs pueden prolongar la vida media biológica de determinados fármacos, conseguir su solubilización en medio fisiológico, aumentar su acumulación en órganos o tejidos de interés, e incluso liberar el fármaco en el tejido diana mediante la ayuda (o no) de estímulos internos o externos. Sin embargo, tanto por su naturaleza como por su tamaño, resulta tremendamente dificultoso evaluar la absorción, distribución, metabolismo y excreción (ADME) de los componentes de los NMs. Además, la interacción de los NMs con los fluidos biológicos es extremadamente compleja, tanto por el elevado número de moléculas interactuantes, como por la dinámica de las interacciones entre las biomoléculas y los NMs. Por ende, la encapsulación de los compuestos en sus transportadores dificulta la obtención de datos cuantitativos por las complejas interacciones fisicoquímicas entre los

componentes. Es por tanto necesario realizar diversas aproximaciones para obtener información relevante y significativa que pueda dar datos fiables acerca de la biodistribución, farmacocinética y destino biológico tanto del NM como del fármaco encapsulado.

En esta tesis doctoral se han realizado diferentes aproximaciones para determinar el destino biológico de los componentes de los nanotransportadores evaluados, incluyendo técnicas de microscopía óptica y electrónica, distintas espectroscopias y técnicas de imagen como la Tomografía de Emisión de Positrones (PET, del inglés *Positron Emission Tomography*) en combinación con otras técnicas de imagen como las Tomografía Computarizada (CT, del inglés *Computerised Tomography*). El trabajo llevado a cabo en la tesis se ha estructurado en tres capítulos que recogen los resultados experimentales (Capítulos 3, 4 y 5).

El **Capítulo 3** aborda la síntesis y el estudio de nanopartículas (NPs) poliméricas biodegradables (ver Figura 1). En primer lugar, se ha optimizado el proceso de síntesis de nanopartículas utilizando copolímeros de ácido láctico y glicólico en distintas ratios, evaluando el efecto que tiene la cantidad de compuesto encapsulado sobre las propiedades de los NMs y sobre el propio proceso sintético. Como modelo de fármaco hidrofóbico se utilizó el 1,2-dicarba-*closo*-dodecaborano, también conocido como *orto*-carborano, debido a su alto carácter hidrofóbico y a que el proceso para su marcaje ya había sido puesto a punto en una tesis doctoral anterior realizada en CIC biomaGUNE.

Para llevar a cabo el proceso de optimización de la síntesis de las NPs se aplicaron dos tipos de encapsulación (encapsulación por nano precipitación y emulsificación asistida por ultrasonido). Se varió la composición del compuesto hidrofóbico en el rango comprendido entre el 1 y el 20 %. Una vez optimizado el proceso sintético, se llevaron a cabo estudios de imagen nuclear para determinar cómo afecta el encapsulamiento del fármaco a su biodistribución tras

administración intravenosa y pulmonar. Para ello, se prepararon NPs cargadas con el fármaco marcado con el isótopo emisor de positrones flúor-18, y se efectuaron estudios PET-CT en animales sanos.

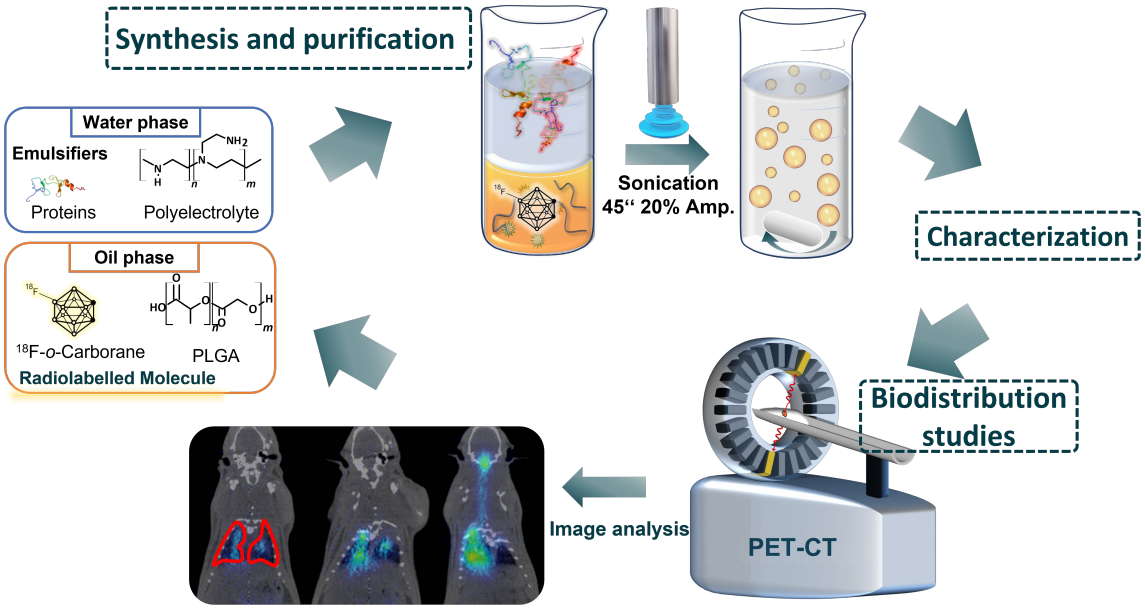

Figura 1. Esquema experimental del proceso de síntesis, caracterización y realización de los estudios de biodistribución de las NPs poliméricas.

Los resultados obtenidos mostraron que un aumento en la cantidad de *o*-carborano conlleva la formación de NPs de mayor tamaño, generando irregularidades en la estructura y aumentando la agregación de NPs con el tiempo. Así mismo, los estudios de imagen revelaron que las NPs de PLGA permiten la administración del fármaco marcado por ambas vías (intravenosa y pulmonar), si bien los estudios *in vivo* sugieren una liberación rápida del fármaco en ambos escenarios.

El **Capítulo 4** aborda el estudio de la interacción de las NPs poliméricas con las proteínas presentes en la sangre, y la posible formación y estabilidad de la corona de proteínas (en inglés, *Protein Corona*). Se evaluaron NPs de PLGA de 150 nm de tamaño hidrodinámico estabilizadas por medio de albúmina o polietilenimina utilizados como surfactantes en la síntesis (ver Figura 2).

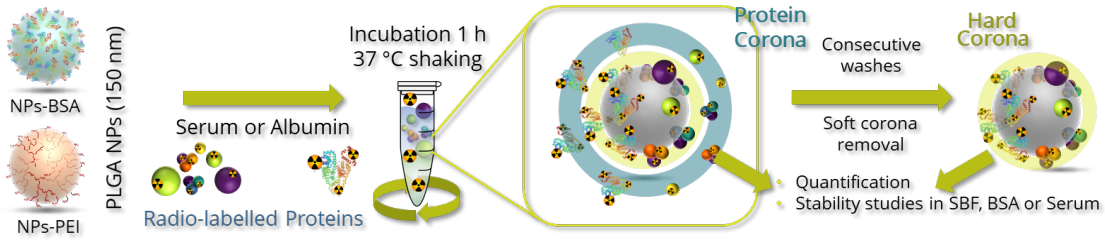

Figura 2. Esquema experimental del estudio de la formación de la corona de proteínas y los estudios de estabilidad llevados a cabo.

Para analizar la cantidad de proteína incorporada en las NPs y la estabilidad de la corona se optó por la incorporación del radioisótopo yodo-131 en los residuos tirosina de las proteínas. Los estudios confirmaron que la cantidad de proteínas agregadas sobre las partículas recubiertas de albúmina es hasta tres veces menor que la cantidad de proteína agregada sobre las NPs decoradas con polietilenimina. Los resultados corroboran que la corona que se forma sobre NPs cargadas positivamente (como son las NPs recubiertas con PEI) tienen una corona dura (en inglés *hard corona*) más estable y una mayor cantidad de proteínas en la corona, debido a las interacciones electrostáticas entre las NPs y las proteínas.

Seguidamente, se evaluó la formación de la corona de proteínas *in vivo*. Para ello, se abordó el marcaje de suero de ratón con fluor-18, utilizando para ello un grupo prostético capaz de reaccionar con aminas primarias. Posteriormente se inyectó en el animal para determinar la ventana temporal en la cual la concentración de actividad fuera constante en los órganos de interés. En un segundo estudio, se repitió el diseño experimental, pero se inyectaron NPs poliméricas unos minutos después de la administración del suero marcado, para determinar la interacción *in vivo* de las nanopartículas con el suero circulante. Los resultados experimentales no mostraron variaciones significativas que pudieran esclarecer las dinámicas de la formación de la corona de proteínas *in vivo*.

En el **Capítulo 5** se abordó la evaluación de la degradación y destino biológico de un sistema de estructura híbrida ampliamente utilizado en diversos campos de investigación: nanopartículas mesoporosas de sílice (MSNs) estabilizadas en la superficie con moléculas de polietilenglicol y decoradas con un péptido en la superficie. Este último con afinidad por un receptor sobreexpresado en determinados tipos de cáncer. Se realizó la síntesis y caracterización de los materiales, mediante las técnicas habituales, incluyendo microscopía electrónica, termogravimetría, dispersión dinámica de luz y espectrometría de masas. Dicha caracterización mostró la formación de NPs con una matriz mesoporosa, con estructura continua bicúbica correspondiente con el grupo espacial $Ia\bar{3}d$. Las consiguientes funcionalizaciones mostraron la formación de la densa capa de polietilenglicol sobre la cual se conjugó el péptido director (en inglés, *targeting peptide*).

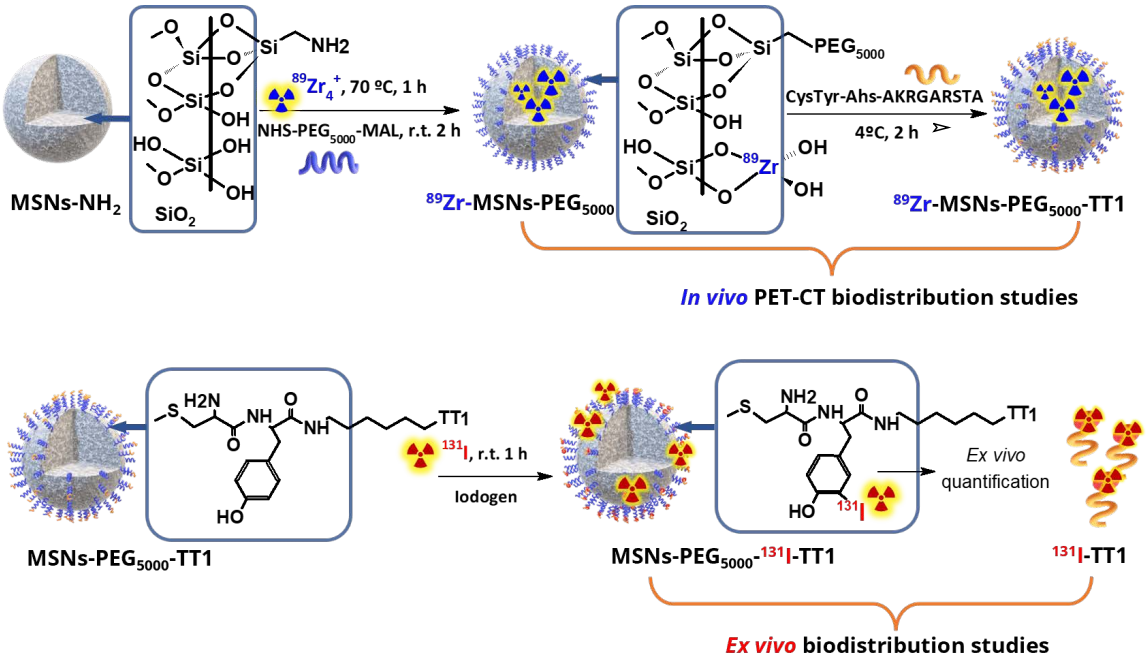

Figura 3. Esquema experimental de la funcionalización y el marcaje de las NPs de sílice mesoporosa para los estudios de biodistribución llevados a cabo.

Después de realizar la caracterización de los NMs se realizó un estudio de cultivos celulares en una línea tumoral, para comprobar si las moléculas

dispuestas en la superficie mejoran la interacción de las partículas en los cultivos celulares de manera específica.

Tras confirmar la especificidad de las partículas en la línea empleada de melanoma tumoral, se abordaron estudios de biodistribución *in vivo* utilizando para ello un modelo tumoral xerográfico, generado mediante inoculación subcutánea de células tumorales. Para poder llevar cabo los estudios de biodistribución, se utilizaros dos radioisótopos para marcar dos partes de los NMs, el interior y la superficie. El zirconio-89 se incorporó sobre la estructura porosa silícea; para realizar el marcaje de la superficie, se marcó el péptido con iodo-131 a través de un residuo tirosina (ver Figura 3).

Los resultados mostraron una elevada acumulación de MSNs en el hígado y el bazo, mientras que los productos de degradación de los MSNs se acumulan en los huesos o se eliminan por la orina. También demostraron que el péptido se desancla parcialmente de las MSNs y se elimina, lo cual, juntamente con la elevada acumulación en hígado, se traduce en una baja acumulación en el tumor, a pesar de la presencia del péptido.

II. Summary

In this PhD thesis the experimental part has been divided in three chapters (3 to 5). In **Chapter 3** we describe the preparation of PLGA NPs, loaded with *o*-carborane for subsequent radiolabelling, and stabilized either with BSA or PEI. The aim of this work was to evaluate the biodistribution and bioavailability of the o-carborane when encapsulated inside a hydrophobic but degradable PLGA matrix. Our results show that PLGA NPs can be successfully used to administrate the hydrophobic *o*-carborane intravenously and through the lungs. *In vivo* studies

carried out with positron emission tomography (PET) suggest a fast release of the encapsulated drug both after intravenous and pulmonary administration.

In **Chapter 4** we explored the use of radiolabelling and gamma counting to study the dynamic of the protein corona on nanoparticles differing in their surface charge and chemistry but with the same core chemistry, using gamma counting. Specifically, we evaluated the stability and exchangeability of radiolabelled proteins forming a hard and soft corona around BSA- and PEI-stabilised PLGA NPs (the corona formed either from pure albumin or from full plasma). BSA used as surfactant in the synthesis of the PLGA NPs is practically not exchanged by proteins from the media, neither for albumin nor for full plasma. The positively charged PEI binds larger amounts of protein resulting as well in a more stable hard corona around the NPs. PET imaging was not suitable to investigate the protein corona dynamics *in vivo*.

In **Chapter 5**, we investigated the biological fate of mesoporous nanoparticles (MSNs) modified with PEG and targeting peptide for directing the nanoparticles to the P32 protein, overexpressed in cancer tissue. This was done using PET imaging and a dual labelling approach, in which the core of the MSNs was labelled with ^{89}Zr, and the shell was labelled by incorporating ^{131}I into the chemical structure of the peptide. Despite the MSNs showed limited capacity to accumulate in the tumour, relevant information on the degradation of the nanocarriers and the stability of the targeting peptide around the nanoparticle could be obtained. MSNs tend to accumulate in lung, spleen, and liver but they degrade releasing ^{89}Zr or degradation species containing ^{89}Zr, which are either eliminated by the bladder or accumulate in bones. When the nanoparticles are labelled through the peptide, the biodistribution patters partially superpose with that of the core labelled MSNs and partially with the pattern of the free peptide, which proves that there is a detachment of the peptide from the nanoparticle. The

absence of activity in the bones for the experiments with the radiolabelled peptide corroborate that the activity at the bones is coming from the detachment of the ^{89}Zr and not because of the presence of nanoparticles there.

1. General Introduction

Nanotechnology is defined as the science, technology or engineering performed at the nanometre scale between 1 and 100 nm, at least in one of their dimensions.[1] The possibility to perform atom by atom manipulation was proposed in the 60's by the physicists Richard Feynman[2] and since then, the theoretical and technological development of nanomaterials (NMs) and their application has reached all areas of society. Although the ability to manipulate, see, and control the NMs at the atomic scale is quite recent, NMs have been used since the pre-modern era. For example, the presence of gold, silver and copper in the form of 60 to 100 nm sized nanoparticles (NPs) colloidally dispersed in the glass of the 4th century Lycurgus coup, produces a dichroic effect in the glass depending if the light is reflected or transmitted.[3] Another example is the hybrid composite made of the natural blue indigo organic pigment, entrapped in sepiolite channels of phyllosilicates, such as palygorskite and other clays used the by the Mayan[4–6] cultures in the 9th century. Over the last 40 years the scientific community has intensively explored nanosciences due the enormous potentiality that NMs can provide, from technological developments in electronics, catalysis, and energy, to biomedical applications such as the development of therapies for cancer or means for environmental remediation.

Nowadays, the Nanotechnology covers a wide variety of disciplines, including material science, physics, chemistry, etc.[7–9] The development of Nanotechnology and the continuously increasing number of nanotechnology-based products have raised concerns in the society about the possible negative impact of NMs on human health[10–13] and the environment[14–16]. One of the most rapidly expanding fields for application of Nanotechnology is bio(nano)medicine. Nanomedicine is the discipline that deals with the use of NMs as therapeutic tools to combat diseases and for the improvement of human health.[17–20] Nanomaterials offer the means to encapsulate (otherwise insoluble) drugs, to protect them from degradation during circulation, reduce toxicity, increase drug bioavailability and to direct drugs to specific tissues or cells, the so called targeted delivery. [21,22]

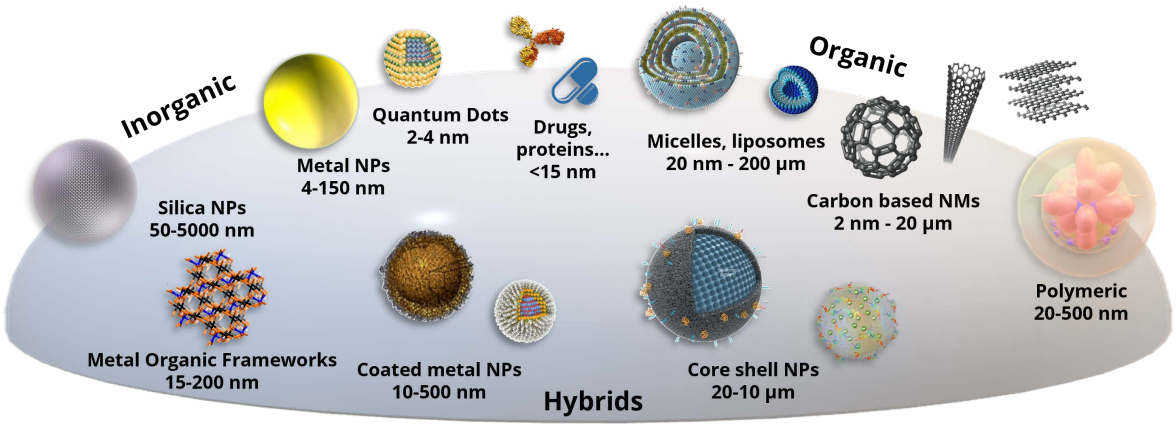

Figure 1.1. General classification figure based on their chemical nature of most published engineered nanomaterials.

NMs can be classified following two main aspects: composition and scale dimension. Regarding the chemical compositions, NMs can be broadly classified as inorganic, organic and hybrids or composite materials (Figure 1.1). In general terms, metallic inorganic NMs such as quantum dots and gold NPs show interesting optical, electrical, and catalytic properties. Mesoporous Silica NMs are an example of inorganic NMs that can be used as drug delivery systems

(DDS), because of their high porosity that allows the incorporation of a large variety of compounds in a high concentration, depending on the pore chemistry.

Organic NMs are the NMs most frequently used as DDS. Polymer based NMs have the ability to carry different compounds (with less cargo capacity than porous silica), and can be designed with high biocompatibility and to be degradable.[23]

The main drawback of using NMs for clinical application is the introduction of materials in the body, that the immune system of the body rapidly recognizes and combats, to finally eliminate via the reticuloendothelial system.[24] This fact reduces dramatically the capacity of the NM to accumulate in the target site and may lead to drug-release in off-target organs or tissues.[25–28] The liver and the spleen are organs rich in macrophages that remove the NMs from the bloodstream. The so-called opsonization process begins when the plasma proteins (60 to 80 mg mL^{-1}) deposit on the surface of the injected NMs forming the so-called protein corona (PC). Kupffer cells (reticular macrophages) located in blood vessels of the liver recognize the opsonin moieties onto the surface of the PC and NMs are endocytosed by the macrophages. There are different ways to avoid recognition by the immune system, e.g. by modifying NMs surface with polyethylene glycol (PEG) molecules (PEGylation), which reduce the deposition of proteins on the surface of the NMs surface.[29] Other alternatives to reduce NMs clearance and increase circulation are the use of coatings based on lipids,[30] carbohydrates,[31] proteins, and polypeptides,[32] polyglycerols,[33,34] acrylamides,[35–37] zwitterions,[38] and oxazolines,[39,40] among others.

Nowadays the gold standard in nanomedicine are the NMs based on biological molecules such as proteins, unibodies, micelles, liposomes, exosomes,

protocell, viral capsids, etc.[41–46] However, the main drawback of these NMs is the low stability *in vivo*, low cargo capacity and the poor chemical stability.

The fate of NMs, through different incorporation routes (gastrointestinal, respiratory, endotracheal, topical, sublingual, etc.) and their translocation are fundamental aspects for comprehending the possible mechanism of toxicological actions of NMs, and thinking in potential biomedical applications, to evaluate the capacity to target the selected organ and to transport encapsulated drugs to specific tissues

NMs can be administrated parenterally, topically, ocularly, or through the respiratory track. Once administered parenterally, NMs enter the blood torrent or the lymphatic system and reach specific tissues or organs, where they must pass endothelial barriers, and finally translocate through the cell membranes to reach the interior of the cells.

The complexity of the biological fluids which are in contact with NMs after administration to a living organism affects their aggregation and stability and modifies the biological properties through the formation of the PC. The interactions of NMs with biological molecules whether in the blood or in cells or organs, are highly dependent on the surface properties and composition of the NMs. Inside cells, they can degrade into their molecules. For example, inorganic NMs can be dissolved generating ions, negatively affecting the cell homeostasis systems. Besides, the surface of metal nanoparticles can be highly reactive, and can interfere with the cellular activity, behaving as oxidising/reducing agents. Organic NMs can degrade into molecular components. In the case of NMs made of synthetic biodegradable polymers, these can be hydrolysed in their monomers and removed by natural pathways, or the biopolymers that can be recycled through the cell machinery.

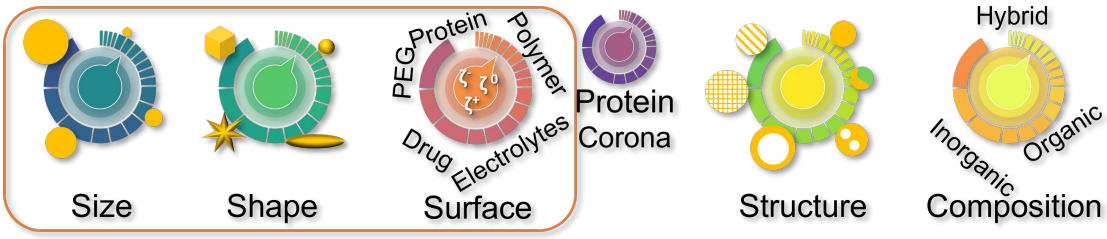

Figure 1.2. Scheme of tuneable physic-chemical properties of hybrid NMs. Some of their properties will determine the protein corona as a new evolving entity once administered to a living organism.

The combination of two or more components derives in hybrid NMs. Those are made with inorganic components such as metal/non-metallic ions, oxides, salts, sulphides, particles, clusters, and their derivatives in combination with organic components, such as organic compounds, ligands, polymers, polyelectrolytes, and drugs. Hybrid NMs play a paramount role in Nanotechnology. The ability to engineer with their properties at different shapes, scales and structures, from nano to macro scale, is the driving force for the active research in different fields (Figure 1.2). Especially, the development of platforms for drug delivery, diagnostics, stimuli-responsive materials, material science, energy and electronic applications, industrial technologies, sensors and so on.

The production of industrial-scale materials and their use in commercial products raises the exposure rate by increasing the amount of material that we can intake.[47] Therefore, the fate and translocation, through different adsorption routes (gastrointestinal, respiratory, endotracheal, topical, sublingual, etc.) and translocation is a fundamental aspect in comprehending the possible mechanism of toxicological actions of NMs, and in instance of their medical application, to evaluate the capacity to target the selected organ they have been engineered.

The NMs can translocate into the body crossing the epithelial barriers, although parenteral, topical, ocular, or respiratory are common administration routes. Once administered via parenteral route, they reach the blood torrent or

the lymphatic system and reach certain tissues or organs, where they must pass an endothelial barrier to enter cells. A major drawback of NMs is the impact of the complex biological fluid they are exposed in. When NMs are spread in the serum blood, a rapid electrostatic interaction with the surrounding protein involves the formation of the PC. Also salt content, temperature, flow, and pressure, produce interparticle aggregation, increasing size, changing the external charge, hydrophilicity, and oxidation state. Those changes have an impact on their biodistribution, changing the retention in different organs. All the changes produced due the biological environment, affect the intracellular trafficking, the toxicological action, localisation, and time retention at cellular and organ level.[48]

The study of the biological fate and the interaction of NMs with biomolecules, as well as their tracking at the cellular and systemic levels is a major challenge and must be approached by combining different experimental techniques.

1.1. Nanoparticles and Medicine

Nanomedicine is considered the medical application of Nanotechnology. It is an area of knowledge in which biology, engineering, chemistry, and medicine merge. Nanomedicine is focused on the design, synthesis, and development of nanomaterials to improve the diagnosis, the treatment and/or the monitoring of human diseases.

Nanomedicine is present in more than one hundred marketed products, and so many others are under clinical trials, covering a wide range of diseases and application routes (Table 1.1).[49–52]

Table 1.1 Nanomedicines approved by EMA during the last two decades

	API	Product Name®	Company	Ad. Route
Liposomes	Cytarabine	DepoCyt	Almac Pharma	Intrathecal
	Doxorubicin	Myocet	GP-Pharma	IV suspension
	Paclitaxel	Abraxane	Celgene	Oral suspension
	Morphine	DepoDur	Almac Pharma	Epidural
	Propofol	Diprivan/Propofol Lipuro/Propofol	Astra Zeneca	IV emulsion
	Mifamurtide	Mepact	Takeda	IV suspension
NPs	Hepatitis A	Epaxal	Crulcell	IV suspension
	^{90}Y-Ibritumomomab tiuxetan	Zevalin	Bayer Pharma	IV solution
Nanocomplex	Fermoxytol	Rienso	Takeda	IV solution
	Iron (III)-hydroxide dextran complex	Ferrisat/Cosmofer	Pharmacosmos	IV solution
	Iron sucrose	Visudyne	Novartis	IV solution
	Ferric carboxymaltose	Feriject	Vifor	IV solution
Virosome	Adjuvanted influenza vaccine	Inflexal V	Crucell	IV suspension
	Glatiramer·Glu, Ala, Tyr, Lys copolymer	Copaxone	Teva Pharmaceuticals	SC solution
Polymer-protein conjugate	Amphotericin B	AmBisome	Gilead Science	IV suspension
	CertolizumabPEGol · PEG-anti-TNFFab	Cimzia™	UCB Pharma	SC solution
	Methoxypolyethylene glycol-epoetinβ	Mircera	Roche Pharma	IV solution SC solution
	PEGfilgrastim · PEGrhGCSF	Neulasta	Amgen Tech.	SC solution
	PEG interferon α-2a	PEGasys	Roche Pharma	SC solution
	PEG interferon α-2b	PEGIntron	Schering-Plough	SC solution
	PEG-HGH antagonist	Somavert	Pfizer	SC solution
Emulsion	Cyclosporine	Norvir	Aesica Queenborough	Oral capsule
	PEGaspargase · mPEGasparaginase	Oncaspar	Sigma-tau Arzeimittel	IV solution IM solution
	Sevelamer	Renagel · Renvela	Genzyme	Oral tablet
Nanocrystals	Aprepitan	Emend	Merck	Oral capsule
	Fenofibrate	Tricor · Lipanthyl · Lipidil	Recipharm	Oral tablet
	Paliperidone	Xeplion	Janssen Pharma	IM solution
	Sirolimus	Rapamune	Pfizer	Oral tablet
	Olanzapine	Zypadhera	Lilly Pharma	Powder

1.2. Drug delivery systems: Nano-encapsulation

Conventional drug formulations present many advantages such as well-defined and scalable manufacturing protocols, full control of the process, reproducibility, and efficacy. Major advances have been achieved in the chemical modification of drugs to enhance the solubility and pharmacokinetics, and arsenals of excipients are used to increase the solubility, control biodistribution, improve therapeutical efficacy, and reduce side effects.[53,54]

Drug delivery systems (DDS) are transporters and protectors, delivering the protected cargo to a specific organ, tissue, or cell, with or without a certain stimulus. DDS must be biocompatible, biodegradable, and stable in physiological media upon the chosen administration route.

1.2.1. Polylactide co-glycolide polymer

Synthetic polymers used for drug delivery may be linear, branched, or globular, and their size and copolymer composition can be tuned according to the application needs. Many polymers including polyacrylamides, polyamides, poly (amino acids), polyesters, poly (ortho esters), and polyurethanes, among others, are currently used to produce NMs for drug delivery. Polylactide co-glycolide acid (PLGA) is a copolymer produced with two aliphatic thermoplastic polyesters, the poly lactic and poly glycolic acids (PLA and PGA, respectively).[55] The extended use of this copolymer is a consequence of its biocompatibility and biodegradability. The copolymer has been employed since the 70´s in absorbable medical sutures Dexon® (PGA) and Vicryl® (PLGA 8:92).[56–58] The suture is made with a copolymer ratio lactide to glycolide of 9:1 and treated to modify the absorption time.

PLGA copolymers are synthetized via ring-opening polymerization of lactide (3,6-dimethyl-1,4-dioxane-2,5-dione) and glycolide (1,4-dioxane-2,5-dione) cyclic

dimers.[59] The lactide/glycolide molar ratio determines the internal hydro/lipophilic character, and is correlated with the hydration rate and crystallinity.[60] The lactide is more hydrophobic than the glycolide because the aliphatic chain is linked to the backbone. A higher composition in lactide results in longer degradation time, reduced wettability, and long-term hydrophobic compound release profiles. Pure lactide polymer with elevated molecular weight has been evaluated for bone implants or integrated as scaffold in tissue engineering.[61]

The polymer is degraded by the hydrolysis of ester bonds of the polymer backbone into their oligomers (fraction of the original polymer chain), and subsequently degraded into glycolic and lactic acid (Figure 1.3).[62] The lactide is metabolized into carbon dioxide and pyruvate, that enters in the Krebs cycle. Only the L-lactate is metabolized, while D-lactate is excreted. Glycolate is oxidized to glyoxylate and converted into glycine serine and pyruvate or directly excreted. It has been shown that carboxylic acid end groups autolyze the chain scission.[63]

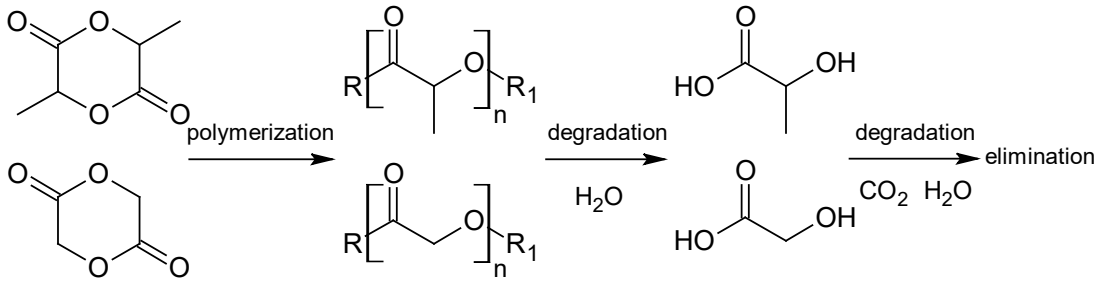

Figure 1.3. Cyclic dimers precursors of lactide (*upper*) and glycolide (*lower*) forming PLGA by polymerization and degradation by hindrance and metabolic elimination.

The rate of degradation is affected by different factors such as: the chemical composition of the polymer (monomer composition, monomer distribution copolymer composition, crystallinity, and molecular weight); [64,65] the structure of the particle (size, shape, surface area, porosity); and the environment, *i.e.* pH,

temperature, physical stress, medium, enzymatic environment, drug load, drug interaction, etc.[66,67]

The degradation of the copolymer via degradation of the backbone into oligomers and subsequently into monomers results in the release of the encapsulated drugs.[68,69]

1.2.2. Drug release in PLGA NPs

Usually, the release of drugs from PLGA matrixes undergoes a biphasic behaviour, described as two stages: an initial burst release and a second sustained release stage.[70] One of the multiple processes encompasses the degradation of the matrix. Simultaneously there are collective processes of surface diffusion, surface erosion, bulk diffusion, and bulk erosion. The release of the drug from the continuous degraded matrix becomes unpredictable and in general terms *in vitro* studies do not correlate to *in vivo* behaviour.[71]

The first phase of burst release is largely influenced by the polymer hydrophobicity, drug concentration, distribution, and solubility. If the compound is soluble in the aqueous medium, the drug present in the surface of the matrix will be released. During the second phase, the water will hydrolyse the matrix into oligomers and then into monomers. This degradation will be faster for lactide rich matrixes. The drug is released continuously though the worn-out layer. The combination of water erosion and drug release creates a continuous gradient of drug to the environment.[21] The *In vivo* scenario becomes more complex with the interaction of enzymes and proteins capable to remove and transport hydrophobic elements. [72–74]

The therapeutic window of PLGA NPs can be tuned to deliver drugs in a period from one week to few months.[75,76] A fast degradation, or short-term release requirement, can be achieved using more hydrophilic monomer (elevated lactide

composition), with low crystallinity, shorter molecular weight, and structurally made with large volume to surface area.[77,78] On the other hand, NPs with elevated proportion of glycolide monomer, high molecular weight, and crystallinity, combined with low soluble drugs can produce a long-term release. Under these circumstances, DDS are especially useful to deliver drugs over weeks to months, particularly when drugs with low solubility and poor metabolism, classified in the group IV according to the BDDCS (Biopharmaceutics Drug Disposition Classification System) are used.[79]

1.2.3. PLGA NPs synthesis

The production of PLGA NPs can be carried out by using different approaches according to the requirements of shape, size, composition, scalability and purpose.[62,80] Main approaches are: nanoprecipitation or phase separation, emulsification-solvent evaporation method, spray drying, microfluidic,[81] solvent casting, and dynamic production. In this thesis we have focused on the two first methods, more specifically on the single emulsion process used for delivering hydrophobic drugs.

A. Encapsulation by Polymer Nanoprecipitation

Nanoprecipitation is a method first reported in 1989 by Fessi et al.[82] It is based on the reduction of the solubility of the polymer by changing the solvent composition. The method consists of the deposition of a polymer solution, dissolved in a semi-polar organic solvent miscible with water, on an aqueous media. Precipitation occurs when the polymer solution is dissolved in an aqueous media in which the polymer is not soluble. In that way, during the dissolution of the organic solvent in the aqueous media, the polymer reaches the solubility concentration, becoming solid (see Figure 1.4). The process varies depending on the polymer's solubility, solvent nature, temperature, salinity, pH,

etc. In summary, the mechanism consists of four sequential steps, starting with the generation of a supersaturation, followed by nucleation, growth, and coagulation.

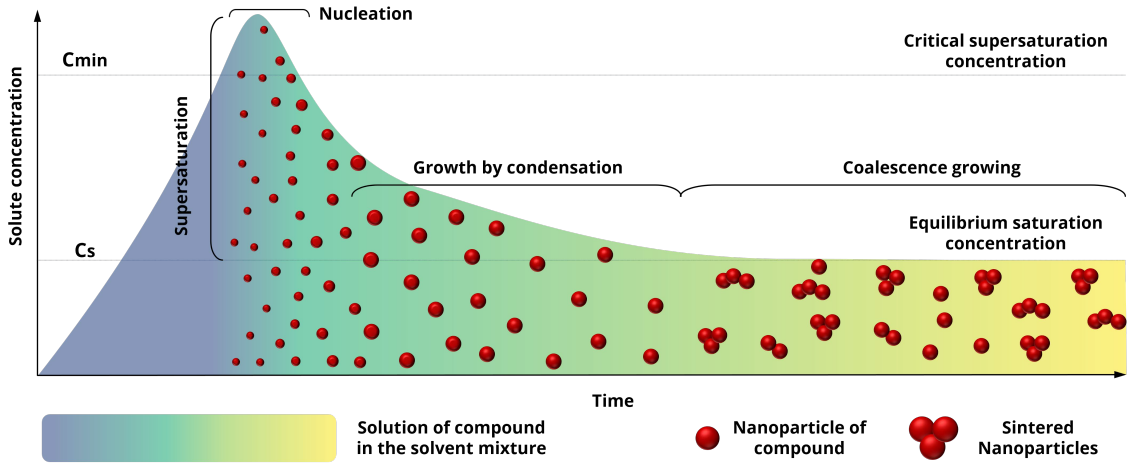

Figure 1.4. LaMer model of precipitation process by supersaturation of solvent poorly soluble in the major solvent or antisolvent.

The nucleation and growth of organic nanoparticles can be achieved by high supersaturation method. The supersaturation takes place when the polymer solution reaches the equilibrium state in which the solvent contains more dissolved polymer than the saturation value. This step occurs by the addition of the polymer solution to the aqueous media.

Supersaturation ratio is given by the ratio S_r between the solubility of the particle at the interface C_s, and the solubility of the bulk, C_∞, and is expressed as Equation 1. This equation reflects that a polymer with high solubility at the interface and low bulk solubility derives to smaller particles. However, the thermodynamically driving force of supersaturation changes locally and over time.

Equation 1 $$S_r \equiv \frac{C_s}{C_\infty}$$

The Equation 2 describes the solubility at the interface with respect to the local supersaturation at the interface of the particle, where γ corresponds to the

surface tension, M to the molecular mass of the solute, ρ to the density, T is the absolute temperature and R is the gas constant

Equation 2 $$\ln S_r \equiv ln\frac{C_s}{C_\infty} = 2\frac{2\gamma M}{\rho RTr}$$

As can be seen in LaMer diagram (Figure 1.4), once the supersaturation is reached, the system becomes thermodynamically unstable and evolves in nucleation step, overcoming the energy barrier for nuclei determined according to Equation 3, where σ correspond to the interfacial tension at the solid- liquid interface, v corresponds to the molar volume of the solute, K is the Boltzmann constant and T is the temperature.

Equation 3 $$\Delta G = \frac{16\pi\sigma^3 v^3}{3K^2T^2(ln\, S_r)^2}$$

Nucleation starts when the polymer (dissolved in the organic solvent) is introduced in the aqueous solution (anti-solvent) creating the supersaturation. Nucleation stops when the nuclei consume the amount of polymer dissolved and the polymer concentration reaches a value below the critical supersaturation concentration. The nucleation rate function (Nr) was described by D'addio and Prud'homme[83] in 2011 as Equation 4.

Equation 4 $$Nr = c \cdot \exp\left(\frac{-16\pi\sigma^3 v^2}{3K^3T^3(ln\, Sr)^2}\right)$$

Then the nuclei will grow by condensation or coagulation. Condensation takes place by the adsorption of monomers from the solution to the surface interface and integration to the nuclei matrix. In addition, formed nuclei can adhere between them when the attractive interactions overcome the repulsive interactions. Coagulation is the process in which one particle hits another particle and the surface molecules interact, gluing in an irreversible process. The collision frequency and efficacy lead the coagulation step, that depends on particle concentration, temperature, size, stirring rate, stabilizer, ionic strength, etc. and depends on the balance of attractive and repulsive forces between the particles.

To prevent the coagulation, stabilizing agents are added to the formulation. These are adsorbed at the surface of the particles, thus increasing the repulsive interaction between nanoparticles.

After particle formation, the solvents used during the process and the excess of free compounds must be removed by filtration, centrifugation, freeze-drying, etc. However, in this process the properties of the particles may be altered. Attractive interactions (Van der Waals forces) between particles can prevail when the particles are very close to each other, eventually resulting in irreversible attachment thus forming aggregates and sintered particles. The limitation of coalescence growing is hindered using a surfactant at desired concentration to achieve the designed size. Otherwise, some properties derived from the nanometric scale might be lost.

Despite the aforementioned issues, the nanoprecipitation method has certain advantages like simplicity, scalability, narrowed size distribution, size versatility and reduced toxicity.

B. Emulsification Solvent Evaporation of Polymers

In this method, oil in water emulsion is produced with ultrasonic homogenizer. Emulsification Solvent Evaporation (ESE) method is a two-step approach that involves first the formation of small droplets of an oil phase (non-aqueous organic solvent holding the polymer and the cargo compound) into an aqueous phase (with the stabilizing agent); in a second step, the organic solvent is evaporated. The process consists in the comminution (destruction) and condensation (construction) of the oil phases, where thermodynamics play a key role.

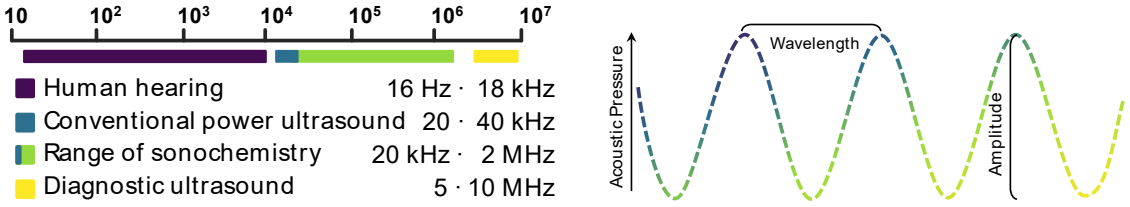

Figure 1.5. Range of frequencies based on their frame of actuation (*left*) and descriptive scheme of the parameters of a wave (*right*).

The sonication or sonochemical process is a way to transfer the energy to the system. It consists in the transmission of sonic waves or ultrasounds (Figure 1.5) in the frequency range of 20 kHz to the 2 MHz from a power source to a liquid. Sonochemistry is the use of ultrasound to produced or enhance a chemical reaction and is widely used in different applications including catalytical reactions, formation of radical species, electrochemistry, extraction, crystallization, formulation, liquid processing (emulsification, homogenization, degasifying, extraction), and cleaning.[84]

There are several parameters that have a substantial impact on the sonochemical process: intensity, frequency, temperature, solvent properties, and dissolved gas.

Intensity and ultrasonic frequency are the two main elements of a wave. Frequency is defined according to Equation 5

Equation 5 $$f = c/\lambda$$

where c is the celerity of the sound in a media (1450 min s^{-1} in distilled water) and λ is the wavelength (m) of the wave. For example, the wavelength value at 20 000 cycles per second in water is 72.5 mm.

In the range of conventional ultrasound, acoustic cavitation is produced in water when the threshold value of 0.5 W cm^2 at 20 kHz is achieved. This threshold is increased in organic solvents.

The sound intensity is defined as the power transmitted per surface unit, according to the Equation 6.

Equation 6 $$I = P_A^2/2\rho c$$

were P_A being the acoustic pressure and ρ is the density of the medium. Noteworthy, the equation is only valid for waves with low-pressure variation and in case of the ultrasonication range used for the preparation of nanomaterials, the pressure variations may reach bars of different, that lead to the Lepoint-Mullié nonlinear equation[85]. Intensity refers to the acoustic power delivered to the medium.

Cavitation efficiency in sonochemistry processes rely on a good balance of the properties of the solvent (density, volatility, and viscosity), which change with the temperature. Each solvent has its own optimized cavity efficiency range at a certain temperature range (dichloromethane, ethanol and water have their maximum at -40, 21 and 35 °C, respectively)[86].

At low ultrasonic frequency the temperature increases rapidly due the macroscopic processes induced such as gas steaming, turbulent regimen regeneration, and different mechanical effects (microjet bubbles that increase cavitation threshold). However, at high frequencies, the mechanical effects are minimized, and the temperature increase is easily controlled.

The other critical parameter is the solvent properties, more specifically the intermolecular forces than ensure the cohesion of a liquid, which determine the cavitation threshold. Weaker forces derive in lower threshold, and therefore, less energetic sonochemistry energies are delivered. On the other hand, dense and viscous liquids display a cavitation threshold higher than a less dense liquid, but they need higher acoustic pressure to tear apart molecules of the liquid.

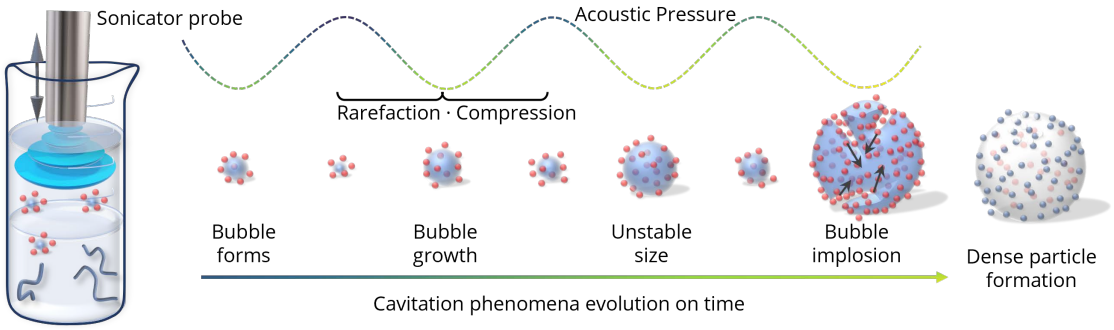

Figure 1.6. Scheme of sonication process in liquid performed by a sonication probe and the evolution according to the rarefaction and compression of the waves to form final dense polymer nanoparticles.

As can be seen in the

Figure 1.6, the vibration is created by the piezoelectric device that is connected to the metallic horn tip or probe, that is in contact with the liquid and generates an oscillating up and down movement, thanks to the power source connected to the piezoelectric device. The oscillatory movement of the tip produces a variation of the pressure denominated acoustic wave that is transmitted through the liquid.

The energy is transferred to the medium as an ultra-sound wave producing the cavitation phenomena, due the rapid change of pressure in a liquid, that leads to the formation of small vapor-filled cavities, in the spots where the pressure is reduced under a certain value.

The total distance of one movement up and down the oscillating movement is called amplitude. The standard sonication probe has an amplitude of around 100 μm, and this is one of the parameters selected in the operation to deliver low or high intensity sonication. The wave amplitude, or elongation shift distance, is determined by the physical properties of the piezoelectric transducer horn geometry and enhancer adaptor. Nevertheless, the frequency (number of pulsations per second) is determined by the combination of the power supply

with the piezoelectric device that operates usually at a fixed frequency and is machine dependant.

From the practical point of view, for a standard sonication tip working at 20 kHz, the generated amplitude of a tip ranges from 70 to 160 μm when the amplitude is set up at 100 %, depending on the tip geometry. Amplitude and intensity are directly correlated. To be able to reproduce results, the amplitude setting, temperature, viscosity, stirring rate and volume of the sample are all parameters that need to remain consistent. It is desirable to perform the process in a fast and efficient way to avoid mass transfer from the probe to the aqueous solution.

During the sonication process, the organic solvent is partially evaporated, and the remaining organic solvent can be eliminated after one hour of stirring while polymer NPs are condensed. By using this method, the NMs are prepared in minutes, and the more condensed size can be achieved after ninety minutes under stirring conditions at room temperature. After a few purification steps, the NPs are ready to be used.

This method is used to encapsulate preferentially hydrophobic and lipophilic compounds and it can be easily scaled, although synthesis reproducibility is lower than the nanoprecipitation method.

1.3. Drug delivery systems: Mesoporous adsorption

Another way to prepare DDS is using NPs with a porous structure in which drugs can be absorbed. Among others, silica mesoporous materials provide large surface areas with versatile structure, tuneable size, chemical stiffness, and designable release profile (hydrophilic-lipophilic balance, pore size, stimuli-responsible gates, etc.). The porous structure provides a protective shell to avoid

compound degradation and allow selective release upon degradation of the silica matrix.

Silica mesoporous materials were developed by Mobil Corporation in 1992.[87] The synthetic routes of a family of structures are based on the hydrothermal reaction of silica precursor in the presence of amphiphilic structure directing-agents (SDA). The SDA forms organic structures and over that surface the inorganic structure is formed, by the hydrolysis and polycondensation of the silica precursors (tetraethyl ortho silicate TEOS or tetramethyl ortho silicate TMOS are the most common precursors used).[88–91] Once, the hybrid material is formed, the porosity emerges by the elimination of the organic template by calcination or extraction. These materials present an elevated surface area (up to 1500 m^2 g^{-1}) and a high pore volume (*ca.* 1.3 cm^3 g^{-1}) with homogeneous and tuneable pore size distribution (from 2 to 30 nm) and elevated chemical resilience to certain chemical conditions. These materials are easily modified through the dense arrange of silanol groups. These properties allow these materials to be used to improve catalytic reactions,[92–94] to adsorb and separate heavy elements,[95–97] and in the context of nanomedicine can be used as controlled drug release systems,[98–100] bone regeneration scaffolds,[101–103] genetic transfection vector[104,105] or cell markers.[106]

1.3.1. Synthesis of silica mesoporous NPs

The method to synthesize uniform dense silica nanoparticles was described by Stöber, Fink and Bohn in 1968.[107] It consists on the hydrolysis of tetra(alkyl) silicates in an alcoholic mixture, using ammonia as catalytic agent. The reactions follow a two-step sequence, starting with the precipitation of the silica nuclei (nucleation step) and followed by the gradual incorporation of hydrolyzed groups (SiO_4^{4-}) onto the nuclei surface (growing step). The size and the

morphology of the NPs are driven by the amount of precursor, the concentration of the catalytic agent and the composition of the alcoholic mixture.

The modifications of the described method to generate mesoporous structures are based on the incorporation of SDA to from a liquid-crystal phase. As Figure 1.7 shows, the SDA will self-assembled forming ordered structures that are stabilized by the polycondensation of silica precursor onto the polar region of the SDA on a cooperative growth regime. The kinetic reaction of the sol-gel process is driven by the condensation rate of the silica, type and concentration of SDA, temperature, pH, and temporal concentration of precursor. With this method it is possible to obtain different nanoparticulated sizes and shapes (spheres, bars, worms, beam-likes) with different porous structures and pore sizes.

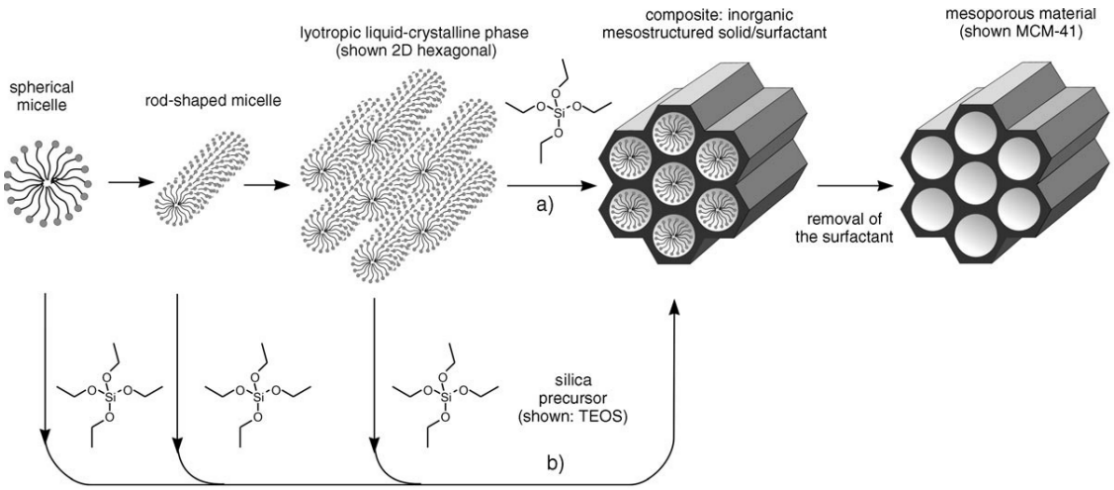

Figure 1.7. Formation of mesoporous material by SDA agents by liquid-crystal template (*a*) and cooperative liquid-crystal template mechanism followed by silica condensation by the precursor addition (*b*).

According to Hou et al.[108,109] there are different synthetic routes to produce mesoporous structures depending on the organic/inorganic interface, represented by the charge of the inorganic surface (*I*), determined by the pH of the medium, the charge of the head of the surfactant (*S*) and the charge of the mediator (*X*), if needed. At pH values below 2, the isoelectric potential (IEP) of

silica, the majority of the silanol groups at the surface are protonated generating a net positive charge on the surface I^+. At neutral pH, the surface has a net neutral charge I^0, and above the IEP the overall charge surface presents a net negative charge I^-, and therefore the majority of the silanol groups are deprotonated. The head of the surfactant can be positive S^+, negative S^- or neutral S^0, while the mediator can be a cation X^+ or an anion X^-. Therefore, to perform a synthesis at basic pH, the route S^+I^- with an alkyl ammonium surfactant type, hexadecyltrimethylammonium bromide (CTAB) was used in the context of the thesis.[108,109]

With the objective of fine tuning the pore size, different lengths of the alkyl chain surfactant can be used to obtain pores from 1.8 to 2.5 nm in diameter. To obtain larger pores sizes, swelling agents such as 1,3,5-trimethylbencene (TMB), N,N-dimethylhexylamine or non-ionic triblock co-polymers like Pluronic® P65, P123 or F127 can be used. The pore size obtained is in the range of 5 to 30 nm, and allow to host macromolecules and short chains of DNA or RNA in the pores.[22]

1.3.2. Functionalization of silica mesoporous NPs

After the synthesis of the mesoporous NPs, the SDA must be removed to release the porous structure and allow the surface to be functionalized. There are two methods used for the extraction of organic phase without altering the porous structure: the calcination at high temperatures and the ionic exchange. The main drawback of calcination is the irreversible loss of water due to the condensation of the silanol groups (Si-O-Si), resulting in a decrease in the number of available silanol groups to react in the post-grafting steps or producing irreversible aggregation of NPs. Therefore, in this thesis we used the ionic exchange with an ethanol (85 %) acid solution for surfactant removal. The proton intercalates into

the interface removing the CTAB from the inside of the pores,[87] allowing the following functionalization.

The incorporation of functional moieties into the mesoporous wall structure is performed by addition to the precursor moieties bearing two triethoxysilane chains, as $(R'O)_3Si\text{-}R\text{-}Si(OR')_3$, will be incorporated into the matrix of the walls without altering the structural or silanol density. When the molecule incorporated during the synthesis presents only one silane chain precursor, as $(R'O)_3Si\text{-}R$, the organic tail is disposed at the surface, providing an anchoring point for further functionalization. In this thesis, this strategy was used to provide fluorescence properties to perform *in vitro* studies. Another post synthetic functionalization or grafting can be performed by condensation of $(R'O)_3Si\text{-}R$ species after or before SDA extraction to functionalize the desired region of the NPs. In this case the functionalization can produce a partial or total reduction or the porosity. The grafting of designed molecules on the mesoporous allows to enhance the colloidal stability, increase the circulation time, reduce cytotoxic effects, or enhance the delivery of the NPs to certain tissues or organs.

1.3.3. Drug encapsulation on mesoporous NPs

The encapsulation of drugs inside mesoporous NPs is performed by the adsorption of the drugs on the surface of the walls of the pores. The elevated surface area of mesoporous nanoparticles corresponds mainly to the internal surface of the pores.[110] Depending on the physical-chemical properties of a compound to encapsulate, a previous adequation of the surface is required to modulate the interaction matrix-drug, which will regulate the drug release profile.[111–113] The adequation to modulate the matrix-dug interaction with the drug is performed by the functionalization of the surface with chemical groups[114,115] that are able to associate with the drug on different manner. As can

be seen in Figure 1.8, for non-covalently linked drug, the interaction of ibuprofen with the matrix it can performed on silica by physisorption, hydrogen bond; or stronger interaction it can be achieve with aminated matrix through the ionic interaction between the amino and the carboxy group of the drug.[116]

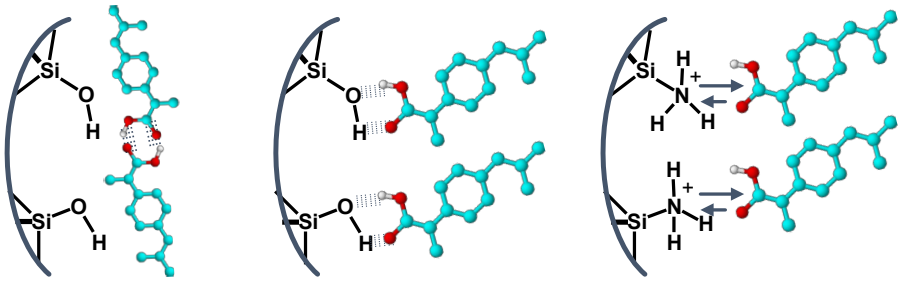

Figure 1.8. Scheme of interacion of ibuprofene molecule with a silica matrix. Weak interaction of physisorpted dimer molecule (*left*), hidrogen bond interaction betwen silanol groups and the carboxilic acid groups (*middle*), and stronger ion interaction between ammonium groups of aminated surface and carboxilate groups of the drug (*right*).

The balance between the drug-solvent *vs* the drug-matrix can be optimized through the surface functionalization and the organic solvent used to load de drug into the NPs.[117,118]

For non-covalently linked drugs, the drug will start to be released immediately after administration of the NPs, when the interaction with the media starts. It has been widely reported that such systems present a double stage release: first a burst-release is observed followed by a second stage of sustained release. Several *stimuli-responsive* systems have been developed to overcome the undesired unspecific release from mesoporous nanoparticles by the use of covalent attachment of drug to the matrix and molecular gates attached at the surface of the pores.[119]

1.4. The fate of Nanoparticles *in vivo*

Intravenous administration of substances derives in the immediate interaction with blood components: 45 % (v/v) corresponding to erythrocytes, leukocytes, and thrombocyte; and 55 % (v/v) corresponding to blood plasma, containing 92 % water and 8 % of proteins (albumin, globulins, fibrinogen, regulatory proteins, clotting factors, immunoglobulins, lipoproteins, etc.) and electrolytes (Na^+, K^+, Mg^{2+}, Ca^{2+}, Cl^-, HCO_3^-, HPO_4^- and SO_4^{2-}). When NPs are injected in the blood torrent, the electrolytes and proteins (with an average concentration of 75 mg mL^{-1}) interact with the NPs surface.[120–122]

Albumin, the most abundant protein in blood, will be absorbed on the surface of the particle, among other minority proteins forming a shell around the particle surface (protein corona, PC). This corona will evolve during time. Opsonin are bivalent functional immunoglobulins which recognize foreign materials and present receptors recognized by macrophages. The PC evolves in time depending on the characteristics of the NM, including size, shape, surface charge, stiffness, and lipophilic balance, among others.[123,124]

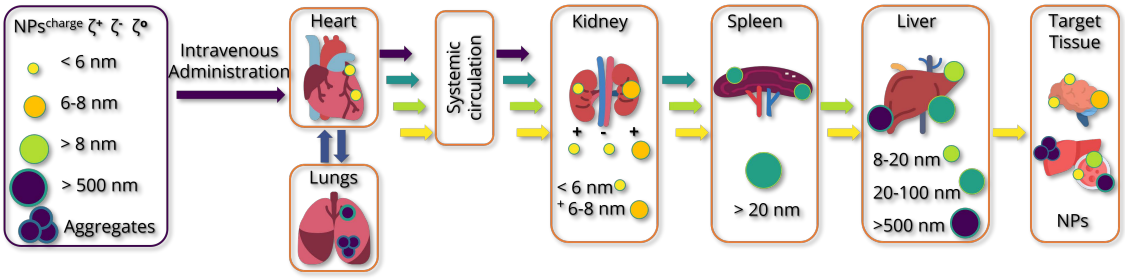

Figure 1.9. Drainage scheme of NPs according to their size and surface charge by the mononuclear phagocyte system.

After intravenous injection, nanoparticles travel to the heart, and during circulation particles can aggregate due the actions of surrounding proteins and ions. In their way from the heart, the particles will pass through the lung's capillaries, which have a standard size of 6 μm. The lung immune macrophage

activity is continuously recruiting monocytes and are the most prevalent immune cells in the lung environment. Due to the high monocyte recruiting activity, the aggregates and big particles are easily detected in the capillaries and remain physically stuck or monocyte phagocyted (Figure 1.9).[125]

Once the particles pass through the lung, they are systemically distributed, and the particles from the blood torrent, are mainly drained by the macrophages according to size. The particles detected by monocytes present in the liver, the *Kupffer* cells, are transferred to the endosomal digested content to the space of *Disse*, ending in the hepatic ducts; and depending on the digestive state and bile production, the nanoparticles travel to the gallbladder, eliminating the particle through the gastrointestinal tract. Finally, the NPs reach the duodenum, part of the small intestine, via the sphincter of Oddi.[126] When a nanoparticle has sizes below 8 nm, clearance happens when the particle enters in the glomerular capillary, via the afferent arteriole which is a negatively charged fenestrated membrane with holes of 5 nm size. Particles below 6 nm are freely filtered, although only positive particles with sizes between 6 and 8 nm are filtered. The filtered particles throughout the glomerular basement membrane (GBM), arrive at the proximal tubule, where the positively charged NPs are more likely to be resorbed, due to the negative charge of epithelial cells. Between the wall of cuboidal cells, the positive particles can pass to reach the interstitial space.[18,126,127]

The elimination process of nanoparticles is fundamental to avoid their long term accumulation.[128] Renal clearance is faster than hepatic clearance, so it is a desirable way to excrete NMs with potential toxic accumulative effects. The design of NPs can be tuned to avoid PC formation or can be designed to tune the PC in a specific manner.[129]

1.5. The Role of Nuclear Imaging in Nanomedicine

Nuclear imaging techniques are unique tools to quantify and determine the location of chemical or biological species over time after administration to a living organism. The application of nuclear imaging techniques requires the administration of a chemical or biological entity previously labelled with a radionuclide, which are unstable atoms of an element that release radiation over a certain time. Each radionuclide decays in a unique way, emitting a combination of charged particles (alpha or beta), neutral particles (neutrino or antineutrino) and different penetrating electromagnetic radiations.

Certain radionuclides emit high energy gamma rays, and hence they have special interest in the medical field. Indeed, high energy gamma rays can penetrate through biological tissues and be detected by an array of detectors placed outside the organism under investigation, thus enabling non-invasive and quantitative tracking. In the biomedical field and for imaging purposes, two kinds of radionuclides are used: gamma and positron emitters.

Nuclear imaging techniques allow the execution of studies to determine the biodistribution of a wide range of molecular modalities (including NPs) with high sensitivity and non-invasively. By introducing the radionuclide in different positions of the molecule/biomolecule under investigation, they also enable the determination of the biological fate of NMs and their components.

One of the critical stages to apply nuclear imaging is the radiolabelling or incorporation of the radionuclide to the species to be investigated. Radionuclides can be incorporated through different approaches to NPs. These include but are not limited to: (i) direct activation with neutron or ion irradiation; (ii) nonspecific adsorption; (iii) coprecipitation; (iv) formation of a complex with a radiometal; and (v) functionalization with a labelled-prosthetic group.[130]

Depending on the emission properties of the radionuclide, two different nuclear imaging modalities can be used: gamma emitters are used in Single Photon Emission Compute Tomography (SPECT), while positron emitters are used in Positron Emission Tomography (PET). Both techniques are minimally invasive and are translational from the preclinical to the clinical fields.[131] The decay mechanisms are explained in the following Sections 1.6.1 and 1.6.2.

1.6. Radiolabelling NMs, pivotal role for biological fate studies

One major obstacle for the establishment of NMs in biomedicine is the difficulty associated to their tracking and the assessment of their biological fate after their administration to a living organism. The study of the stability biodistribution, metabolization and excretion can be partially achieved by the incorporation of radionuclides followed by nuclear imaging.

The half-life of the radionuclide needs to be considered to evaluate the time windows in which the NPs should be tracked. NPs radiolabelled with a short half-lived radionuclide will be investigated only during first stages of biodistribution. In contrast, if the half-live is too long, high radiation doses will be delivered to the investigated subject, with potential side effects. Another important aspect to consider when radiolabelling NPs is the radiochemical stability. If the radionuclide does not stay together, *i.e.* if the radionuclide detaches or the nanoparticle degrades, imaging data will not be representative of the biodistribution or fate of the NP.

Depending on the biodistribution study to be carried out, the isotope can be incorporated into the different components of which the particle is made (see Figure 1.10). From the point of view of the location in the structure of the NPs, the radionuclide can be incorporated into or with the structural components through co-precipitation, adsorption, isotopic exchange, or nuclear activation.

Figure 1.10. Labelling strategies used to incorporate radionuclides into de different component of the NPs.

The incorporation of the radionuclide to the surface of the NPs can be achieved by, among others, chemical redox reactions, isotopic exchange, using bifunctional chelates, by nonspecific adsorption or with the use of prosthetic groups carrying the radionuclide and are attached to the NP surface. The cargo of the NPs can be radiolabelled and subsequently incorporated into the NPs before or after the synthesis of the NPs. As discussed before, while the radiolabelled cargo remains encapsulated in the nanoparticles, information on the biodistribution of the nanoparticle will be obtained. However, if the cargo is released, the information obtained from imaging studies will be difficult to interpret, as it will correspond to the location of the intact NP (with the cargo) and the cargo itself.

1.6.1. Gamma emitters

Gamma emitters decay in a range of energies below the MeV energies, and each isotope decays with a unique and specific spectrum energy. Photons are emitted in all directions and are detectable by most of commercially available cameras in the range 100-300 keV. Table 1.2 shows the main properties of gamma emitters most commonly used in the clinical setting.[132,133]

Table 1.2. Single photon emitters frequently used for clinical diagnostic and therapy with their half live and the energy of the emitted photons

Radionuclide	Half-life	γ Energies [keV] (Fraction %)
^{67}Ga	78.3 h	93 (39), 185 (21), 300 (17), 393 (5)
^{99m}Tc	6.0 h	140 (89)
^{111}In	67.9 h	172 (91), 245 (94)
^{123}I	13.2 h	159 (83)
^{131}I	192.2 h	364 (82), 637 (7)

Gamma emitters are detected with SPET cameras (Figure 1.11). These cameras consist of a rotatory collimator placed between the radiation source and the scintillator detectors, coupled with photo multipliers. The rotary system allows the system to obtain angular views, known as projections. Photons are filtered with the collimator, which consists of a mesh-oriented cell made with a high-density metal and filters those photons that do not reach the detector perpendicularly, thus allowing the determination of the position of the disintegration.

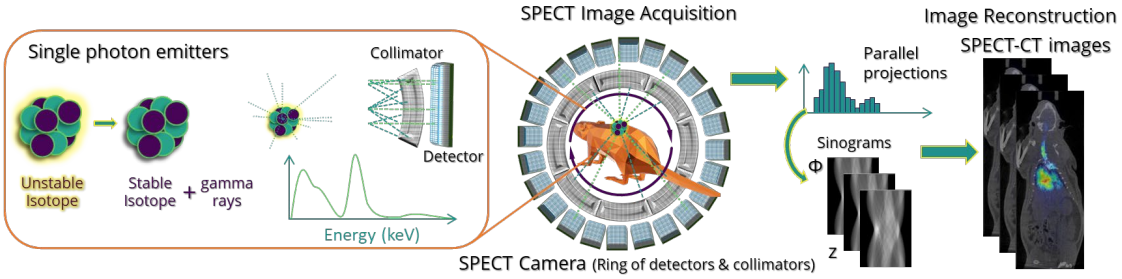

Figure 1.11. Scheme of the photon emitters with determined energy profile (*left*); scheme of a SPECT camera with the collimator system, filtering photons that do not reach the detectors perpendicularly (*middle*); Representative images obtained in SPECT imaging studies (*right*).

The presence of the collimator aids in the identification of the position of the disintegration. However, a high percentage of the incident photons are not indeed detected, thus compromising the sensitivity of the technique, especially when compared to PET cameras (see below). Still, SPECT cameras have the

potential to discriminate energies, opening thus opportunities to perform *in vivo* studies with different radionuclides with different emission properties simultaneously.

1.6.2. Positron emitters

Positron emitters are atoms with a low ratio neutron(n):protons(p), which lies below the stability band. When this happens, a proton is spontaneously converted into a neutron, and a positron (particle with the mass of an electron with positive charge) is emitted with a certain energy. Most of positron emitters are produced via proton irradiations, and their half-life tends to be lower than photon emitters.

Positron emitters decay by emission of a positron from the parent nucleus. The emitted positron travels a distance (positron range; typically, a few millimetres in water) while interacts with the surrounding matter. When it is almost at rest, the positron undergoes an annihilation process with an electron of a surrounding atom, resulting in the formation of two gamma rays with 511 keV each that are emitted in opposite direction. The Table 1.3 summarises the main properties of positron emitters commonly used in the clinics and in research.[133,134]

Table 1.3. Frequently used positron emitters in nuclear imaging research and medical applications.

Radionuclide	Half-life	Production route	β^+ $Energy_{max}$ [MeV] (Fraction %)
$^{11}C^*$	20.4 min	$^{14}N(p,\alpha)^{11}C$	0.981 (100)
$^{13}N^*$	10.0 min	$^{16}O(p,\alpha)^{13}N$	1.190 (100)
$^{15}O^*$	2.1 min	$^{15}N(p,n)^{15}O$	1.732 (100)
^{18}F	109.8 min	$^{18}O(p,n)^{18}F$	0.634 (97)
^{89}Zr	78.1 h	$^{89}Y(p,n)^{89}Zr$	0.910 (100)
^{64}Cu	12.7 h	$^{64}Ni(p,n)^{64}Cu$	0.579 (39), 0.653 (18)
^{68}Ga	67.7 min	$^{69}Ga(p,2n)^{68}Ga$	1.890 (89)

* Despite the short half-live of the radionuclides, those can be used in infrastructures with a cyclotron.

The simultaneous emission of two gamma rays after the annihilation allows the determination of the location of the radionuclide with high sensitivity and quantitatively. PET cameras consist of arrays of detectors concentrically placed along the axis of the field of view (Figure 1.12). When two photons are detected by two different detectors with a time difference below a few picoseconds, this is considered a coincidence event. The line between the two detectors is known as the line of response, and the annihilation occurred somewhere along that line. This is called "electronic" collimation, contrarily to SPECT where collimation is "physical". The detection of hundreds of thousands of coincidences allows the generation of a three-dimensional image providing information about the spatial distribution of the labelled entity. The image is obtained through a reconstruction process. Over the years, different reconstitution algorithms have been developed. These can be classified into analytical methods, Filtered Back Projection (FBP) and few variants of the iterative statistical reconstruction methods like the Ordered Subset Expectation Maximization (OSEM).

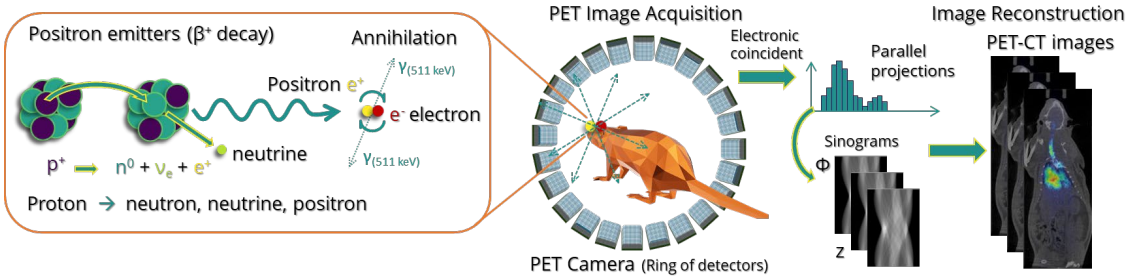

Figure 1.12. Scheme of the mechanism of betta positive decay (*left*); schemes of the detection of the annihilation of two gamma rays detected on a PET-camera with the associated signal obtained (sinogram) (*middle*); representative images obtained after reconstruction (*right*).

Nuclear imaging techniques do not provide anatomical information of the subject investigated. Because of this, these imaging modalities are combined with X-ray computerised tomography (CT). The co-registration of the two images (PET and CT) allows for the determination of the spatiotemporal distribution of the labelled entity, and its anatomical localization within the organism. Furthermore, the gamma rays emitted suffer an attenuation within the organ (specially in large animals) that may have an effect in the registration of the signal on the detectors. The CT images allow the generation of the attenuation map, which is used during PET or SPECT image reconstruction.

2. Aims of the thesis

2.1. Justification of the study: Nano Fate Project

The PhD dissertation aims to bring insights of the biological fate of NMs with potential interest in the field of nanomedicine. The high number of nano-formulations, especially at distinct stages in clinical trials, has raised concerns in the society for the toxicological effect of nanomedicines.

The Spanish Government with the support of the European Union Commission funding agency, granted the project called NanoFATE: Translocation, Biological Fate and Biointeractions of Engineered Nanoparticles with Biomedical Applications and for Nanosafety Evaluation. The part of the project conducted at CIC biomaGUNE aimed at designing NPs as drug carriers for intravenous administration and the evaluation of their interaction with the plasma and biological fate, this is, how the carrier behaves, where it accumulates and if it degrades during circulation.

This thesis, which is framed in the above-mentioned project, focuses on the evaluation of the biodistribution and biological fate, using nuclear imaging, of two examples of nanoparticle carriers for drug delivery: polymeric biocompatible nanoparticles of poly lactic co glycolic, suitable for the

encapsulation of hydrophobic drugs; and inorganic mesoporous silica nanoparticles, characterized for a regular array of pores, which can be used for holding a wide variety of molecules (hydrophilic and hydrophobic).

Chapter 3 covers the synthesis, characterization and biodistribution studies of PLGA polymeric NPs coated with either albumin or polyethyleneimine and loaded with a hydrophobic compound. The synthesis by nanoprecipitation was performed encapsulating the hydrophobic compound 1,2-dicarba-closo-dodecaborane (*o*-carborane) 1 to 20 wt % respect to the total content. Further studies were performed to assess the biodistribution of the compound incorporated into the PLGA NPs.

Chapter 4 describes the formation of the protein corona onto NPs made of PLGA and with hydrodynamic size of 150 nm, coated with albumin and polyethyleneimine. The aim was to evaluate the formation of the protein corona and determine its stability.

Chapter 5 describes the biological fate of mesoporous silica nanoparticles stabilized on the surface with polyethylene glycol and decorated with a peptide on the surface. With that aim, double labelling of the core and the peptide was carried out with different radionuclides, and nuclear imaging studies with the different labelled entities were carried out.

2.2. Objectives

This thesis aims to advance on our knowledge on the fate of nanoparticle formulations for drug delivery in vivo by nuclear imaging techniques.

The specific objectives of this thesis are:

A. To optimise the preparation of PLGA NPs with variable concentrations of a hydrophobic drug.

B. To assess the biodistribution pattern of the hydrophobic drug encapsulated in PLGA NPs, after parenteral and pulmonary administration, using small rodents and PET imaging.
C. To assess the formation and stability of the protein corona on PLGA NPs from serum using radiolabelled proteins and nuclear imaging techniques.
D. To determine the biodistribution pattern of Mesoporous Silica Nanoparticles modified with a homing peptide for tumour targeting on an experimental animal cancer model, using Positron Emission Tomography.
E. To assess the stability of core and coatings in mesoporous silica nanoparticles in vivo by combining core and surface radiolabelling strategies and analyse the advantages and drawbacks of labelling either the core or the coating of the nanoparticles.

3. Synthesis, characterization and biodistribution of PLGA NPs

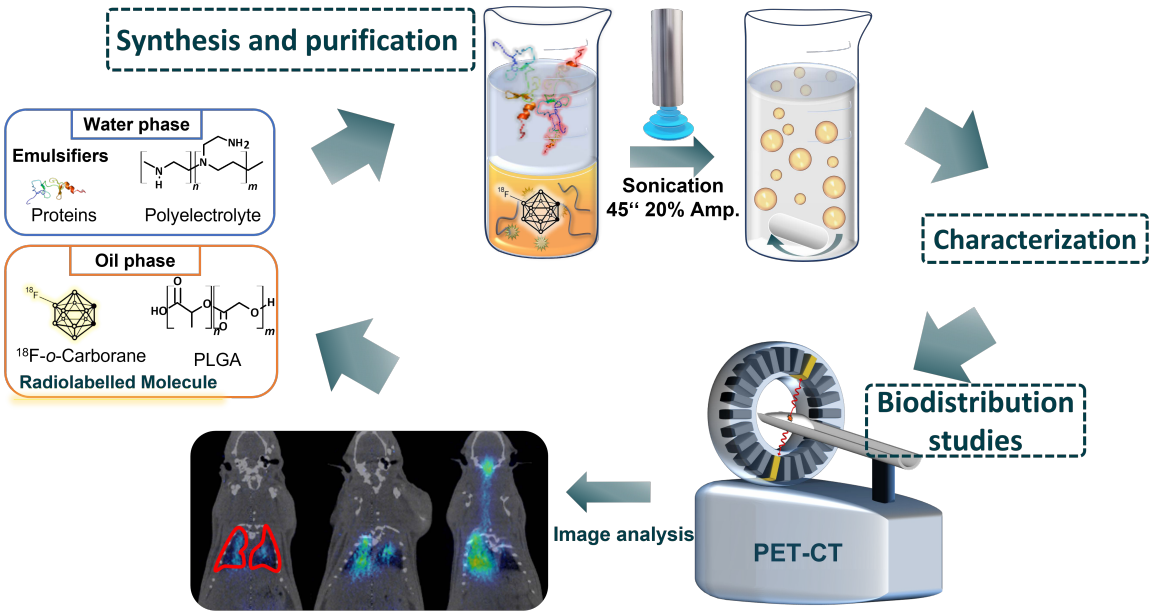

3.1. Introduction

A plethora of drug delivery systems (DDS) have been approved in the last two decades either by the European Medicines Agency (EMA; Table 1.1) or the Food and Drug Administration (FDA). DDS can aid in the site-selective delivery of drugs with unfavourable pharmacokinetic properties or undesired toxicological or side effects, thus increasing the efficacy while minimising off-target side

effects.[135] DDS play a pivotal role, for example, in the administration of compounds with low solubility in water and poor metabolism, which are classified in the group IV according to the Biopharmaceutics Drug Disposition Classification System (BDDCS).[79] DDS are also useful to achieve a controlled release of the drug over weeks or months.[136,137]

Among DDS, biocompatible polymers are particularly interesting due to their low toxicity and biocompatibility. Polymers such as poly(lactic-co-glycolic acid) (PLGA) have been widely exploited to deliver hydrophobic compounds due their hydrophobic and biocompatible character.[138] Additionally, the degradation time of PLGA and release kinetics of the encapsulated drugs can be modified by tuning the monomeric composition of the polymer and the method used for its preparation, turning these polymers into very attractive DDS.[139,140]

The properties of DDS must be designed not only considering the drug itself, but also the administration route, as the latter defines the biological barriers to be overcome to reach the target organ or tissue. For example, DSS designed for dermal administration must overcome different dermal barriers and penetrate a few millimetres through the skin to reach the epidermis, the dermis or the blood torrent.[141] On the other hand, advanced therapy medicinal products (ATMPs) designed to modify genetic malfunction of certain cells in a specific tissue or organ are usually administered parentally.[142] Still, the majority of DDS are intended for intravenous administration. This administration route introduces the DDS (and the drug) directly into the bloodstream, thus favouring the distribution over the whole body. However, the blood is a complex fluid which contains a wide variety of cells and (bio)molecules, which could interact with the administered DDS. Such interactions, which will be influenced by the size, the shape and the surface composition of the DDS,[143] will have an impact on biodistribution and biological fate of the DDS. Consequently, the design of the

surface composition of nanomaterial-based DDS plays a key role in their biological fate, and hence it is a critical aspect for the success of the treatment.[144]

The investigation of the interactions between nanomaterials and the different components of the blood is not simple. One of the strategies commonly used to gain knowledge on the *in vivo* behaviour of nanomaterials relies on the use of plasma proteins to perform experiments *in vitro* under controlled conditions.

Among all proteins present in blood, albumin is the most abundant. It is synthesized in the liver, regulates the osmotic pressure, and transports molecules such as enzymes, vitamins, and hormones, among others. The high abundance of albumin in the blood has encouraged researchers to use this protein in the preparation of DDS, either as the main component or as a stabiliser, to prevent rapid opsonization after administration.

Another commonly used strategy to functionalize and stabilize PLGA particles is based on the use of aminated polyelectrolytes. Polyethyleneimine (PEI) is a well-known biocompatible, aminated, cationic polyelectrolyte widely used in biotechnological applications, including gene therapy. It is used as stabilizer of polymeric NPs, providing the surface with positively charged amine groups. The presence of positive charges on the surface enables gene complexation and delivery,[145] and increases the interaction with cell membrane. Moreover, once inside the cell endosomes, the polymer can act as proton sponge, thus neutralising the acidic environment of early endosomes and disrupting endosome maturation and favouring particle translocation.

In the context of this PhD thesis, we have studied the biological fate of polymeric (PLGA-based) NPs bearing either PEI or albumin on the surface as DDS for small, water insoluble hydrophobic compounds (class IV), by applying molecular imaging techniques. As a model drug compound, the hydrophobic

compound 1,2-dicarba-*closo*-dodecaborane (also known as *ortho*-carborane or *o*-carborane) was selected, as it has shown promising properties as hydrophobic pharmacophore in receptor-ligand interactions including opioid, androgen retinoic or HIV protease receptors.[146,147] The ultimate goal of this part of the work was to evaluate the biodistribution and biological fate of the administered DDS and investigate the parameters affecting *in vitro* stability and drug distribution within the particle.

3.2. Results and discussion

Our first step was to optimise the production of PLGA NPs stabilized either with albumin or PEI (Figure 3.1). Polymeric NPs were synthesised following two of the most used processes: (i) nanoprecipitation; and (ii) emulsification/evaporation.

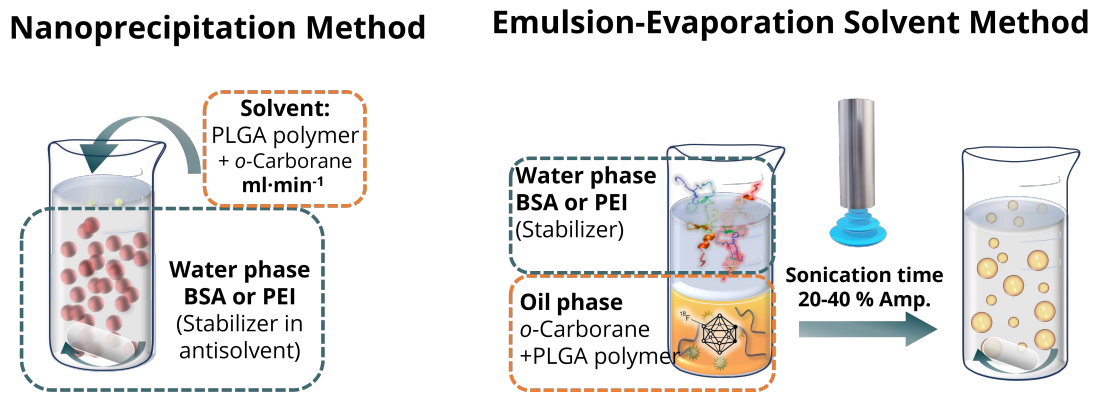

Figure 3.1. Scheme of the two synthetic methods used to produce PLGA coated nanoparticles with albumin and polyethyleneimine.

Both methods have advantages and drawbacks. Nanoprecipitation requires the dropwise addition of an organic solvent (total or partially soluble in the anti-solvent) on the antisolvent which already contains the stabilizer, followed by purification; on the other hand, the emulsification/evaporation method involves a sonication step to disrupt the two phases into sub-micron emulsions surrounded by the stabilizer molecule, followed by solvent evaporation.

3.2.1. Synthesis of PLGA NPs by Nanoprecipitation Method

With the aim of optimising the production process, the effect of the concentration of the hydrophobic drug (*o*-carborane) was first investigated. Experimentally, PLGA NPs were synthetized by dissolving 20 mg *o*-carborane:PLGA in 2 mL of solvent mixture. The following amounts of *o*-carborane: 0.2, 1, 2, 3 and 4 mg, were dissolved with PLGA with the following copolymer ratios: 85:15, 75:25 and 50:50 (MW: 20, 40 and 50 kDa), corresponding to 1, 5, 10, 15 and 20 wt % of the *o*-carborane in weight with respect to the total mass. Two different solvent mixtures were used depending on the stabilizer used. A mixture of acetonitrile/dichloromethane 19:1 (v/v) was used as the solvent for the preparation of PEI-stabilised NPs, and acetonitrile/dimethyl sulfoxide/dichloromethane 10:2:1 (v/v/v) was used for the preparation of BSA-stabilised NPs. The resulting solution was added dropwise, using a syringe pump (0.1 mL min^{-1}) to a 50 mL of anti-solvent aqueous solution containing BSA (20 mg mL^{-1}, pH 7.4) or PEI (50 mg mL^{-1}, pH 8.0), under magnetic stirring (800 rpm). Immediately after, ultrapure water (80 mL) was added to avoid coalescence. During this addition, the solution became milky and turbid due the formation of emulsion droplets. The turbidity disappeared over the following hours due to solvent evaporation.

To remove the excess of solvent, the suspension was kept under agitation for 6 to 16 h. Excess of surfactant was eliminated by centrifugation (9 kRCF, 15 min, r.t.) and removal of the supernatant. The pellet was finally resuspended in ultrapure water for 10 minutes in a sonication bath. The centrifugation process was repeated three times, and the final pellet was resuspended in 1 mL of ultrapure water.

The resulting NPs were subsequently characterised using different techniques including scanning electron microscopy (SEM), transmission electron microscopy (TEM), zeta-potential and dynamic light scattering (DLS).

Table 3.1 Sizes and ζ-potential values of NPs prepared by nanoprecipitation method with PLGA of three different compositions with increasing amount of *o*-carborane.

DLS (nm)	carborane	1 %	5 %	10 %	15 %	20 %	ζ-pot (mV)
PLGA-BSA	85:15	227 ± 16	270 ± 12	291 ± 26	351 ± 9	~	-24 ± 4
	75:25	339 ± 9	175 ± 5	259 ± 17	~	~	-12.3 ± 0.3
	50:50	303 ± 48	~	~	~	~	-5.4 ± 0.4
PLGA-PEI	85:15	236 ± 23	351 ± 9	323.4 ± 8	~	~	35 ± 1
	75:25	383 ± 18	~	~	~	~	36 ± 2
	50:50	323 ± 8	~	~	~	~	38 ± 1

~Refers to non-uniform particles or aggregation.

The average hydrodynamic size increased when higher amounts of the hydrophobic drug (*o*-carborane) were incorporated into the NPs (Table 3.1). In all cases except PLGA-BSA NPs, 85:15 copolymer ratio, the addition of > 10 % of *o*-carborane resulted in the formation of large particles that could not be properly characterised by DLS. SEM images revealed spherical particles with non-regular shapes with deformations and pores (Figure 3.2).

As mentioned in Section 1.2, the precipitation method is limited by multiple factors including supersaturation, precipitation, growth, and condensation. When the concentration of *o*-carborane increases, the hydrophobic composition of the solvent solution containing the polymer and the *o*-carborane decreases the critical supersaturation concentration. This leads to a faster nucleation step with uncontrollable coalescence growing, due to the absence of available monomers, which are sequestered.

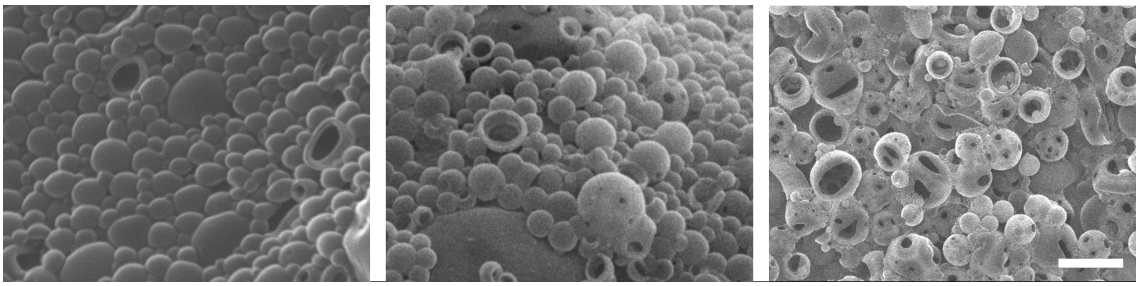

Figure 3.2. SEM images of PLGA-PEI NPs with 1, 5 and 10 wt % *o*-carborane (*left to right*), showing an increased quantity of pores and irregular shapes. Scale bar 500 nm.

In addition to the problems discussed above, it was noticed that a long time was required to completely evaporate the solvent (6-16 h). These long times are not appropriate for translation of the conditions to the preparation of labelled NPs (or NPs with the radiolabelled drug entrapped), as the positron emitters used in the context of this PhD thesis to investigate biological fate of the NPs have relatively short physical half-lives (see below). Considering: (i) the low percentage of hydrophobic content loaded in the NPs; (ii) the relatively large particle sizes obtained, which might be inappropriate for intravenous administration; and (iii) the limitations in the preparation time, we decided to discard this method and explore other experimental approaches.

3.2.2. Synthesis of PLGA NPs by emulsification evaporation solvent method

The effect of *o*-carborane load on the properties of the NPs was also assessed using the emulsification/evaporation (ESE) method. This method is based on the preparation of an oil in water (O/W) emulsion comprising: (i) an organic phase, total or partially insoluble in water, containing the polymer and the hydrophobic compound; and (ii) an aqueous phase containing the stabilizer. The emulsion is generated by phase disruption using mechanical (*i.e.* sonochemical) forces, capable of breaking the superficial tension and resulting in the generation of small droplets of organic solvent (size range from microns to millimetres) surrounded by the aqueous phase.

The PLGA NPs were prepared by dissolving different amounts of *o*-carborane (0.2, 1, 2, and 6 mg) and the corresponding amount of PLGA to a final mass of 20 mg (copolymer ratios 85:15, 75:25 and 50:50 and molecular weights of 20, 50 and 40 kDa, respectively) in dichloromethane (1 mL). The resulting solution was introduced in a 5 mL flat bottom glass vial (11 x 30 mm) containing a magnetic stirrer (3 x 6 mm) with 3.5 mL of an aqueous solution of BSA (20 mg mL^{-1}) or PEI (50 mg mL^{-1}). The reagents were cooled at 4 °C before use, and the vial was maintained in an ice-water bath. After 30 second of magnetic stirring (800 rpm) the sonication tip was introduced *ca.* 12 mm below the level of the liquid, and the sonication was started. Immediately after sonication, the liquid was poured over 80 mL of ultrapure water under magnetic stirring (600 rpm) for 2-5 hours in a fume hood to evaporate the organic solvent. The dilution was carried out to avoid coalescence between particles before the organic solvent was completely evaporated.

Elimination of the excess of surfactant was achieved by centrifugation (9 kRCF, 15 min) and removal of the supernatant. The pellet was finally resuspended in ultrapure water for 10 minutes in a sonication bath. The centrifugation process was repeated three times, and the final pellet was resuspended in 1-5 mL of ultrapure water. The sample was finally filtered to remove big aggregates. The resulting NPs were characterized by electron microscopy, Dynamic Light Scattering, and Infrared Spectroscopy.

A. Optimisation of the sonication parameters

The sonication process has a huge impact on the final properties of the NPs, and the sonication parameters to be applied might be influenced by the composition of the solvent, O/W ratio, partition coefficient of the components in both phases, and some physical aspects such as the shape of the vial, the volume

of the two phases, and the equipment available.[148] Parameters that can be modulated include the power and the amplitude of the pulses, sonication time, temperature, number of cycles, energy diffusion, and tip shape, among others.

The synthetic procedures were optimised considering that, for *in vivo* applications, all the preparation should be carried out in a radiation-controlled facility. Additionally, NP sizes below 200 nm are desirable for intravenous administration, as larger particle sizes may lead to rapid accumulation in the lungs and the liver, thus resulting in a dramatic decrease in bioavailability. The PLGA polymer ratio selected was 85:15, as previous experiments (see 3.2.1) had shown that this ratio facilitates the incorporation of a higher percentage of hydrophobic drug, probably due to the higher hydrophobic character of this copolymer with respect to those with 75:25 and 50:50 ratios. At this stage, the content of *o*-carborane was fixed to 5 %.

In brief, NPs were synthetized by dissolving 1 mg of *o*-carborane and 19 mg PLGA (copolymer ratio 85:15, molecular weight of 20 kDa) in 1 mL of dichloromethane. The solution was introduced in a 5 mL flat bottom glass vial (11 x 30 mm) containing a magnetic stirrer (3 x 6 mm) with 3.5 mL aqueous solution of BSA (20 mg mL^{-1}) or PEI (50 mg mL^{-1}). The effect of the sonication process on NP properties was investigated by modifying the amplitude range (20, 25 and 30 %), sonication times (from 10 to 90 seconds) and the concentration of stabiliser (2 % for BSA, 5 % for PEI).

Irrespectively of the amplitude, it was observed that sonication times greater than 60 seconds produced an increase in the temperature of the solution up to 40 °C. Consequently, bubbles were formed due to the evaporation of dichloromethane. This resulted in increased polydispersity index (PDI) values (Figure 3.3). When amplitudes of 25 and 30 % were used, such temperature

increase was observed at shorter times, and the resulting NPs displayed smaller hydrodynamic diameters and higher PDI values (Figure 3.3).

The most uniform particles, with hydrodynamic size of *ca.* 150 nm, were obtained when amplitude of 20 % was applied for 45 seconds. These conditions were used to obtain the NPs in the next chapter.

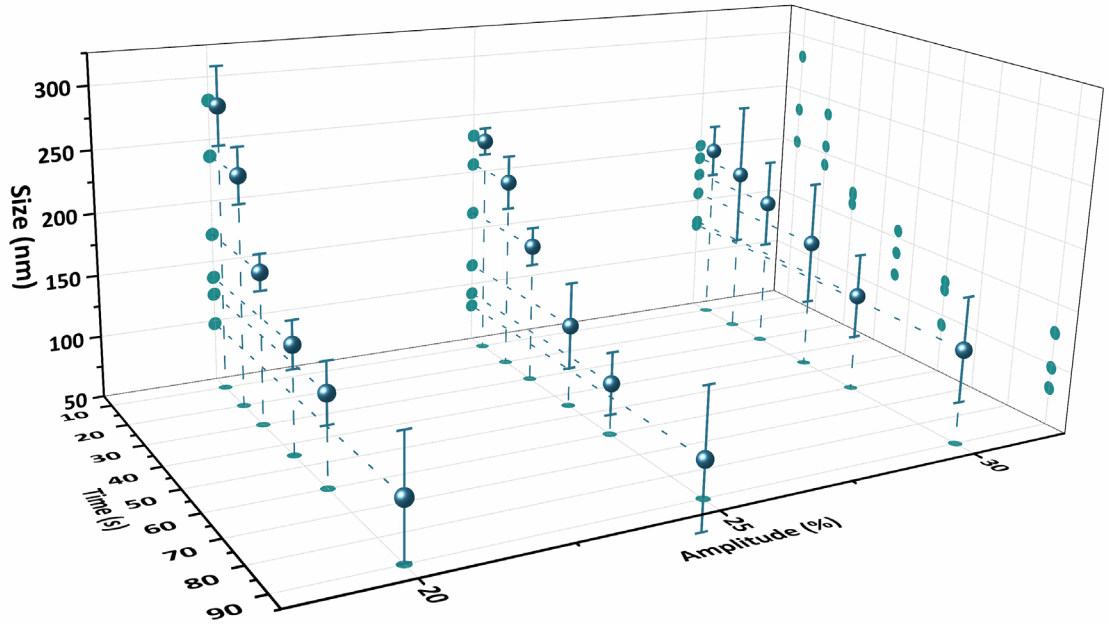

Figure 3.3. Hydrodynamic size of NPs as a function of sonication amplitude and sonication time applied during their preparation. Each experiment was repeated at least 10 times.

B. Effect of hydrophobic compound concentration in PLGA-BSA NPs

One critical factor on the properties of the NPs is the amount of *o*-carborane encapsulated. Thus, we next explored the effect of the amount of *o*-carborane on PLGA-BSA NPs, using different PLGA ratios. NPs were characterised by means of SEM and DLS. For this set of experiments, sonication amplitude and time were fixed at 20 % and 45 seconds, respectively.

The increase in the amount of *o*-carborane resulted in the formation of a mixture of large and irregular particles, empty capsules, leaky particles, and small particles (see Figure 3.4, right column, 15 % of *o*-carborane).

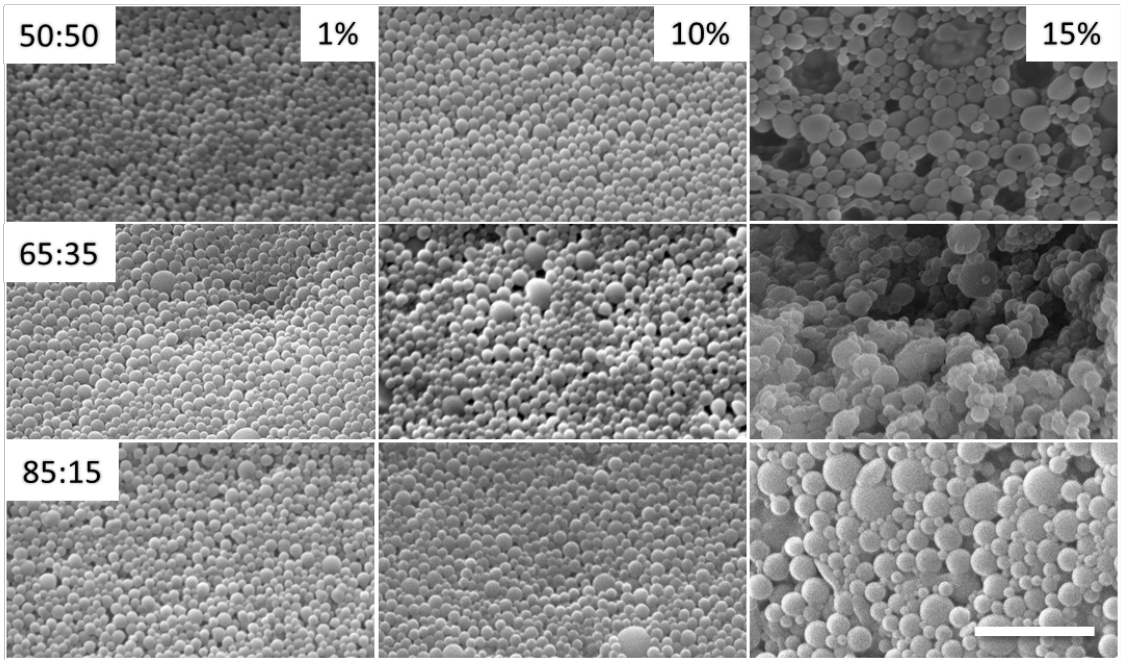

Figure 3.4. SEM images of PLGA-BSA coated NPs obtained by emulsification method, with the polymer ratios 50:50, 65:35 and 85:15 with *o*-carborane concentration of 1, 10 and 15 % (*left to right*). Scale bar of 1 μm.

As expected, when higher lactide/glycolide ratios were used, which results in higher hydrophobic character of the polymer, the effect of the concentration of *o*-carborane on the properties of the NPs was less severe, as already suggested by the results obtained in Section 3.2.1 using the nanoprecipitation method.

The dynamic stability of the NPs was investigated by performing DLS analysis at different times after preparation. With that aim, samples were kept under continuous stirring. DLS results (Figure 3.5) reveal, first, that NPs with a higher content of *o*-carborane have larger size (*ca.* 500 nm for NPs containing 15 % of *o*-carborane *vs* 250 nm for NPs containing 5 % of *o*-carborane); and second, that NPs containing 15 % of *o*-carborane tend to aggregate over time, suggesting low stability in solution, probably due to exposed hydrophobic domains capable of interacting. Contrarily, NPs with 5 % *o*-carborane remained stable over the duration of the study.

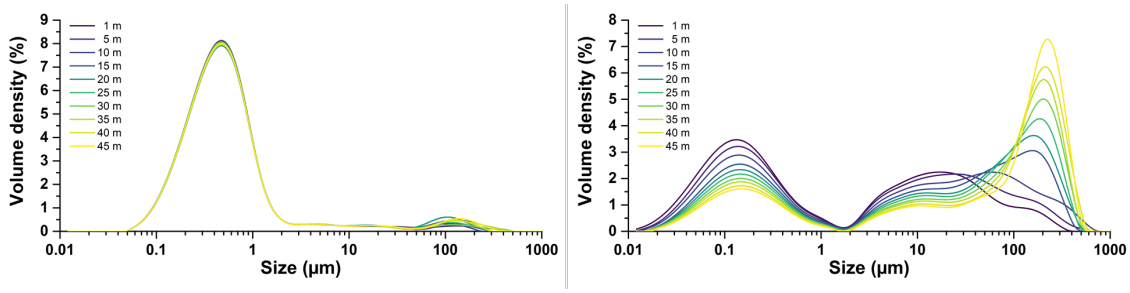

Figure 3.5. DLS measurements under continuous stirring of PLGA-BSA NPs (65:35) with 5 % (*left*) and 15 % of *o*-carborane (*right*).

C. Effect of hydrophobic compound concentration in PLGA-PEI NPs

We next explored the effect of the drug load on the properties of PLGA-PEI NPs. When PEI was used as the stabiliser, larger sized, prone to aggregate particles were obtained in comparison with PLGA-BSA NPs, probably due to the lower stabilising capacity of PEI in the presence of *o*-carborane.

PLGA-PEI NPs with average size of 250 nm and ζ potential values ranging from 30 to 35 mV could be obtained when amounts of *o*-carborane < 1 % were used. An increase in the *o*-carborane content produced an acute effect in nanoprecipitation, due to the interaction between the polyelectrolyte stabilizing the carborane molecule and the micelles (Figure 3.6 right column).

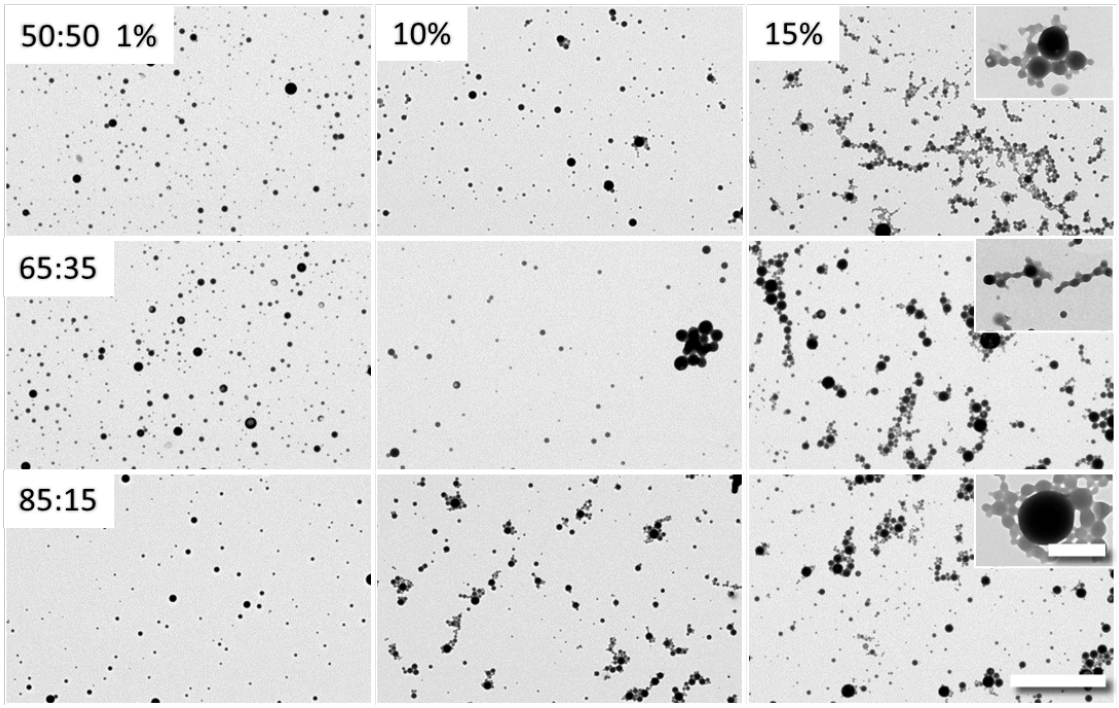

Figure 3.6. TEM images of PLGA, PEI coated NPs obtained by nanoprecipitation method, with the polymer ratios 50:50, 65:35 and 85:15, with increasing amount of *o*-carborane (*from left to right* 1 %, 10 % and 15 %). Scale bar of 5 µm. *Inset* scale bar of 1 µm.

The behaviour of the particles coated with PEI under dynamic conditions is clearly different from that observed for BSA coated particles. Particles with 5 % concentration of *o*-carborane aggregate immediately (Figure 3.7

left), indicating the incipient aggregation of certain populations. This effect is more significant for NPs with a 15 % content in *o*-carborane (Figure 3.7 right). The instability of the particles prevents their use for *in vivo* applications.

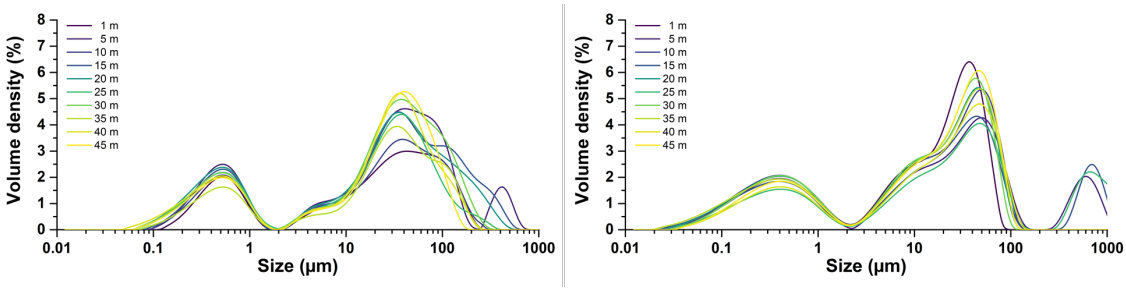

Figure 3.7. DLS measurements under continuous stirring of PLGA-PEI NPs (65:35) with 5 % (left) and 15 % of o-carborane (right).

D. Hydrophobic compound encapsulation efficiency

We next explored the efficiency in the encapsulation of *o*-carborane into the polymeric NPs. With that aim, the amount of *o*-carborane in the particle was investigated by means of infrared (IR) spectroscopy.[149] As it can be seen in the IR spectra of *o*-carborane (Figure 3.8), The B-H (*ca.* 2590 cm^{-1}) and C-H stretching signals (*ca.* 3080 cm^{-1}) are clearly separated, thus facilitating the analysis.

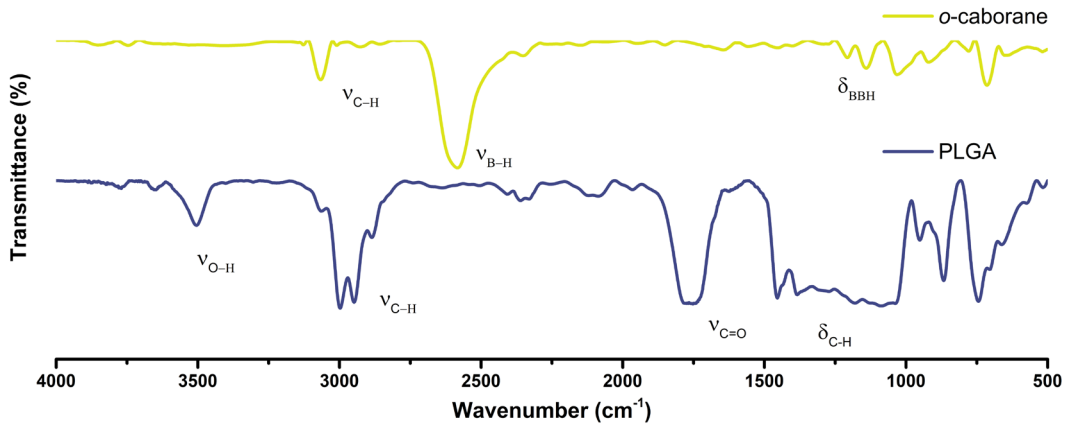

Figure 3.8. Infrared spectra of *o*-carborane (*yellow*) and PLGA (*blue*) with indication of the characteristic stretching and bending bands of both compounds.

A calibration curve was first generated by dissolving different amounts of *o*-carborane and a fixed amount of PLGA in dichloromethane. The solution was placed on a cylinder-shaped (13 mm diameter) support and dried overnight at room temperature. Then the spectra were collected either using the film, or by preparing a pellet with potassium bromide (60 mg). Both approaches yielded equivalent results, although the maximum *o*-carborane/PLGA ratio was fixed at 30 %, as concentrations above this value resulted in poor consistency of the film and appearance of different phases.

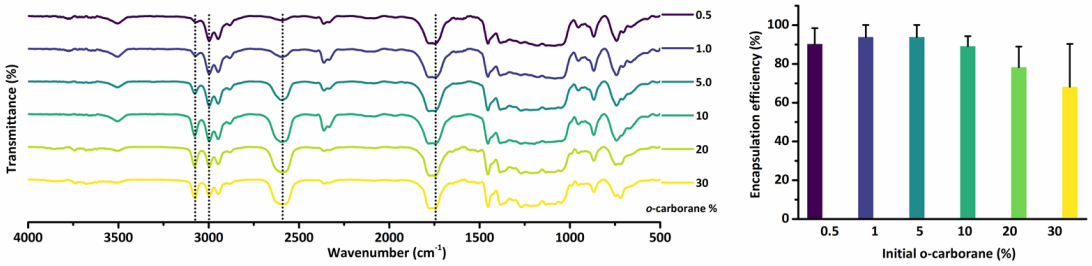

Figure 3.9. Infrared spectra (with the designated vibrational modes) of PLGA with increasing content of *o*-carborane normalized with the stretching band of carbonyl at $\nu_{C=O}$ 1738 cm^{-1} (*left*); bar graph of encapsulation efficiently of PLGA-BSA NPs evaluated by infrared spectroscopy (*right*).

After acquiring the spectra (Figure 3.9) the calibration curve was generated by normalizing the spectra to the carbonyl peak (1750 cm^{-1}) and evaluating the intensity the band at 2590 cm^{-1}. The obtained Equation 7 was used to determine the amount of *o*-carborane in the NPs.

Equation 7 $$y = 0.0095 \cdot x + 0.0152;\ R^2 = 0.998$$

Encapsulation efficiencies as high as 95 % could be achieved when *o*-carborane/PLGA ratios up to 10 % were used for PLGA-BSA NPs, and these values raised to quasi-quantitative incorporation for PLGA-PEI NPs.

E. Drug encapsulation polydispersity

The polydispersity in drug encapsulation was next explored at different *o*-carborane/PLGA ratios by the use of Electron Diffraction X-Ray Spectroscopy (EDXS). At higher *o*-carborane ratios and maintaining the stabiliser unchanged, increased irregularities in particle shape could be observed by TEM (Figure 3.10). Higher polydispersity could also be observed as previously described in Section A.

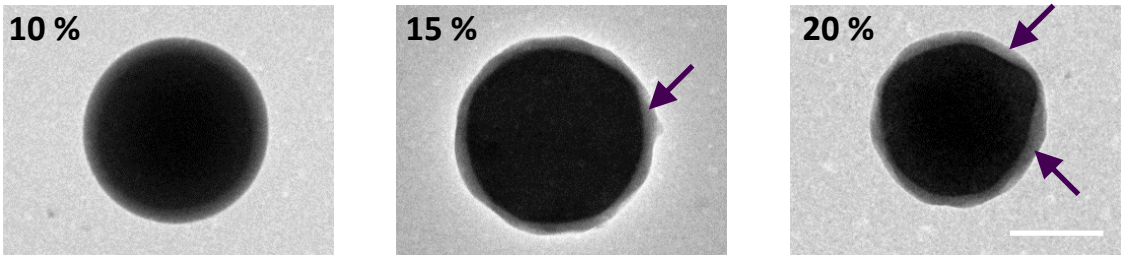

Figure 3.10. TEM images showing surface irregularities of NPs with added *o*-carborane 10, 15, and 20 % (*left to right*). Scale bar of 100 nm.

To evaluate differences in boron concentration within each particle, Energy Dispersive X-ray Spectroscopy (EDXS) of selected areas were carried out on PLGA-BSA NPs with a content of *o*-carborane between 10 to 20 %. EDXS analysis is a complex technique that requires the consideration of different parameters (excitation source, depth profile, sample composition, topography, interaction drop-surface) and hence it cannot be considered as a fully quantitative technique.[150,151] The analysis of light elements with low energies leads to high absorption in the detector and the specimen, and the detection efficiency decreases when the beam energy increases. Still, and in spite of these limitations, EDXS can be used to determine qualitative parameters with high spatial resolution, and performs reasonably well to obtain comparative analysis of similar samples.[152] In the case of NPs, the profile can be used to determine the composition of an element inside a particle.

In our case, EDX analysis was performed in scanning transmission electron microscopy (STEM) with a bright field detector to acquire the image and the EDX detector for the compositional analysis. The EDX signal was recorded ensuring a minimum of 10^3 counts in the range of interest (0.15 to 4.0 keV). The analysis of the peak corresponding to boron band (Kα = 0.185 keV) is challenging, due to the proximity of the carbon band (Kα = 0.277 keV) and the background of the support. The nanoparticles analysed have a majority elemental composition of boron, carbon, nitrogen (Kα = 0.393 keV) and oxygen (Kα = 0.525 keV). For our

samples, the signal from the background was subtracted with the INCA Software (Oxford Instruments), and the sum of the signals obtained of the four elements (B, C, N and O) will correspond with the total NP composition. For the latter analysis, the ratio B/C was obtained considering the total elemental composition.

A clear grid region without visible particles was analysed to evaluate the presence of scattered signals coming from the detector, the grid, and the microscope composition elements (Copper, Silicon and Iron, among others). The signals coming from these elements were deconvoluted to estimate the semi-quantitative atomic percentage of the elements of interest of the analysed areas (Boron, Nitrogen, Carbon and Oxygen). The assignment,[153–155] estimations, quantification, and measurements were also carried out with the INCA Software (Oxford Instruments).

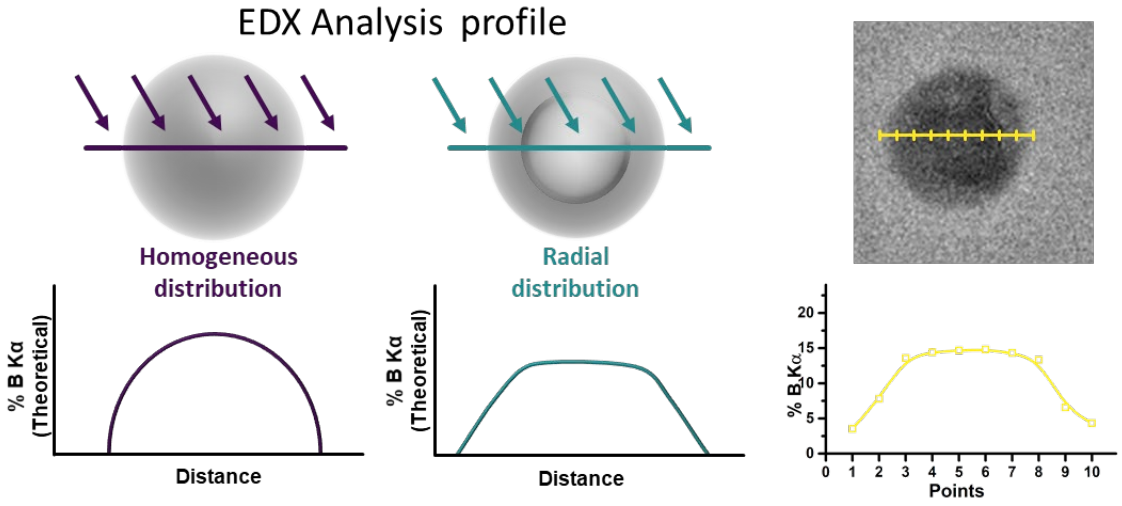

Figure 3.11. Representative EDX relative analysis abundance of a dense particle (*left*) and hollow particle (*middle*), and PLGA-BSA NPs with the respective point analysis of relative boron signal percentage.

The analysis along the NP surface suggests that *o*-carborane is not uniformly distributed in the polymeric matrices. Instead, the profile obtained suggests a radial distribution (Figure 3.11). Because the NPs are spherical in shape and thorough mixing is applied before sonication, we hypothesize that the radial

distribution of *o*-carborane occurs at the curing stage, when dimethyl chloride is displaced, and polymer chains are rearranged. This radial distribution was observed in all particles, irrespective of the stabilizer and the polymer/copolymer ratio.

3.2.3. Radiolabelling of PLGA NPs

One of the major advantages of nuclear imaging is the ability to use small amounts of radiolabelled material to evaluate the biodistribution of chemical or biological entities *in vivo* and at the whole-body level. The application of nuclear imaging requires as the first step the radiolabelling of the molecule to be investigated, and in the context of Nanomedicine, different labelling approaches have been developed over the years.[156,157]

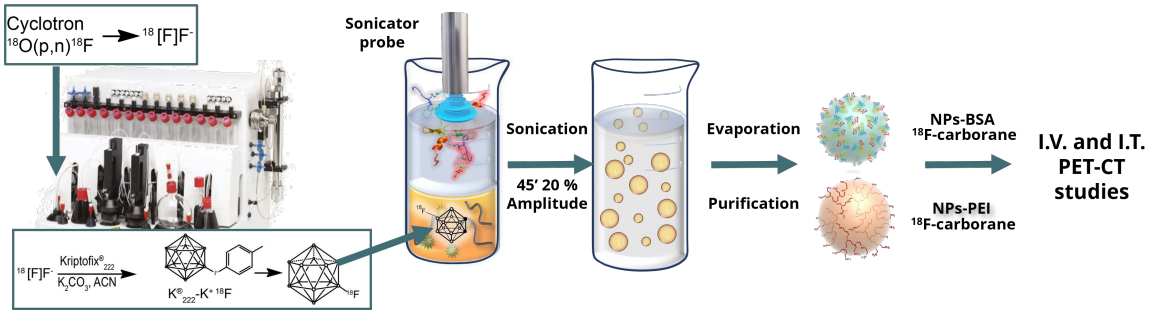

Figure 3.12. Scheme of the radiolabelling reaction for the incorporation of ^{18}F-*o*-carborane in PLGA NPs.

In this PhD thesis, we decided to investigate the effect of the nanocarrier on the biodistribution of the hydrophobic drug, with loading ratios up to 10 %. Hence, our approach was based on the incorporation of the radiolabel on the hydrophobic drug. Among all positron emitters, fluorine-18 (^{18}F) was selected, as: (i) it has a relatively long physical half-life of 110 min, which enables preparation of the NPs and subsequent imaging studies; (ii) it can be readily produced in the cyclotron available at CIC biomaGUNE; and (iii) a method for

the radiolabelling of *o*-carborane has been already developed in the Radiochemistry and Nuclear Imaging Group at CIC biomaGUNE.

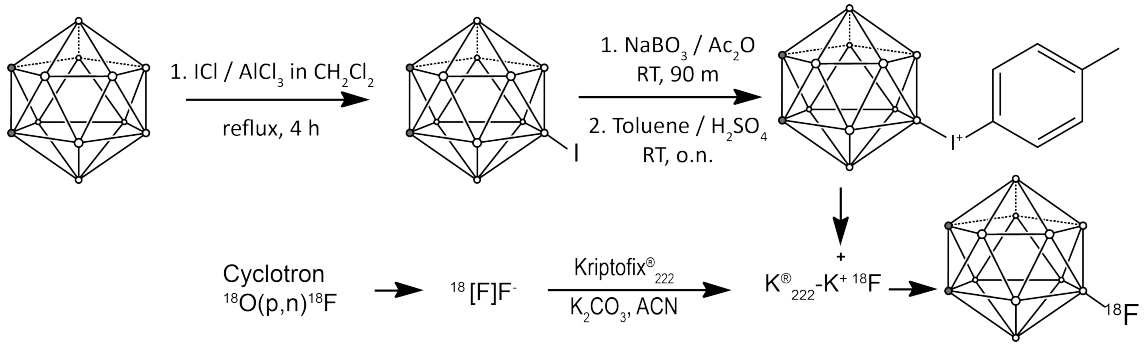

Figure 3.13. Scheme of synthesis and labelling to obtain ^{18}F-*o*-carborane.

Preparation of 9-[^{18}F]-*o*-carborane, was performed through a three-step sequence (Figure 3.13).[158] In the first step, an equimolar amount of *o*-carborane (1.0 g, 7.1 mmol) is reacted with iodine monochloride (1.14 g, 7 mmol) in presence of $AlCl_3$ (0.1 g) in dry methylene dichloride (DCM, reagents added in iced-water bath) and under inert atmosphere, and subsequently refluxed for 4 h, to obtain mono substituted 9-Iodo-*o*-carborane following a previously reported method.[159] The mixture was poured into 20 mL ice-cooled water, the organic phase was separated, and the aqueous phase was extracted with three portions of 15 mL of diethyl ether. The extracted organic portions were washed with 10 % aqueous sodium thiosulfate ($Na_2S_2O_3$) solution to neutralize iodine unreactive species, washed with water, and dried over $MgSO_4$. The reaction of 9-Iodo-*o*-carborane with toluene in presence of $NaBO_3$ under strong acidic medium (H_2SO_4) yielded a powdered white solid of *p*-tolyl-(9-*o*-carbonaryl) iodonium bromide (1.2 g, yield 45 %).[160]

Structural characterisation of the precursor for radiolabelling was achieved by means of ^{11}B and ^{1}H-nuclear magnetic resonance (NMR), which confirmed the position of all peaks according to literature.[158]

After characterisation of the precursor, the radiolabelling step was tackled. The radionuclide ^{18}F, was generated by proton irradiation of $[^{18}O]H_2O$ via the $^{18}O(p, n)^{18}F$ nuclear reaction; $[^{18}F]F^-$ was trapped in an anion exchange resin and eluted with 0.5 mL of K_2CO_3 (50 mg mL^{-1}) and 1 mL CH_3CN containing 5 mg Kryptofix®2.2.2. After azeotropic evaporation of the solvent, dried potassium $[^{18}F]$fluoride-complex was obtained, and subsequently 5 mg of the precursor *p*-tolyl-(9-*o*-carbonaryl) iodonium bromide dissolved in 1 mL of 2-methyl-2-butanol:CH_3CN (1:9) was added to the reaction vessel and heated up to 100 °C for 20 min. The crude reaction was diluted with 2 mL of mobile phase (CH_3CN:NH_4HCO_2 pH 3.9, 40:60) and injected in a semi-preparative C-18 column (5 mL min^{-1}), to purify the product from the undesired radiolabelled by-products.

The radioactive peak corresponding to the labelled compound (retention time 25 min) was collected and poured on 30 mL of distilled water, and subsequently adsorbed in a solid phase extraction (SPE) cartridge. The SPE was washed with 5 mL of ultrapure water to remove mobile phase solvent residues and dried for 2 minutes with helium. Finally, ^{18}F-*o*-carborane was eluted from the cartridge with 1 mL of dichloromethane to the final collection vial.

After purification, radio-HPLC was carried out to evaluate the purity of the compound. Radioactive chromatographic profiles confirmed radiochemical purity > 98 %. The overall decay-corrected radiochemical yield was > 60 %.

The preparation of the labelled NPs was achieved by using the same preparation protocol described above, but spiking the initial mixture of *o*-carborane/PLGA with a small amount (10 μL) of 9-$[^{18}F]$-*o*-carborane just before sonication. The sonication method for the synthesis of the particles was used due

the shorter times of encapsulation observed, the lower amount of solvent required and the higher evaporation ratio of dichloromethane.

In brief, 100 μl of ^{18}F-*o*-carborane (*ca.* 70 MBq; as obtained after purification and reformulation) was added to a vial containing 2 mg of PLGA, 0.1 mg of *o*-carborane, and 3 mL of either BSA (2 %) or PEI (5 %), under magnetic stirring. The biphasic solution was stirred for 30 seconds and sonicated for 40 seconds at an amplitude of 25 %. The resulting mixture was poured into ultrapure water (12 mL) and stirred under nitrogen flow until complete evaporation of methylene chloride. The particles were purified and washed by centrifugation as previously described. The radiochemical yield was calculated by dividing the amount of radioactivity in the final pellet by the sum of the amount of radioactivity in all the supernatants plus the pellet. The RCY was 75-86 % for PLGA-BSA and 82-95 % for PLGA-PEI NPs. The purified and labelled PLGA NPs were obtained 5 hours after the end of the bombardment of the production of [^{18}F]fluorine.

After production, we first investigated the radiochemical stability in saline buffer, serum, and simulated body fluid (SFB). With that aim, NPs were incubated in the different media from 30 min to 6 hours at 37 °C, collected, centrifuged and the amount of radioactivity in the pellet and the supernatant was measured. In all cases, radiochemical stability was higher than 90 % after 6 hours of incubation.

3.2.4. Biodistribution of NPs after Intravenous administration

All animal experiments described in the thesis were conducted in accordance with the Spanish policy for animal protection (Royal Decree 53/2013), which meet the EU Directive 2010/63/EU requirements regarding the animal welfare and the protection of the animal used in experimental procedures. All experiment

procedures were previously approved by the Ethical Committee and accredited local government.

To evaluate the biodistribution of the NPs, ^{18}F-labelled particles (3.7-37 MBq) were intravenously administered to wild type (WT) rats and PET imaging studies were performed. Dynamic images were acquired during the first hour after administration. Then, animals were recovered from anaesthesia and imaging sessions (static) were conducted at different times up to 4 hours post-administration.

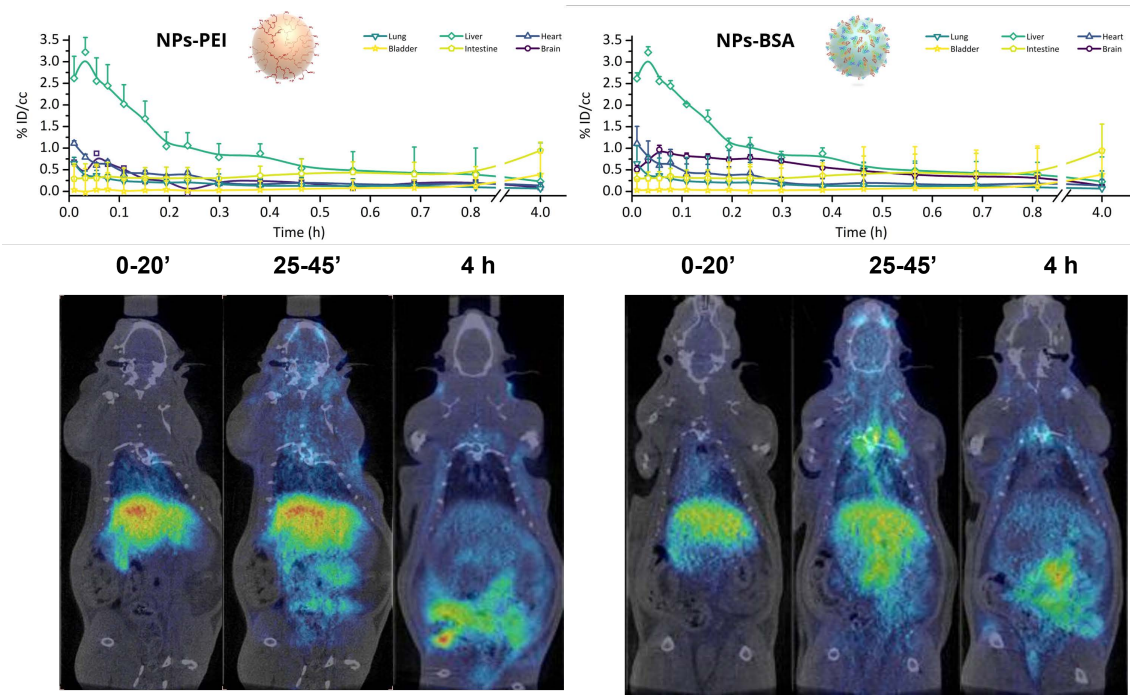

Figure 3.14. Concentration of radioactivity in different organs at different times after intravenous administration of PLGA NPs stabilized by PEI (*left*) and BSA (*right*). Representative PET-CT images (coronal slices) for different time frames are shown.

Previous studies carried out in our group have shown that particles with similar physiochemical properties are rapidly accumulated in organs of the mononuclear phagocytic system (MPS, formerly known as the reticuloendothelial system or RES), mainly in the liver and the spleen.[161–165] Accordingly, the studies conducted in this section, as show in Figure 3.14,

showed initial accumulation of NPs in the liver and to a lower extent in the spleen. Interestingly, elimination of the radioactivity through the intestinal tract was observed at long times after administration (t = 3 h). These results may suggest that the radiolabelled species, this is *o*-carborane, is release from the NPs and eliminated. Such elimination occurred irrespective of the stabiliser (BSA or PEI).

3.2.5. Biodistribution of NPs after Intratracheal administration

Polymer Nanoparticles can be used as DDS for pulmonary administration. Contrary to other materials that can induce lung inflammation and long retention in the lungs, polymeric materials are biocompatible.[166–168] Additionally, pulmonary administration is a very interesting alternative to intravenous administration, especially when the lung is the target organ, as maximum accumulation of the DDS (and hence the drug) can be achieved at the side of action, thus maximizing therapeutic efficacy while minimising off-target side effects.[169]

Taking this into account, we next investigated the biodistribution of the labelled *o*-carborane encapsulated in the NPs after pulmonary administration. Such administration was performed *via* endotracheal insufflation using a Penn-Century's FMJ-250 high Pressure Syringe. The Micro Sprayer® Aerosolizer - Model IA−1C produces a droplet size with homogenous distribution, with Mass Median Diameter (MMD) of 16-22 μm. Despite the droplet size is clearly above the optimal value for pulmonary administration into small rodents (5 μm)[170–172] and accumulation in major airways can be expected, this administration system allows the deposition of *ca.* 90 % of the nebulised material into the lungs, as previously reported.[173]

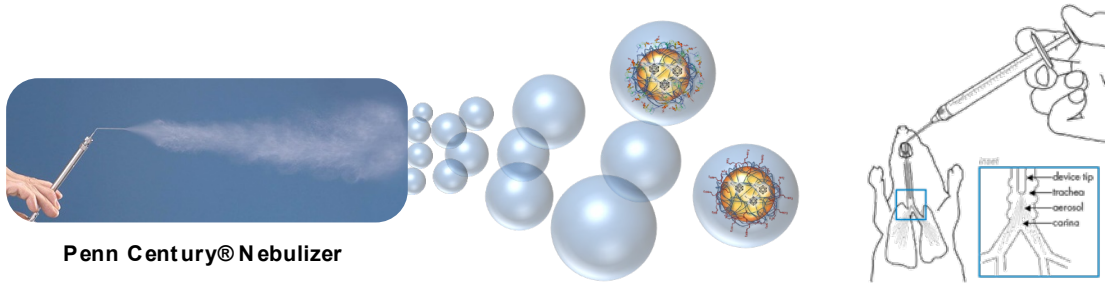

Figure 3.15. Image of a Penn Century Nebulizer (*left*) and scheme of nebulized droplets containing NPs (middle) and scheme of positioning place of the device tip in the carina (*right*).

Experimentally, animals (n = 4) where deeply sedated by inhalation of 5 % isoflurane in pure O_2. Subsequently, the animal was placed on the intubation bed, the tip of the Sprayer was introduced above the carina junction, and 50 µl of labelled suspension containing *ca.* 37 MBq of labelled NPs were nebulized at the time the animal inhaled. The animals were immediately positioned in the scanner to acquire PET-CT images.

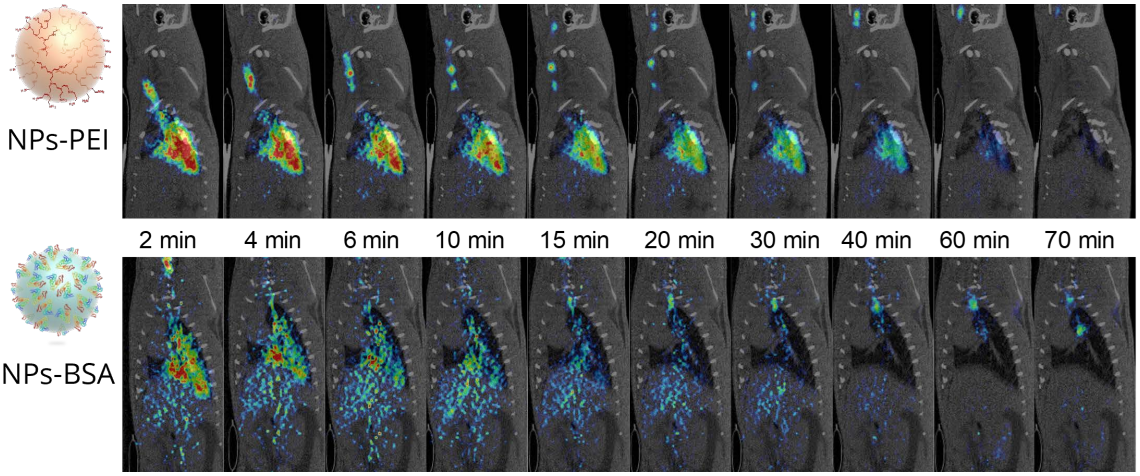

Figure 3.16. Representative PET-CT (sagittal slices) images acquired at different time points after intratracheal administration of PLGA NPs coated with PEI (*upper images*) and BSA (*lower images*). Activity values of the images were normalized to the initial maximum value of the average images.

The visual inspection of PT-CT imagens shown in Figure 3.16, reveals longer retention times of PEI coated than for BSA coated NPs. Quantification of the images (see Figure 3.17) confirmed a fast elimination from the lungs. Indeed, the retention in the lungs is lower than expected, as previous studies carried out in

our research group with NPs have shown that these can stay in the lungs for long times.[174,175] Based on our previous results, we hypothesize that the labelled *o*-carborane is released from the NPs and subsequently translocated from the lungs to the bloodstream and to other organs, mainly the liver, with posterior elimination through gastrointestinal tract.

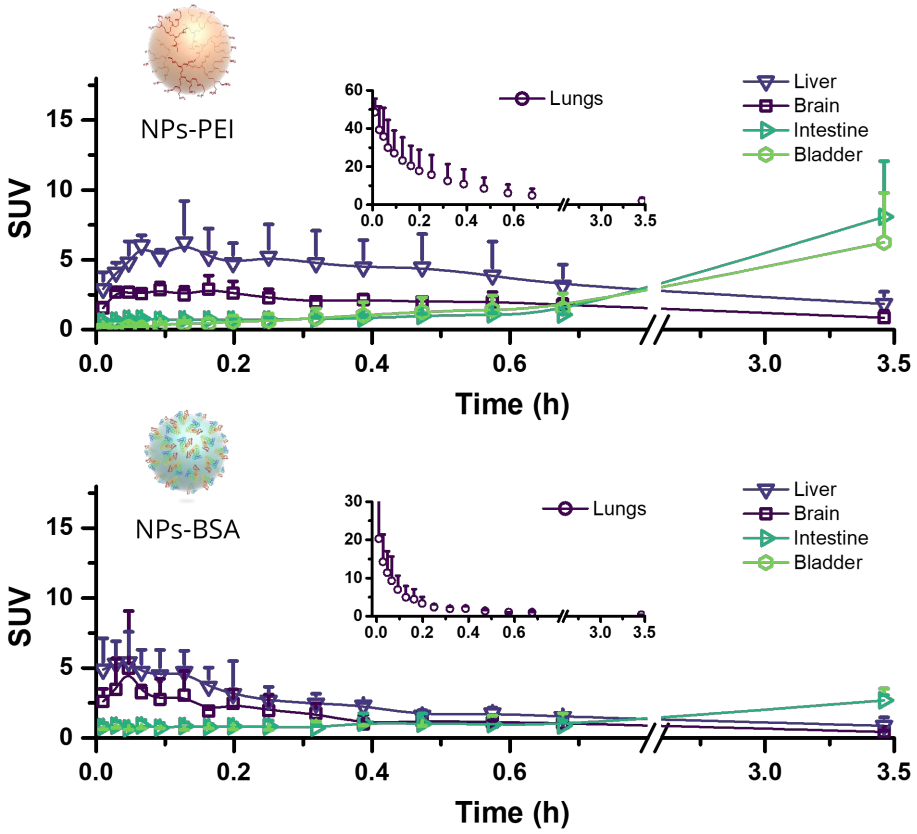

Figure 3.17. Standardized Uptake Values of mayor organs in rat healthy animals after intratracheal instillation with a micro sprayer of PLGA-PEI (*top*) and PLGA-BSA (*bottom*), with an *inset* of the lung uptake.

This, to some extent, can be explained by the properties of *o*-carborane.[176] Indeed, small hydrophobic compounds can rapidly escape from PLGA particles, due their porosity.[136]

3.3. Summary and Conclusions

In this chapter, we describe the preparation of PLGA NPs, loaded with *o*-carborane for subsequent radiolabelling, and stabilised either with BSA or PEI.

Two preparation methods (Nanoprecipitation and Emulsification Evaporation Solvent) were evaluated, and the effect of different factors on the quality of the NPs was investigated. In general terms, the preparation of NPs stabilised with PEI is less reproducible than the preparation of NPs stabilised with BSA.

The NPs prepared by Nanoprecipitation method present a hydrodynamic diameter size between 220 and 320 with narrowed distribution, and ζ potential values of -20 mV for PLGA-BSA and 35 mV for PLGA-PEI nanoparticles.

The effect of different monomer ratios of PLGA was evaluated in the encapsulation efficiency of the hydrophobic molecule *o*-carborane. Results show that monomer ratios resulting in a higher hydrophobic character (greater composition of lactic than glycolic) lead to more efficient encapsulations of *o*-carborane. Encapsulation values > 10 wt % could be achieved only when PLGA 85:15 was used. Still, this method requires long preparation times, incompatible with the short half-life of positron emitters used in this work.

The NPs prepared by Emulsification method present a hydrodynamic diameter size between 100 and 300, depending on the sonication parameter applied, with similar ζ potential values. When the amount of *o*-carborane incorporated in the NPs increased from 5 to 15 %, increasing irregularities and significant aggregation were observed.

Biodistribution studies in rodents, performed by incorporating ^{18}F-labelled *o*-carborane into the NPs followed by PET imaging, showed accumulation in the liver and spleen with progressive elimination via intestine after intravenous administration, and progressive release from the lungs after intratracheal administration. Based on our previous studies, these results suggest the release of the encapsulated drug.

4. Study of Protein Corona on PLGA NPs

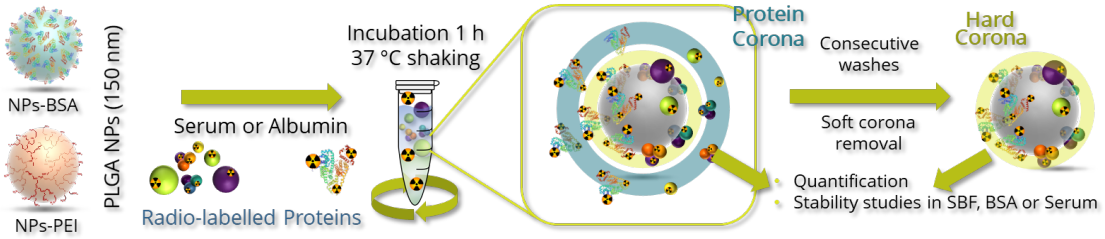

4.1. Introduction

The blood is a fluid connective tissue that is constantly circulating through the blood vessels transporting ions, biomolecules, and cells. The main functions of blood comprise the delivery of nutrients, oxygen, and biomolecules; the distribution of the corporal heat; the defense and hydration of the body; and maintenance of the homeostasis. The pH of the blood is 7.40 ± 0.05 (slightly alkaline) and different salts and buffers keep pH values within this narrow range.

A major part of cells in blood are erythrocytes (99 %). Erythrocytes transport oxygen and carbon dioxide. Other cells also present in blood are white blood cells, and comprise macrophages, monocytes, lymphocytes, basophils, and eosinophils. The fraction of the blood not containing cells is called plasma, which is mainly composed of water (92 %) which contains ions, proteins (these

accounting for 7 % of the total plasma), and cell fragments as exosomes, circulating vesicles or platelets.

Plasma contains different proteins, including Albumin (53 %, 22 mg mL^{-1}, 66 kDa), α1 Globulin (8.4 %, 3.5 mg mL^{-1}, 36 kDa), α2 Globulin (7.4 %, 3.1 mg mL^{-1}, 57 kDa), β Globulin (26.5 %, 11 mg mL^{-1}, 11 kDa), γ Globulin (4.4 %, 1.8 mg mL^{-1}, 160 kDa) and fibrinogen (7 %, 0.3 mg mL^{-1}, 340 kDa).[177] Albumin clearly represents the most abundant protein present in the blood. It is generated in the liver and has an average circulating *in vivo* half-life of 21 days. It is a globular non-glycosylated protein formed by 585 amino acids and has a 66.5 kDa molecular weight.[178] At physiological pH, albumin is negatively charged, and it works as ionic sponge and circulating antioxidant agent,[179] and acts as transporter and coadjutant for multiple molecules as fat-soluble hormones, fatty acids or pharmacological drugs.[180–182]

Albumins have 70 % alpha helix secondary structure with a few random coils, distributed in tree domains I, II and III, with their own A and B sub-domains. Each one has six and fourth helices, with eleven identified binding sites. Seven of the domains are available for fatty acid molecules (capric C10, lauric C12, myristic C14, palmitic C16 and stearic C18), and the other identified sites interact with smaller molecules.[182] Pharmacological molecules such as diazepam, digitoxin, ibuprofen or zidovudine-5-triphosphate are bloodstream transported by albumin, as it happens with the endogenous compound bilirubin.[183]

As mentioned, the second most abundant proteins are the globulins. There are divided in three subgroups, known as alpha, beta, and gamma globulins. The latter provide the defence signalling involved in the immune response and are also known as immunoglobulins or antibodies.[184] The former two, alpha and betta, are responsible for the transport of fat-soluble vitamins (A, D, E and K),

lipids, and iron to the cells. Fibrinogen is a less abundant protein in plasma and its main function is to assist to the clotting process.[185] A minor fraction of the blood corresponds to regulatory proteins, as hormones and enzymes (< 1 %) and other solutes, as gases, wastes or nutrient.

The development in Nanotechnology during the last years has led to the design of nanoparticles with increasing complexity and tailored properties for biomedical applications. When a particle is introduced in the blood torrent, a series of interactions take place between the nanoparticles and the components of the blood. The interaction of nanoparticles with blood is a complex process, and is affected by the flow rate[186], the diffusion of molecules and nanoparticles in blood, shear stress forces during circulation,[187–189] interaction with phagocytic cells and clearance by the mononuclear phagocytic system (MPS). All these aspects are only considered when the studies of the interactions are conducted *in vivo*.

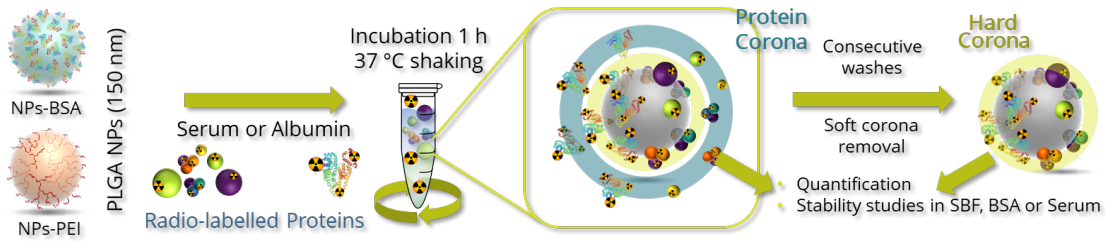

Figure 4.1. Scheme of the formation of protein corona onto nanoparticles, soft corona removal and consecutive studies performed to quantify protein corona and asses the stability of these in different media.

One of the phenomena that may take place when NPs are introduced in the blood stream is the formation of the protein corona (PC). The protein corona is a dynamic mixture of proteins that associate to the surface of NPs when these are exposed to a biological environment. Some of the proteins can be easily exchanged, while others can form covalent bonds with functional groups present at the surface of the NPs. One example is the complement system protein C3b,

which can form ester or amide bonds with amino or hydroxyl groups present on the surface of NPs (Figure 4.2).[190–193] The formation of such bonds leads to activation of the complement, with consequent opsonization and phagocytosis.

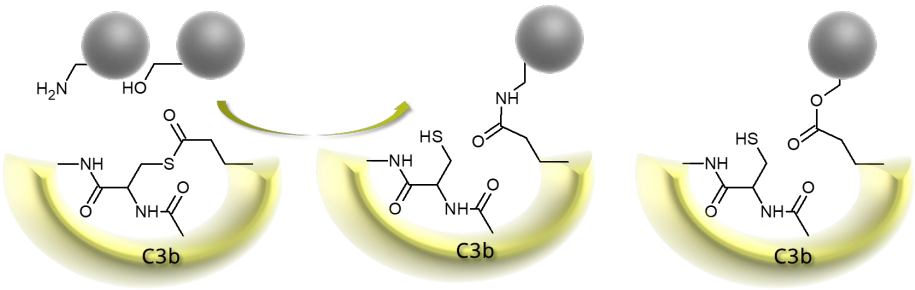

Figure 4.2. Scheme of covalent bond of complement protein C3b to different groups of the nanoparticle surface.

This chapter focuses on the study of PC interaction using nuclear imaging techniques. The NPs evaluated were similar to those described in the precious chapter. More specifically, studies were carried out with PLGA NPs 150 nm diameter sized and stabilized with BSA and PEI (polyethyleneimine, branched). The protein corona was formed using serum or albumin, with the proteins radiolabelled with a radionuclide. The aim of the chapter is the investigation of the stability of a preformed protein corona, by evaluating the release and/or exchange with the media.

4.2. Results and discussion

4.2.1. Serum purification and quantification

Serum was obtained from blood collected through the tail vein of 30-60 days old Sprague Dawley rats. With that aim, rats were anaesthetised, the tail was carefully warmed, and a 25-gauge needle was injected in one of the lateral tail veins to extract blood samples (*ca.* 1 mL), which were collected in BD SST™ Microtainer centrifuge tubes containing clot activator and gel separation phase. The whole blood was clotted by leaving it at room temperature for 30 min and

centrifuged at 1.3 kRCF for 10 minutes at 4 °C to separate both the cells and clotting factors (Figure 4.3). The centrifuge procedure was performed twice to remove small clots recovered from the first supernatant, and the resulting supernatant was aliquoted. This process removes erythrocytes, leucocytes, platelets, and clotting factors, while proteins, electrolytes, hormones, and exogenous substances remain in the supernatant. The purified serum was used to conduct the subsequence protein corona studies.

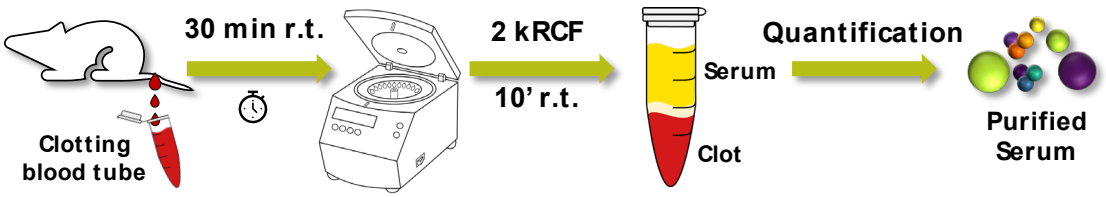

Figure 4.3. Scheme of blood extraction, plasma purification and quantification.

Protein concentration of each batch was determined previously to radiolabelling using a Nanodrop spectrometer in combination with the Pierce™ BCA Protein Assay colorimetric assay. In brief, 100 µl of commercial protein standards at different concentration and two diluted fractions (20 and 50-fold) of the serum, were mixed with 2.0 mL of working reagent (reagent working mix A/B 50:1) and incubated for 30 minutes at 37 °C. After the incubation period, samples were cooled at room temperature and the absorbance was measured by triplicate at 562 nm on a plate reader spectrometer. A calibration curve of absorbance *vs* protein concentration was generated to determine the proteins concentration on serum. The amount of proteins content was 40.2 ± 0.8 mg per mL of serum.

4.2.2. Protein radiolabelling

DL-Tyrosine or 2-Amino-3-(4-hydroxyphenyl)-propanoic acid is one of the twenty basic amino acids. The aromatic hydroxyl group is a reactive group for

protein kinases to add phosphate groups, that trigger subsequent reactions and modulations driven by specific antibodies. Albumin has 18 tyrosine residues, some of them with high reactivity, such as Tyr 411 which is located around the tip of the loop 7.

Tyrosine residues are also known to be ideally suited for the radiolabelling of proteins using radioisotopes of iodine. In the presence of an oxidizing agent, the cation I^+ is generated *in situ*, and reacts with the activated alpha-positions of the hydroxyl group in the aromatic ring. Different oxidising agents have been developed over years. One of the most convenient ones is 1,3,4,6-tetrachloro-3*α*,6*α*-diphenyl-glycoluril (Pierce™ Iodination Reagent, formerly called Iodogen) due to several reasons, including high labelling efficiency,[194] high stability in the reaction media, water insolubility,[195] and very good performance even at very low protein concentrations.[196]

In this PhD thesis, the iodination was performed by the incubation of 500 μg of BSA (≈ 25.0 μl, 20 mg mL^{-1}, phosphate buffer 10 mM pH 7.4) or 400 μg of purified Serum (≈ 14.3 μl, 35 mg mL^{-1}), in low binding protein Eppendorf tubes pre-coated with Iodination Reagent and 37 to 74 MBq of sodium iodine (1 to 2 μl, $Na^{131}I$, 0.1 M NaOH), for 10 minutes under shaking conditions (Figure 4.4). The advantage of using pre-coated tubes is that the reaction is stopped by just transferring the solution to a different (non-coated) vial. Hence, after reaction, the crude was transferred to a different vial and the protein fraction was purified with 3 kDa centrifuge filters. The contents of the filter were recovered with simulated body fluid (SBF).

The radiochemical purity of the labelled proteins was assessed by instant thin layer chromatography (iTLC). With that aim, a diluted sample of labelled protein (0.2 μl) was mixed with sodium thiosulfate (1 μL, 100 mM) as reducing agent and

seeded on a paper iTLC strip. The strip was eluted with methanol/H_2O 85:15, and finally measured with a radio thin-layer scanner. Under these conditions, labelled proteins stay at the seeding spot, while unreacted iodine is eluted with the solvent.

Results confirmed radiochemical purity above 95 % before purification with centrifugal filtration, and this value raised to 99 % after purification. The labelled proteins were used to spike solutions with pre-known concentrations of proteins, to have full control on specific activity of the final preparations.

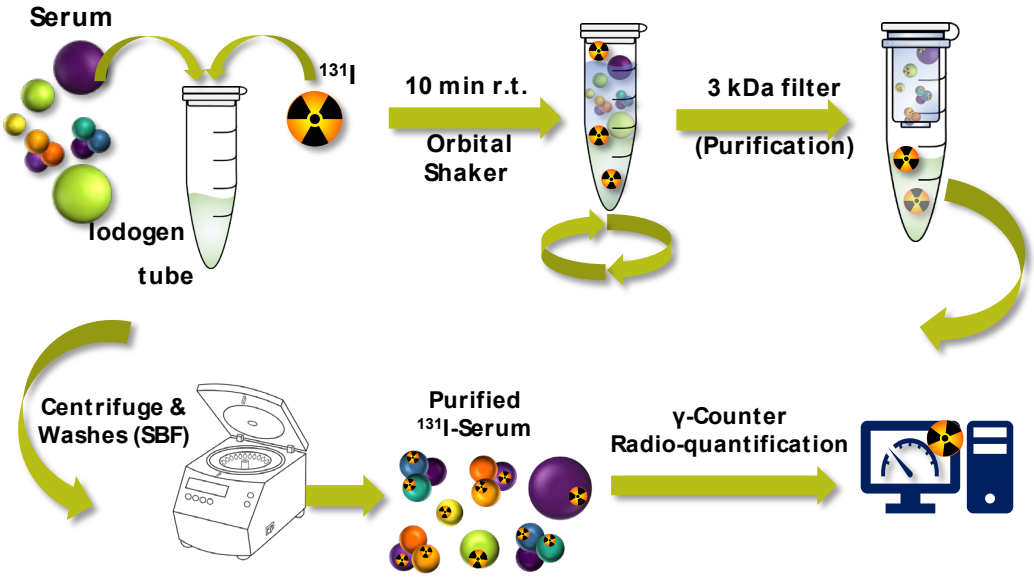

Figure 4.4. Scheme of serum radiolabelling process, purification, and quantitative measurements of radioactivivity performed with a gamma counter.

When the radiolabelling is carried out in serum samples, different proteins can be labelled, not only BSA. Of note, not all proteins will necessarily react at the same rate with ^{131}I, as the reaction rate depends on the number of tyrosine residues and their exposure to the media. To characterise the labelled mixture of proteins, electrophoresis techniques were used. The analysis of the different labelled species was achieved in a 15 % polyacrylamide gel electrophoresis gel (SDS-PAGE) run under 150 V for 40 minutes. The gel was stained with

Coomassie blue, and each line was cut and placed onto a radio-TLC plate reader to determine the chromatographic profile. Correlation between the distribution of species stained with Coomassie blue and the chromatographic (radioactive) profile obtained after scanning the plate with the TLC-reader were observed, suggesting that the amount of radiolabelled protein matches the amount of non-labelled protein present in the solution. In other words, the radiolabelled proteins faithfully represent the protein distribution in the serum.

Finally, and to enable the absolute quantification of the amount of radiolabelling protein in subsequent experiments (see below) a calibration curve was generated. With that aim, different solutions containing increasing (and known) amounts of radioactivity (^{131}I; range: 22 Bq to 55 kBq; 0.6 nCi to 1.5 μCi) were prepared and measured in an automated gamma counter (Perkin Elmer 2470 Wizard 2). The values in counts per minute (CPM) and real amount of radioactivity (Bq) were correlated with the Equation 8.

Equation 8 $$Y(Bq) = 11.34\,x(CPM) + 274;\ (r^2 = 0.9999)$$

4.2.3. Stability of albumin used as stabilizer in PLGA-BSA NPs

PLGA NPs stabilized with BSA were prepared as described in Chapter 3. In this case, BSA acts as a surfactant and remains attached to the PLGA core by weak hydrophobic interactions. The BSA coating can thus be considered in this case a special case of protein corona, though it is not formed by exposing the NPs to a biological fluid. To evaluate the stability of BSA used as stabilizer in different conditions, the albumin present on the surface of the NPs was radiolabelled with ^{131}I using a similar approach to that described in the previous section (see Figure 4.5 for schematic representation of the labelling procedure). In brief, an aliquot containing 600 μg of PLGA-BSA NPs in 300 μl of SBF (2 mg mL^{-1} on PBS) were incubated for 45 minutes at 37 °C on an orbital shaker with 3.7 MBq of ^{131}I on

Iodination reagent coated tubes. The reaction mixture was then withdrawn, diluted with 600 µl of SBF, and subsequently centrifuged at 16 kRCF for 15 minutes and washed twice with SBF. After purification, the particles were incubated with SBF, BSA 2 % and purified serum on an orbital shaker up to 72 h.

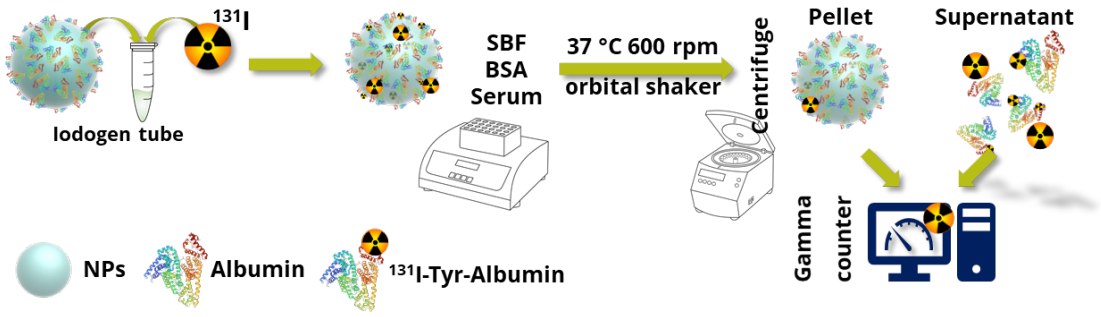

Figure 4.5. Scheme of radiolabelling of albumin presents on the surface of the surfactant of PLGA-BSA NPs.

At pre-selected time points, aliquots were obtained and centrifuged at 16 kRCF for 30 min to separate NPs. The amount of radioactivity in the filtrate, the washings and the filter were measured using a gamma counter, and the percentage of protein attached to the NP was calculated as the ratio between the amount of radioactivity in the filter and the sum of the amounts of radioactivity in all fractions.

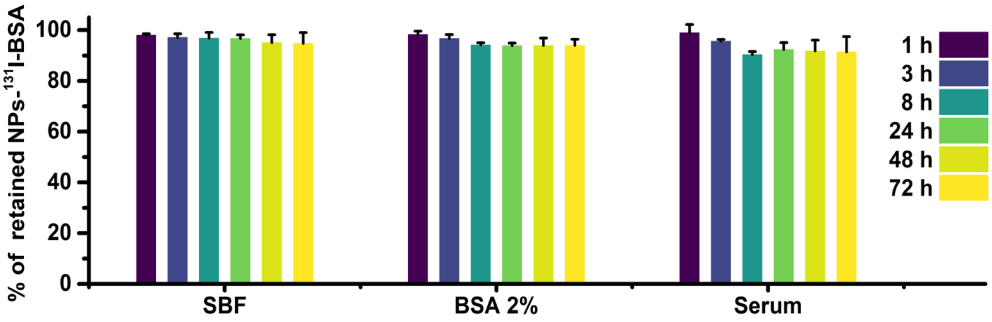

Figure 4.6. Stability of the ^{131}I of the labelled albumin on the surface of the PLGA-BSA NPs.

As it can be seen in Figure 4.6, the radioactivity remains almost quantitatively attached to the NPs up to 72 hours after the start of the incubation, irrespectively of the incubation media.

More precisely, up to the 94.7 % of labelled protein molecules remain attached to the NPs after 72 hours incubation in SBF. When the incubation media is an aqueous solution of albumin (20 mg mL^{-1}) this value is slightly decreased to 93.9 %. Interestingly, serum seems to be the medium that favours to a higher degree the detachment of the labelled proteins from the NP. In this medium, the percentage of labelled protein that detaches from the NPs is close to 8 % at t = 8 hours of incubation, although this value remains constant over the whole incubation period up to 72 hours. The differences discussed above were found to be non-significant. The high stability of the labelled particles confirms that protein release/exchange with the media is very slow in all cases, almost negligible. These results are positive. Indeed, the stability of BSA as stabilizer of PLGA NPs confirms that these particles are suitable to investigate the formation of PC, and that the risk of detachment of the stabilizer can be neglected.

4.2.4. Protein corona preparation in BSA- and PEI-stabilised PLGA NPs

For biomedical applications nanomaterials are usually functionalized with molecules to avoid unspecific interactions with biological molecules. The most common strategy is based on the use of dense coatings of hydrophilic polyethylene glycol (PEG) molecules.[19] However, in the last decade it was found that the PEG protective shell generates antibodies against these molecules, avoiding consecutives treatments.[197–199]

In this thesis, and to investigate the dynamics of PC, two different NPs were assayed: BSA-stabilised PLGA NPs and PEI-stabilised PLGA NPs, 150 nm sized,

and prepared as described in Chapter 3. These particles were incubated with a solution of labelled proteins: albumin or serum.

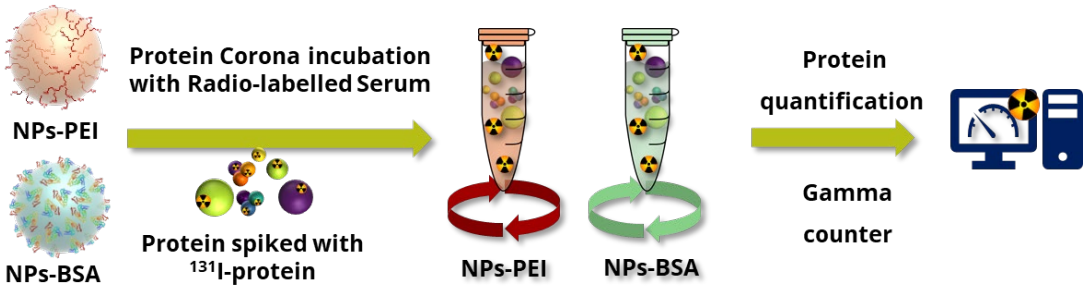

Figure 4.7. Schematic representation of the procedure followed for the investigation of PC dynamics in BSA- and PEI-stabilised PLGA NPs after incubation in media containing labelled albumin or labelled serum proteins.

To prepare the labelled protein solutions, the stocks were spiked with radiolabelled purified proteins labelled as described in Section 4.2.2. The particles (100 μg) were incubated with the labelled medium (100 μL) (Figure 4.7). After incubation for 1 hour (37 °C under orbital shaking) the particles were centrifuged at 16 kRCF for 20 min. The centrifugation and separation of the pellet leads to very small loss of the protein from the corona, and the obtained results reflect the protein content in the corona formed around the NPs.[36]

The supernatant was collected, and each fraction was measured in an automatic gamma counter. The pellet was further resuspended in SBF (100 μL) and three additional centrifugation/washing steps (100 μl of SBF each) were applied. At each step, the amount of radioactivity in the pellet and the supernatant/washings was measured. The fraction of radioactivity in the NP (remaining in the precipitate) after the first centrifugation step was the complete or soft corona (SC). The fraction of radioactivity after the three washing steps was considered to be the hard corona (HC), which is formed by a monolayer (2 - 7 nm thickness) of proteins strongly adhered to the surface of the particles, with a high constant affinity and a high synergic interaction with the particle surface. The

values obtained were used to determine the amount of protein in both the soft and hard coronas, based on the specific radioactivity of the proteins in the incubation media (Figure 4.8).

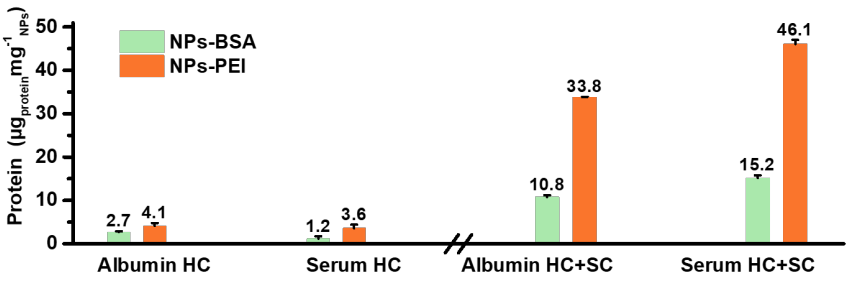

Figure 4.8. Amount of protein associated to NPS after incubation in solutions containing labelled BSA or labelled serum.

In general terms, larger protein corona is formed around PEI stabilized PLGA NPs (both HC and SC) in serum and albumin. Absolute values (μg of protein per mg of NP) almost triplicate values obtained for BSA-stabilised NPs. Additionally, it is clear from the results that the amount of protein integrating the soft corona is much higher that the amount of protein present in the HC. The positive charges on the surface of the NPs due to the presence of PEI strongly interact with the albumin, displaying negative charges at physiological pH.

The interaction of proteins from blood with nanoparticles will depend on protein concentration and affinity for the surface chemistry of the NPs. Protein corona starts forming with the most abundant protein in blood and usually low surface affinity (albumin) and it is followed by an exchange of proteins with higher affinity. However, there are proteins with very low affinity for the surface of a nanomaterial that can be present in the corona through interaction with other proteins, and other proteins like the complement protein C3b that can covalently bond to the surface of the particle (Figure 4.2).

4.2.5. The effect of albumin and serum of a former Protein Corona

For both hard corona (HC) and soft corona (SC) formed onto NPs stabilized with PEI and albumin, the stability of the proteins around the NPs was assessed by incubating the NPs in simulated body fluid (SBF), unlabelled albumin, and serum at different time points. Then, NPs were separated from the media and the amount of radioactivity retained in the NP was measured. The percentage of protein released from the NP was determined as the ratio between the amount of radioactivity found in the media after incubation and the total amount of radioactivity, expressed in percentage.

During development of the experimental set up, various strategies were attempted, such as separation through porous membranes (Transwell® plates of different pore sizes), separation by filtration using chromatographic columns, centrifuge filters or HPLC. However, the methods tested produced a destabilization of the protein corona or were governed by diffusion phenomena that prevented the correct quantification of the protein-associated the particles. Just to mention one example, 5 to 20 % of the protein content is absorbed in the surfaces of centrifuge tubes; the diffusion across membranes takes hours to reach the equilibrium across the pore of the membranes, and the chromatographic separation by column separation and HPLC alter the partial composition of corona, or proteins stack at the entrance of the column. Therefore, as mentioned in Section 4.2.4 the centrifugation was the method used for isolation of the NPs.

The evaluation of the stability of the different protein coronas was performed as follows: aliquots of NPs (1 mg mL^{-1}) with the preformed protein corona were placed in low binding protein tubes with the incubation solution (SBF, albumin or serum). The incubation was performed under orbital shaking at 37 °C and 600 rpm. At selected time points (0.2, 0.5, 1, 2, 4, 8 and 16 hours) an aliquot was

extracted and centrifuged at 16 kRCF for a period of 10 to 30 minutes. The pellet containing the NPs and the supernatant were separated and the amount of radioactivity in each fraction was determined using an automatic gamma counter. The percentage of PC remaining on the NP was calculated as the ratio between the radioactivity in the particles (measured in the pellet) and the total radioactivity (pellet and supernatant).

The exchange of proteins is understood as a competitive displacement of the previously adsorbed proteins by new proteins with higher affinity to the surface (Vroman effect).[200] The postulated mechanism was based on a three step sequence of desorption and adsorption of proteins, followed by a competitive exchange that progressively exchange the previously bounded proteins for new ones *via* a transient complex formation, exposing the protein from the inner layer and desorbing the protein placed into the inner layer.[201]

A. Stability of Serum Corona on PLGA-PEI NPs

Incubation of the NPs with a serum HC (3.6 ± 0.8 μg $_{\text{serum HC}}$ per mg $_{\text{PLGA-PEI}}$) in SBF resulted in a release of radioactivity as low as 3.2 % (0.11 ± 0.01 μg $_{\text{protein}}$ per mg $_{\text{PLGA-PEI}}$) suggesting that the HC is stable in this medium (see Figure 4.9). This means that 97.0 % of the original protein (3.50 ± 0.05 μg $_{\text{protein HC}}$ per mg $_{\text{PLGA-PEI}}$) remains at the NP surface after incubation. This stability was observed over 16 h of incubation at 37 °C. However, when the particles were incubated in an aqueous albumin solution (20 mg mL^{-1}) after 16 hours, 10.4 % of the HC fraction (0.37 ± 0.01 μg $_{\text{protein}}$ per mg $_{\text{PLGA-PEI}}$) was detached from the surface of the NPs. Finally, the incubation of the NPs over 16 hours with non-labelled serum resulted in an exchange of 16.5 % (0.60 ± 0.02 μg $_{\text{protein}}$ per mg $_{\text{PLGA-PEI}}$) of the protein present in the hard corona.

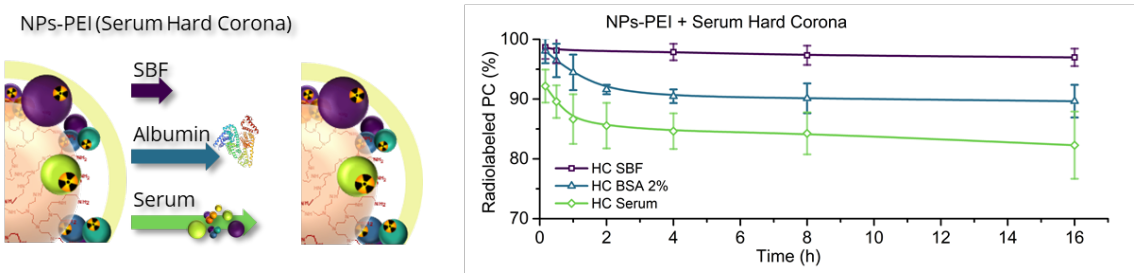

Figure 4.9. Scheme of PLGA-PEI NPs with the radiolabelled serum HC incubated in SBF, non-labelled albumin and serum (*left*); and graphic with the percentage of remaining protein corona on PLGA-PEI NPs after incubation (*right*).

The reason for these high values needs to be further explored, although we hypothesise that the presence of proteins in the serum with high affinity for the NP surface could contribute to a progressive displacement of the HC.[202] In all cases, it is noteworthy that the displacement of the proteins forming the HC occurs majorly during the first two hours of incubation.

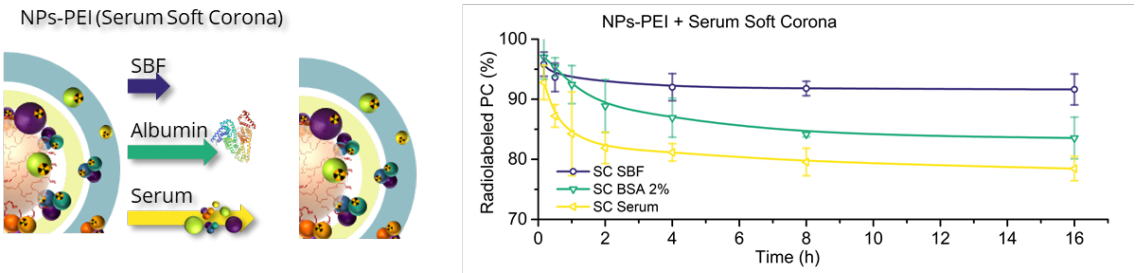

Figure 4.10. Scheme of PLGA-PEI NPs with the radiolabelled serum SC incubated in SBF, non-labelled albumin and serum (*left*); and graphic with the percentage of remaining protein corona on PLGA-PEI NPs after incubation (*right*).

When the NPs with the complete serum corona (HC and SC, 46.1 ± 0.9 μg $_{\text{serum SC}}$ per mg $_{\text{PLGA-PEI}}$) were exposed to SBF, non-labelled albumin or fresh serum, similar release profiles were observed (see Figure 4.10). The incubation with SBF reveals a release of 6.4 % of the serum corona proteins (2.94 ± 0.01 μg $_{\text{protein}}$ per mg $_{\text{PLGA-PEI}}$) to the medium during the first hour, an after 16 hours, the amount of remaining protein was 42.2 μg $_{\text{protein}}$ per mg $_{\text{PLGA-PEI}}$ (91.6 %). When particles were exposed to serum, up to 21.5 % of the proteins (9.93

μg $_{protein}$ per mg $_{PLGA-PEI}$) were removed (Figure 4.10), with a faster exchange in comparison to incubation in albumin, and a resulting final amount of protein in the corona of 36.2 μg $_{protein\ SC}$ per mg $_{PLGA-PEI}$.

B. Stability of Albumin Corona on PLGA-PEI NPs

NPs with an albumin HC (4.1 ± 0.7 μg $_{albumin\ HC}$ per mg $_{PLGA-PEI}$) were incubated with SBF. Incubation resulted in a release of radioactivity of the 4.0 % (1.2 ± 0.5 μg $_{albumin}$ per mg $_{PLGA-PEI}$) after 16 h of incubation, suggesting a stable HC in this medium (see Figure 4.11). This mean that 96.0 % of the albumin corona remains at the surface after incubation. However, when the particles were incubated in an aqueous albumin solution (20 mg mL^{-1}) for 16 hours, only 7.3 % of the HC fraction (0.3 ± 0.1 μg $_{albumin}$ per mg $_{PLGA-PEI}$) was released from the surface of the NPs. The NPs incubated with non-labelled serum result in a release of 0.73 ± 0.08 μg $_{albumin}$ per mg $_{PLGA-PEI}$, which corresponds to the 17.8 % after 16 hours of incubation.

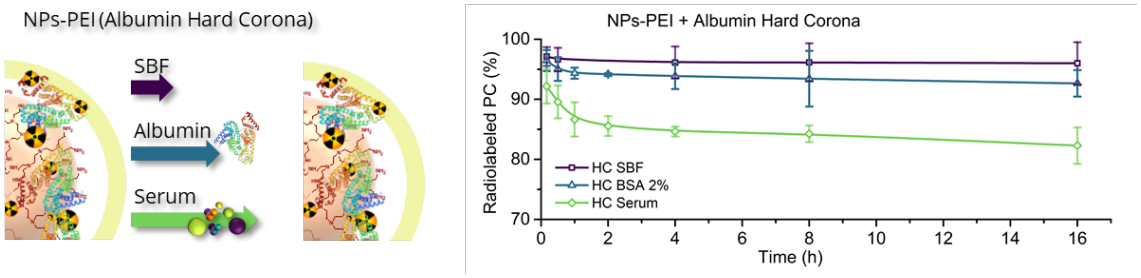

Figure 4.11. Scheme of PLGA-PEI NPs with the radiolabelled albumin HC incubated in SBF, non-labelled albumin and serum (*left*); and graphic with the percentage of remaining protein corona on PLGA-PEI NPs after incubation (*right*).

The HC (albumin and serum) of PLGA-PEI NPs showed almost equal concentration of protein per gram of NPs; and both released less than 10 % of the corona during the first two hours of incubation, when were incubated with SBF

or albumin on a progressive slow exchange. The exchange rate increases when the protein in serums with higher affinity can displace the former corona with fresh proteins. The albumin HC is likely to have a strong electrostatic interaction with the branched amine polymer at the surface, forming an albumin shell, with a low release profile.[203]

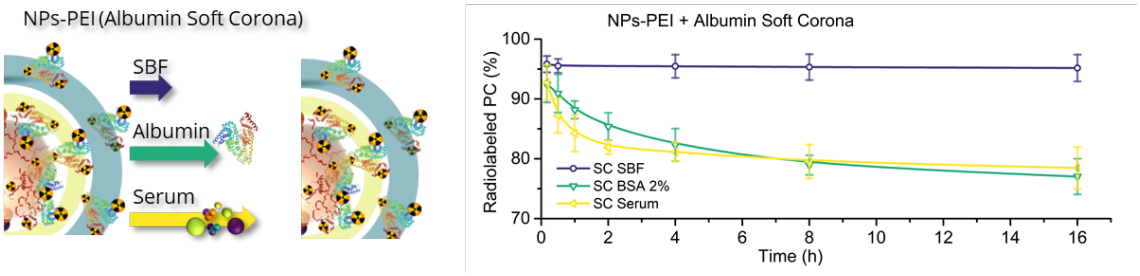

Figure 4.12. Scheme of PLGA PEI NPs with the radiolabelled albumin SC incubated in SBF, non-labelled albumin and serum *(left)*; and graphic with the percentage of remaining protein corona on PLGA PEI NPs after incubation (*right*).

As can be seen in Figure 4.12, the PLGA-PEI NPs with albumin corona (HC and SC, 33.8 ± 0.1 μg $_{albumin\ SC}$ per mg $_{PLGA\text{-}PEI}$) were stable in SBF releasing only the 4.8 % of albumin SC (1.6 ± 0.2 μg$_{albumin}$ per mg $_{PLGA\text{-}PEI}$) after 16 hours of incubation. While in presence of non-labelled albumin the exchange increase to 23 % that corresponds to 7.8 μg $_{albumin}$ per mg $_{PLGA\text{-}PEI}$; and in the presence of serum the amount of protein released is 21.5 %, that corresponds to 7.3 μg $_{albumin}$ per mg $_{PLGA\text{-}PEI}$ for the same period. These results suggest that SBF does not affect the preformed protein corona, and an equilibrium is achieved when just a small fraction of the corona is released. The albumin hard corona is not affected by the presence of albumin or serum, due to the adhesion of more albumin over the surface, which acts as stabilizer and cannot undergo exchange with the albumin shell created with albumin over the PEI surface.

The PLGA-PEI NPs with albumin SC incubated in serum showed the fastest and largest exchange of proteins.

C. Stability of Serum Corona on PLGA-BSA NPs

When PLGA-BSA NPs with serum HC (1.2 ± 0.5 μg $_{\text{serum SC}}$ per mg $_{\text{PLGA-BSA}}$) were incubated in SBF for 16 hours only 9.8 % of the serum HC was released (0.1 ± 0.2 μg $_{\text{protein}}$ per mg $_{\text{PLGA-BSA}}$). After 16 hours incubation with non-labelled albumin or serum, up to 45 % (0.7 ± 0.2 μg $_{\text{serum SC}}$) and 62 % (0.5 ± 0.2 μg $_{\text{serum SC}}$) of the preformed HC was removed.

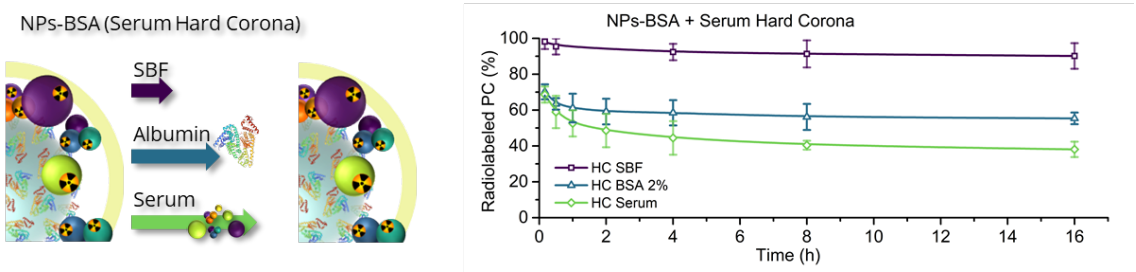

Figure 4.13. Scheme of PLGA-BSA NPs with the radiolabelled HC from serum incubated in SBF, non-labelled albumin and serum (*left*); and graphic with the percentage of remaining protein corona on NPs-BS PLGA-BSA NPs after incubation (*right*).

We hypothesize that the abundant exchange of serum HC with fresh proteins (albumin and serum) indicates that the coating of PLGA-BSA NPs reduce drastically the amount of HC proteins and increase the exchange of protein on the surface the NPs. The coating of PLGA-BSA was note detached from the NPs after incubation with proteins (see Section 4.2.3), indicating that albumin can act as stealth coating agent.

Furthermore, the serum corona concentration of the of PLGA-BSA NPs was three times fold less proteins than the PLGA-PEI NPs. This result suggests that the albumin used as surfactant reduces tight interactions of proteins to the surface of PLGA-BSA NPs, preventing hard corona formation, as we expected.

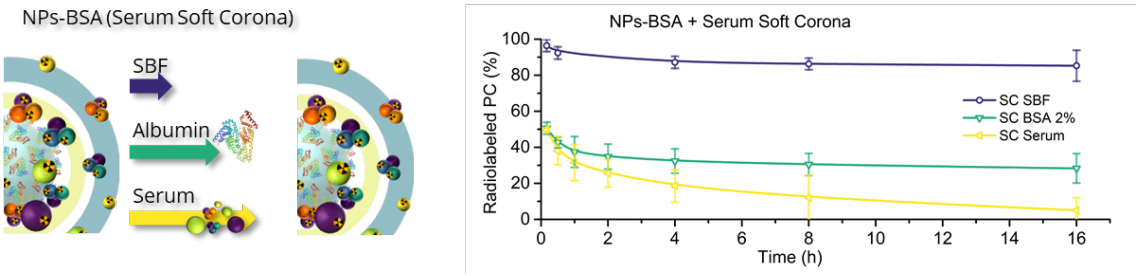

Figure 4.14. Scheme of PLGA-BSA NPs with the radiolabelled serum SC incubated in SBF, non-labelled albumin and serum (*left*); and graphic with the percentage of remaining protein corona on PLGA-BSA NPs after incubation (*right*).

The incubation of the PLGA-BSA NPs with serum SC (15.2 ± 0.6 μg $_{\text{serum SC}}$ per mg $_{\text{PLGA-BSA}}$) in SBF resulted in a release of 14.7 % (2.24 ± 0.02 μg $_{\text{protein}}$ per mg $_{\text{PLGA-BSA}}$) suggesting that the SC remains stable in this medium (see Figure 4.14). This means that 85.3 % of the original protein (12.9 ± 0.5 μg $_{\text{protein SC}}$ per mg $_{\text{PLGA-BSA}}$) remains at the NP surface after 16 hours of incubation in SBF.

Conversely, when the particles were incubated with non-labelled albumin or serum, a massive release of the serum SC (65 % and 74 %) occurs within the first two hours of incubation. After 16 hours of incubation with non-labelled albumin, the exchange continues removing up to 72 % of the serum SC. This means that only the 28 % of the original serum SC (4.3 ± 0.4 μg $_{\text{protein SC}}$ per mg $_{\text{PLGA-BSA}}$) remains after 16 hours. By other hand, the exchange produced by the non-labelled serum continues for 16 hours, removing the 95% of the initial serum SC. This means that only 5 % of the original serum SC (0.76 μg $_{\text{serum SC}}$ per mg $_{\text{PLGA-BSA}}$) remains. The remaining amount of protein is practically equal than the observed for the serum HC under the same condition.

D. Stability of Albumin Corona on PLGA-BSA NPs

The amount of albumin tightly bond (hard corona) to PLGA-BSA NPs was 2.7 ± 0.2 μg $_{\text{albumin}}$ per mg $_{\text{NPs-BSA}}$. As it can be seen in Figure 4.15, when the albumin

HC was exposed to SBF it remained stable. After 16 hours of incubation, as much as 89 % of the initial amount of albumin (2.4 ± 0.2 μg $_{albumin\ HC}$ per mg $_{NPs\text{-}BSA}$) was still attached to the NPs. And when albumin HC was exposed to albumin, 64 % of the initial corona (corresponding to 1.7 ± 0.2 μg $_{albumin\ HC}$ per mg $_{NPs\text{-}BSA}$) remained attached. This value decreased to 30 % when NPs were incubated in serum (0.9 ± 0.2 μg $_{albumin\ HC}$ per mg $_{NPs\text{-}BSA}$).

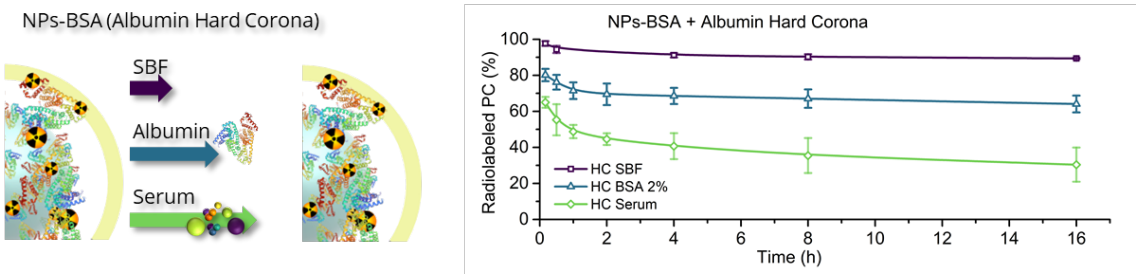

Figure 4.15. Scheme of NPs-BSA with the radiolabelled albumin HC incubated in SBF, non-labelled albumin and serum (*left*); and graphic with the percentage of remaining protein corona on NPs-BSA after incubation (*right*).

For the albumin SC (10.8 ± 0.4 μg $_{albumin\ SC}$ per mg $_{NPs\text{-}BSA}$) 89 % of the albumin remains attached to the NP up to 16 hours when incubated in SBF (9.6 ± 0.4 μg $_{albumin\ SC}$ per mg $_{NPs\text{-}BSA}$). When the albumin SC was exposed to albumin and serum, the most significant removal of proteins took place mostly during the first hour. In BSA, after 16 hour of incubation 95 % of the albumin corona was removed, (only the 0.5 ± 0.1 μg $_{albumin\ HC}$ per mg $_{NPs\text{-}BSA}$ was left at that time; Figure 4.16). When the NPs were incubated with serum, the amount of albumin removed was smaller (81.8% at t = 16 hours; amount left: 2.0 ± 0.2 μg $_{albumin\ HC}$ per mg $_{NPs\text{-}BSA}$) probably due the stabilization of the corona with other proteins with higher affinities.

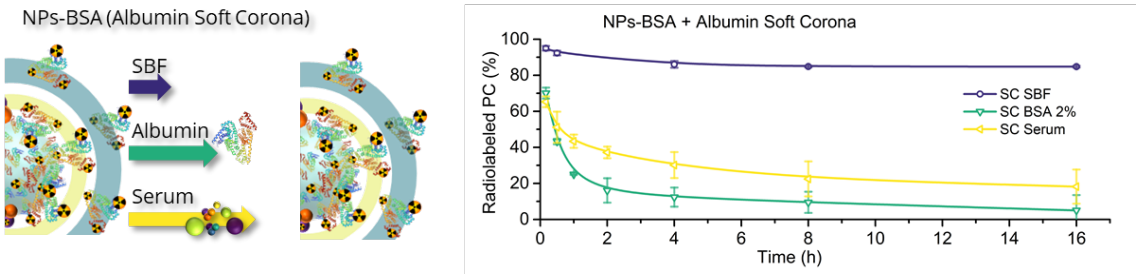

Figure 4.16. Scheme of PLGA NPs-BSA with the radiolabelled albumin soft corona incubated in SBF, non-labelled albumin and serum (*left*); and graphic with the percentage of remaining protein corona on NPs-BSA after incubation (*right*).

4.2.6. Blood pool serum radiolabelling for *in vivo* protein corona evaluation

The investigation of the stability of the protein corona in vivo is extremely challenging. Here, we assayed an indirect approach based on the intravenous administration of labelled proteins, followed (or not) by the administration of NPs. In both cases, the biodistribution of the labelled species was monitored using positron emission tomography (PET). Differences between biodistribution profiles obtained in both scenarios may provide information about the formation of the protein corona in vivo. For these studies, we decided to label the proteins using an ^{18}F-labelled prosthetic group, bearing an activated ester capable to react with primary amines present in lysine residues of proteins. This prosthetic group has proven efficient for the radiolabelling of NPs and nanomotors,[204,205] and its preparation is well established at the Radiochemistry and Nuclear Imaging Lab (see Section 5.2.5 for detailed labelling procedure). In brief, 50 µL of purified serum from rat blood were incubated with 6-[^{18}F]Fluoronicotinic Acid 2,3,5,6-tetrafluorophenyl ester (107.4 MBq) for 30 minutes at room temperature and under stirring. Acetonitrile (20 µL) was used as the solvent and the reaction was conducted in a low protein binding tube. After incubation, the serum was transferred to a centrifuge filter with a 10 kDa molecular cut-off. After one hour

of purification, the labelled proteins were recovered from the filter and submitted to quality control using radio-TLC. Results confirmed radiochemical purity values above 98 % in all cases, and the RCY (decay corrected) = 65 % respect to the incubated prosthetic group.

PET studies were carried out in two-months aged Sprague Dawley rats. Anaesthesia was induced with 5 % isoflurane in pure oxygen, and one of the lateral tail veins was canulated. Immediately after, the anesthetized rodent was placed in the homeothermic bed of the PET-CT camera with a face cone mask, where anaesthesia was maintained with 1 to 3 % isoflurane in pure oxygen. 300 µL of serum spiked with 18-30 MBq of radiolabelled serum were intravenously injected thought the canula, and PET images were obtained over a period of 5 hours.

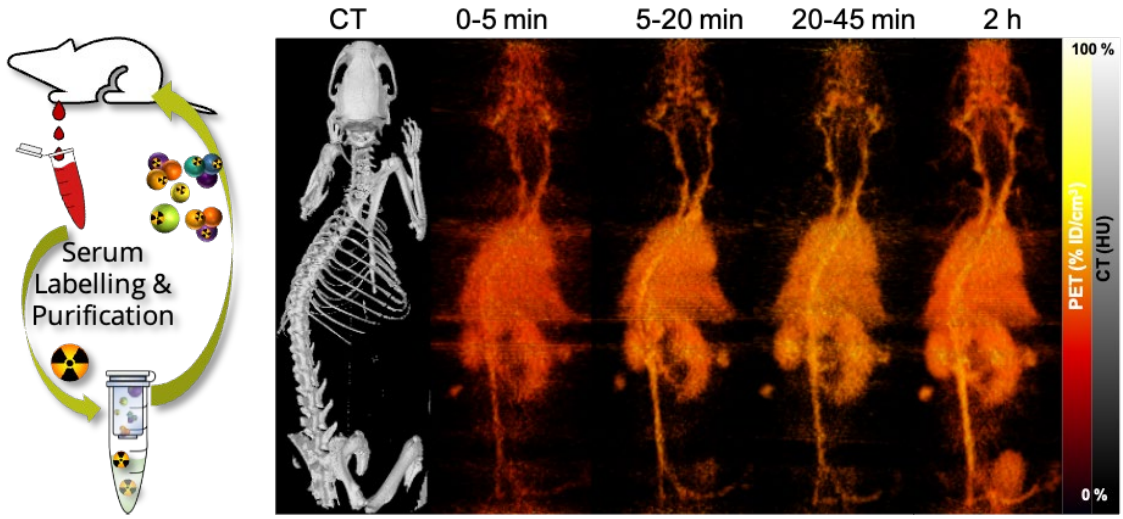

Figure 4.17. Surface CT and volume PET rendered whole body coronal images of average frame images of 0-5, 5-20, 20-45 minutes and 2 h before injection of ^{18}F radiolabelled serum with prosthetic group.

Images clearly show the presence of radioactivity in all major organs, including lungs, liver, kidneys, heart, and brain, suggesting the presence of radioactivity in blood. Progressive elimination of the radioactivity via urine was observed at longer times after administration (Figure 4.17).

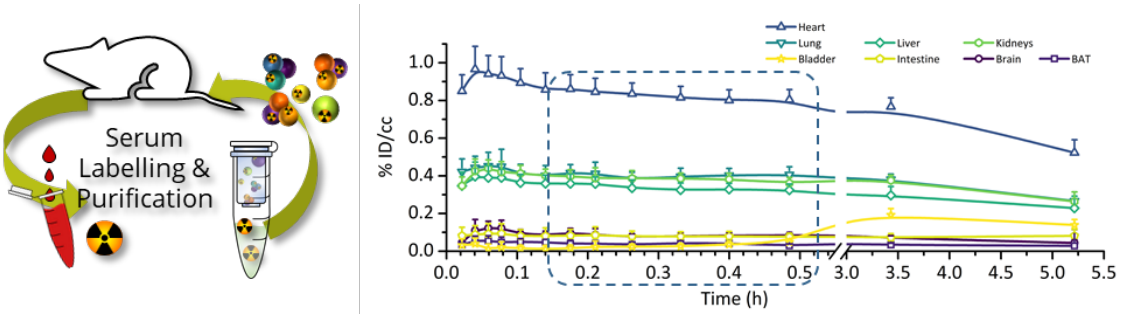

Figure 4.18. Concentration of radioactivity in the different organs expressed as percentage of injected dose per cubic centimetre, obtained from PET images after intravenous administration of serum labelled with ^{18}F-prosthetic group.

Quantification of the images was carried out by drawing volumes of interest in the different organs (Figure 4.18). Dynamic curves confirmed long circulation of the proteins in blood (as suggested by the high and slowly decreasing concentration of radioactivity in heart). The concentration of radioactivity was also significant in kidneys, liver, and lungs, where it remained stable over the duration of the study. Elimination via urine at t > 3 h was also observed.

Next, we repeated the study but 10 minutes after the administration of the radiolabelled serum, the animals were injected with 300 µL of the suspension of NPs at a concentration of 1 mg mL^{-1}, and PET-CT images were acquired.

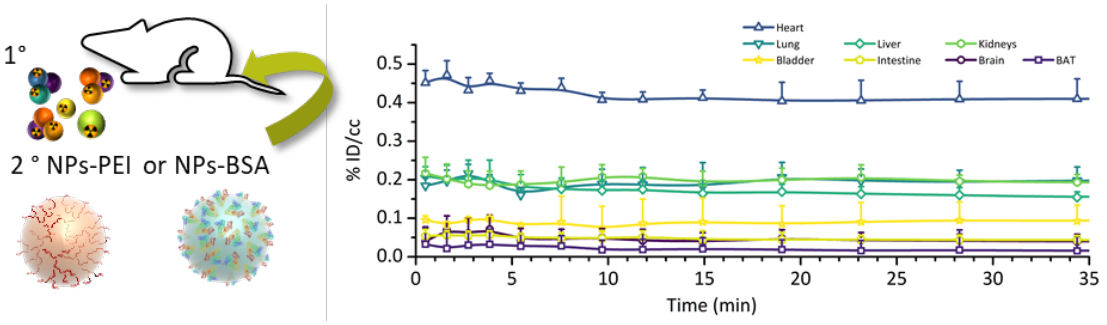

Figure 4.19. Concentration of radioactivity in the different organs expressed as percentage of injected dose per cubic centimetre, obtained from PET images after intravenous administration of labelled with ^{18}F-prosthetic group, ten minutes before NP administration.

As is can be seen in Figure 4.19 the variation in the concentration of radioactivity in the different organs after administration of nanoparticles did not

show a clear effect. During the firsts minutes an increase of the percentage of activity was noticed in the lungs, probably due the accumulation of aggregated nanoparticles, and a fluctuation in the heart was observed. It is also possible that the slight changes in the signal could be produced by distortion in the blood flow, as a result of the administered bolus containing the NPs.

4.3. Summary and Conclusions

In this chapter we have assessed the stability of hard and soft corona around PLGA NPs with two different surface coatings by means of gamma counting using radiolabelled proteins, albumin, or full plasma. PLGA NPs were prepared either with the positively charged polyethyleneimine (PEI) or with the slightly negatively charged albumin.

Since the albumin used as stabilizer for the NPs is only bound to the PLGA core by hydrophobic interactions it could also be replaced by proteins from the media. Therefore, we evaluated first the stability of the BSA surfactant. A straightforward iodination reaction in mild conditions was used to label the BSA on the NPs. Gama counting showed that albumin used as surfactant during the synthesis process of PLGA NPs is stable and remains associated to the NPs after exposure to SBF, non-labelled albumin and non-labelled plasma. It was also observed that the amount of proteins forming the soft corona on the PEI stabilized NPs was three times higher than on the BSA stabilized NPs, which is understandable since PEI is charged and proteins can strongly attach to the polymers due the electrostatic interactions.[203]

For both NPs, a soft corona is formed but the hard corona for BSA stabilized NPs is practically inexistent, proving that only weak interactions take place between the BSA used as surfactant and the protein of the media, while for the PEI NPs the electrostatic interactions are strong and lead to a large hard corona.

Exposing the NPs with a preformed corona to SFB always resulted in the loss of a relatively small percentage of proteins in comparison with the protein lost by exposure to non-labelled albumin and non-labelled serum. The non-labelled plasma resulted always in the largest removal of labelled proteins from the preformed corona. This can be understood as plasma contains other proteins than albumin with a higher affinity to the surface of the NPs, which can replace the albumin present in the preformed corona. Although experiments of protein exchange were performed with incubations up to 16 hours, major exchange occurred during the first hours of incubation. In the case of the soft corona on BSA coated NPs incubation with the plasma results in a practically complete removal of the corona.

The results presented in this chapter show the dynamic character of both soft and hard corona and how easily proteins can be exchanged in the corona. By means of gamma counting we have been capable of quantifying the mass of proteins associated with nanoparticles, with an accuracy that cannot be achieved by other techniques as the activity is directly proportional to the mass of radiolabelled proteins.

In addition, blood serum was labelled and injected into animals to determine if posterior administration of NPs results in al altered biodistribution pattern. Unfortunately, no conclusive results were obtained in these experiments.

5. *In vivo* fate of Mesoporous Silica NPs for targeted delivery

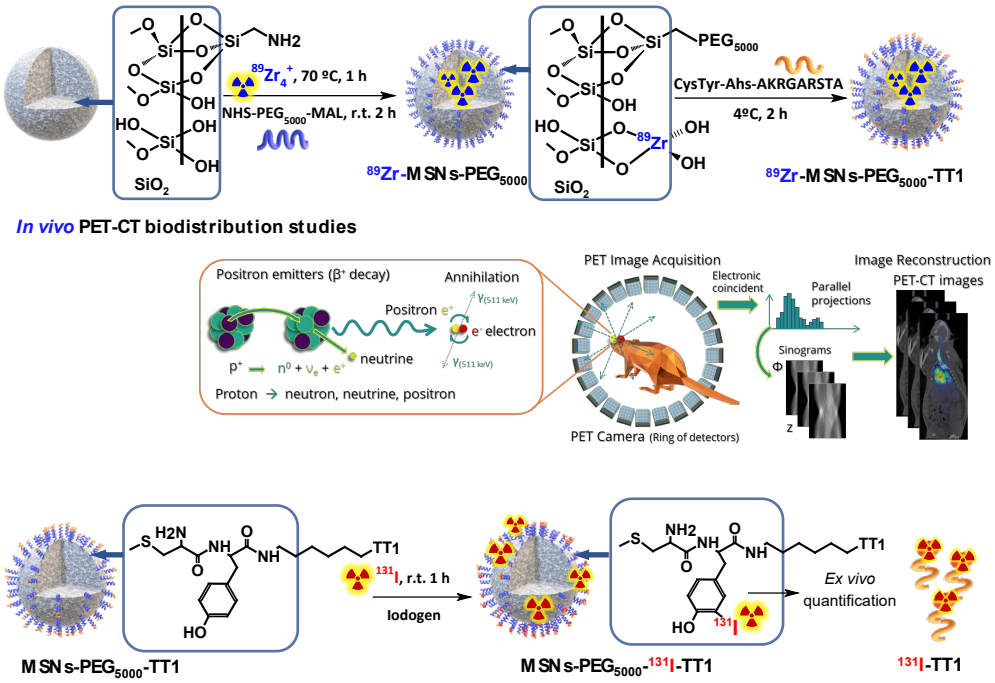

5.1. Introduction

Mobil Corporation researchers developed in 1992 a series of mesoporous materials, based on silica precursors and structure directing agents.[87] The acronym of MCM stands for Mobil Composition of Matter, and it refers to the mesoporous materials created by hydrothermal synthesis in the presence of a

structure director agent (SDA, organic amphiphilic molecule), that will form a structure on which it will condense the silica precursor, (usually tetraethyl orthosilicate TEOS or tetramethyl orthosilicate TMOS) that will form the inorganic part of the material by hydrolysis and polycondensation reactions. After the end of the reaction, the SDA is removed by extraction or calcination, obtaining the porous structure. The textural properties of the material consist of a narrow mesopore distribution in the range of 2 to 30 nm, and an elevated surface area up to 1500 $m^2\ g^{-1}$ at a pore volume *ca.* 1.3 $cm^3\ g^{-1}$.[206] In addition, the elevated density of silanol groups, present in the surface of the amorphous condensed silica, allows for easy and versatile chemical reactions.[207]

These structural characteristics allow these materials to be used in catalytic, separative or heavy metal adsorbent applications.[93,96] In the field of nanomedicine, they are of great interest for its application in the controlled administration of drugs, cell markers, gene transfection, immobilization of bioactive macromolecules or as sensors supporting interfaces.[7,208]

Due to the chemical resilience, versatile porous structure, temperature resistance and solvent stability of silica NMs, plenty of mechanisms and molecular gates have been engineered to control the release of the drug from the inside of the porous structures. The molecular gates are chemical structures placed at the end of the porous channels, the gatekeepers prevent the release of the drug inside the porous structure until a specific stimulus triggers a chemical or conformational reaction.[209] The drug can also be incorporated by surface covalently attached prodrugs that possess a reactive bond to a stimulus. The trigger to open the molecular gates can be internal (pH, salt, enzymes, and so on) and/or external stimuli (radiation, light, ultrasound, magnetic field, etc.).[210]

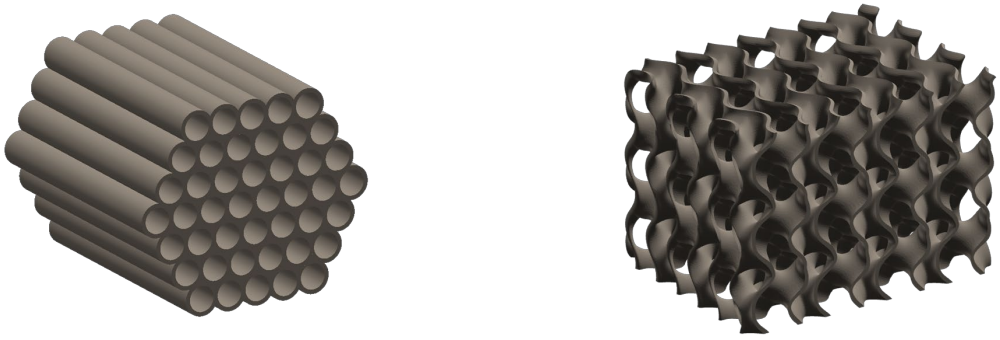

Figure 5.1. Illustrations of mesoporous structure of MCM-41 (*left*) and MCM-48 (*right*).

Two representative examples are the so-called MCM-41 and MCM-48 (Figure 5.1). These materials have pore diameters of 2 to 10 nm, modulable by adding swelling agents to obtain larger pore sizes. The pore wall is formed by a network of amorphous silica. The fundamental difference between the different MCMs lies in the ordering of its porous structure as shown in Figure 5.1. The materials MCM-41, MCM-48 and MCM-50 present hexagonal (space group P6mm), bicontinuous cubic (space group $Ia\bar{3}d$) and laminate phases (space group $p2$) respectively. Morphological control of these materials has been extensively studied and allows obtaining some of these materials in the form of nanoparticles. From a chemical point of view, the composition and structure of the inorganic matrix of mesoporous silica NPs (MSNs) is much more stable against organic solvents or enzymes than other "soft" systems, such as liposomes or polymeric NPs that are more susceptible to degradation by different routes. Nevertheless, the MSNs accumulate in the body and remain in the organs until the silica dissolves, and it is eliminated through the excretory system by the urine. Silica degradation takes place through the hydrolyzation of silanol groups exposed on the surface (indeed, ca. 35 % of silicon atoms are exposed in the mesoporous). However, proteins in bloodstream may stack on the surface of the particles reducing the exposed area, lengthening the designed drug release times, and diminishing eventual therapeutic effects.

Apart from the strategies based on the use of gates to prevent early and unspecific release of drugs, there is a need to selectively increase the uptake in specific tissue. There are two main strategies for increasing uptake of NPs in specific tissues, the direct targeting and the pre-targeting approach.[205,211,212] Both are based on the EPR effect where the bloodstream delivers nutrients through the intricate and defenestrated vasculature characteristic from the surrounding tumour tissues where NPs are can be accumulated.[18,135] The mesoporous NPs that flow through the vessels can pass the endothelium gaps and reach the tumour tissue, and at certain points the particle interacts with the membrane of the cell and the particle is introduced by the endocytic process and the cargo released.[213,214] The active targeting is based on the interaction between proteins or receptors overexpressed in cancer cell membranes with specific ligands, such as peptides or antigens, which are incorporated into NPs.[52] The pre-targeting approach is a two steps strategy based on the administration of a molecule with specific and elevated affinity with the cancer cell, that have been modified in the terminal part to interact with a particle with a specific moiety that is administered in a second step.[205,215]

5.2. Result and discussion

In this chapter we perform a complete study of mesoporous silica NPs with a homing peptide, assessing the biodistribution and degradation of the NPs and their components at *in vitro* and *in vivo* scales. The study encompasses the synthesis, functionalization, characterization, *in vitro* degradation ratio, *in vitro* cell uptake evaluation and *in vivo* biodistribution of MSNs in melanoma xenograft tumour mouse model.

5.2.1. Synthesis, functionalization and characterization of MSNs

The method for the preparation of MSNs is based on modifications to the method presented in 1968 by Stöber et al. to synthesize monodisperse solid silica particles. The particles are formed in an ethanolic aqueous mixture, by tetra alkyl silicates with a basic agent as catalyst. The reaction starts with the precipitation of silica nuclei (nucleation stage) followed by the gradual growth of hydrated silica groups (SiO_4^{4-}) on the surface (growth stage) until the reagents are consumed to the final size of the particles. The control of morphology and size of NPs are given by the amount of silica precursor added in the synthesis, and the electrostatic repulsions between particles, among other factors, which cause them to acquire spherical form to minimize their energy surface.

Modifications of the Stöber method consist in the use of SDA (amphiphilic polymers or surfactants) for the formation of liquid crystal phase (or mesophase), that acts as the template on which the polycondensation continues in a cooperative growth stage over the self-assemble SDA. The controlling factor of the sol-gel reaction as surface-silica, concentration of self-assemble surfactants, silica condensation rate, temperature, pH, solvent polarity, stirring speed, among others allow to obtain different morphological structures.

MSNs have been synthesized following a previously described method, with small modification to obtain porous silica NPs of 120 nm diameter.[90] Briefly, 0.50 g of Hexadecyltrimethylammonium bromide (CTAB, 1.4 mmol, 98 %, SA) and 2.05 g Pluronic F−127 (163 μmol, 98 %, SA) were dissolved in a solution containing 96 mL of MQ water, 43 mL of absolute ethanol (0.93 mol, 100 %, SA) and 11.2 mL NH_4OH (180 mmol, 29 %, SA) under magnetic stirring for 30 minutes until complete dissolution. Under magnetic agitation at 1000 rpm, 1.95 mL of tetraethyl orthosilicate (TEOS, 8.5 mmol, 98 %, 0.93 g mL^{-1}, SA), were

poured into the vortex of the previous solution. The stirring was maintained for 1 min to initiate the nucleation stage, and subsequently the mixture was kept for 24 hours at room temperature without stirring during the condensation stage.

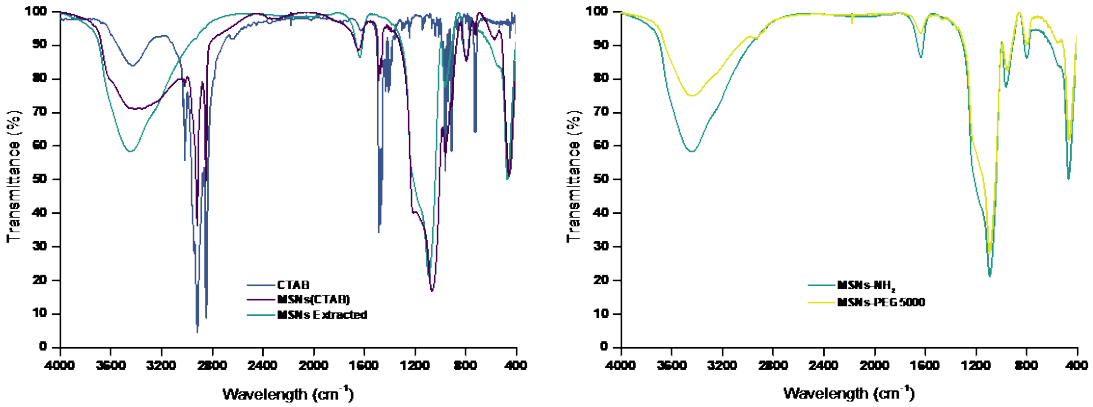

Figure 5.2. FT-IR spectra of MSNs before and after DSA (CTAB) extraction (*left*) and after PEG functionalization (*right*).

The MSNs, a white solid product, was collected by centrifugation at room temperature at 9 kRCF for 20 min, washed with 100 mL of MQ water three times and twice with 30 mL of ethanol (70 %, SA).

The SDA is a detergent agent that must be eliminated thoroughly to avoid toxic effects. The extraction was performed by acidic hydrolysis under reflux overnight in ethanolic acidic mixture (20 mL, 70 %; 4 mL HCl, c.c.), and washed with MQ water and ethanol 70 % twice, subsequently dried for storage and characterization. To confirm the total elimination of the agent FT-IR was performed to determine the presence of SDA (See Figure 5.2). The left part of the figure shows IR spectra for CTAB, and the particles before and after extraction. The absence of CTAB signals in MSNs (extracted) can be clearly visualised, based on the absence of the most intense signal of: C-H stretching vibrational features at 2800 to 2960 cm^{-1}, methylene scissoring vibration and asymmetric bending mode of the head methyl group at 1450 to 1500 cm^{-1}, the CH_2 wagging region at 1360 to 1440 cm^{-1} and C-N stretching vibrational modes at 900 to 980 cm^{-1}.

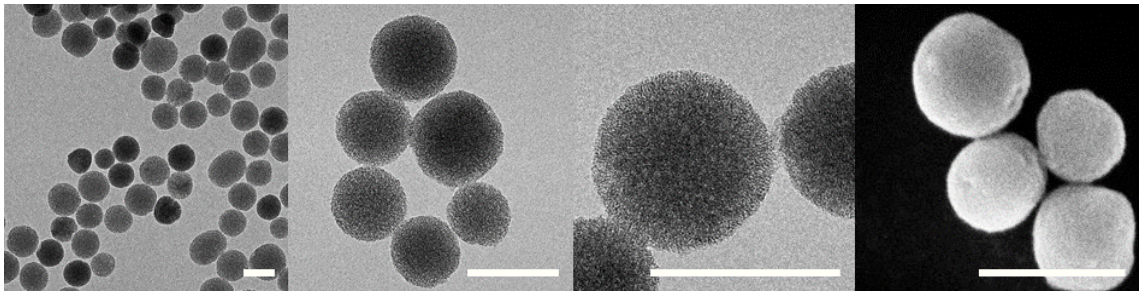

Figure 5.3. Electron microscopy images, transmission, and scanning mode of mesoporous silica MCM-48 nanoparticles. Scale bar of 200 nm.

However, after functionalization with amine and PEG, the only visible region is related to the C-H stretching vibrational features at 2800 to 2960 cm^{-1}, while the other characteristic regions of PEG molecules of C-O stretching at 1000 to 1100 cm^{-1} are masked under the characteristic silanol band of: bending modes of OH at 1650 cm^{-1}, the symmetric vibrational stretching Si-O-Si at 1000 to 1100 cm^{-1}, the stretching Si-OH at 960 cm^{-1} bands, and the asymmetric stretching vibrational mode at 800 cm^{-1}.

Particle visualization was performed by electron microscopy (Figure 5.3). Particles showed spherical shape with regular porous structure. Functionalization with amine groups was confirmed by ζ-potential shift from negative (-20 ± 4 mV) to positive (15 ± 2 mV) values.

N_2 adsorption-desorption isotherm curves are shown in Figure 5.4 (right). Both curves exhibited a type IV isotherm curve, that is characteristic of mesoporous materials. The hysteresis loop is produced on mesoporous materials with cavities interconnected through pore sizes due the multilayer adsorption followed by capillary condensation and shown at a relative pressure of $P/P_0 = 0.5$. The reduction of the loop height after the functionalization indicates a reduction of open pores. The average pore size distribution of 3 nm is maintained after functionalization, while the pore volume is slightly reduced. This is probably due to disappearance of external pores with larger diameter, due to the

functionalization with the amine silanol groups which is enhanced on the external surface of the particle, where the pore with bigger diameter is exposed.

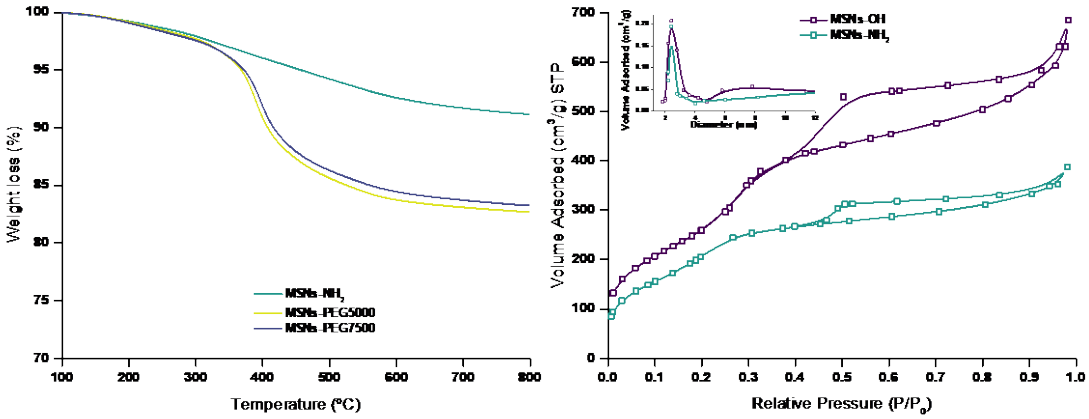

Figure 5.4. *Left*: Thermogravimetric analysis of non-PEGylated and PEGylated particles; *right:* Nitrogen adsorption and desorption curves and volume adsorption *vs* pore distribution (*inset*), to determine surface area in the mesoporous silica nanoparticles.

The post-graphing step was performed according to the literature,[216] taking the average of 4.9 silanol groups per nm^2 and 1057 ± 45 m^2 g^{-1} of MCM-48 NPs, which provides 8.6 mmol of silanol groups per gram of MCM-48. The silanol groups of the surface were aminated by condensation of silanol groups of aminated silanol compounds, as follows. Briefly, 100 mg of NPs were resuspended in 10 mL of absolute ethanol[217] in an ultrasonic water bath for 10 min. Meanwhile, 1.1 equivalent of the available functionalization groups, 0.6 µl of (3-aminopropyl) triethoxysilane (APTES, 0.32 mmol, 99 %, 0.946 g mL^{-1}, SA) were added to the suspension under magnetic stirring at room temperature. The reaction was kept for 4 hours and afterward, MSNs was collected by centrifugation and washed twice with ethanol 70 %.

Polyethylene glycol (PEG) functionalization on the MSNs is needed to enhance colloidal stability, reduce haemolysis, protein adhesion, and extend circulation.[218,219] PEG chains of two molecular weights (5000 and 7500 Da) were used in the experiments. The coupling of PEG chain was performed via Michael

addition of acrylate terminal groups with hydroxyl groups in the other extreme to avoid self-condensation. The percentage of potential external available groups to be functionalized is estimated as 25 % of the total surface area of 886 m^2 per gram of amine functionalized surface. Briefly, 10 mg of Silica MSNs were dispersed in 10 mL of PBS for 10 minutes in ultrasonic water bath. Then 2 eq. of PEG (2 x 61 μmol) were dissolved in 100 μl of PBS and poured to the suspension. The reaction was kept for 2 hours under magnetic stirring. Then, the NPs were washed three times with PBS and dispersed in a final volume between 1 to 10 mg mL^{-1}.

The B16F10 melanoma tumour cell presents increased levels of p32 protein in the membrane. To evaluate the action of short peptides as active targeting agents in silica NPs, LinTT1 peptides were anchored on the surface of the nanoparticle through the PEG chain. LinTT1 peptide sequence consists of a penetrating sequence followed by a short peptide of STA amino acids that specifically target the p32 protein membrane, overexpressed on cell membrane in melanoma cells.

The peptide sequence was designed to be anchored to the PEG via cysteine (AKRGARSTA). After the cysteine residue, a tyrosine amino acid was added to the sequence for further iodination with ^{131}I. Additionally, amino hexanoic acid (Ahs) units were included in the sequence as spacers, to obtain the final sequence: MSNs-PEG-CY(Ahs)AKRGARSTA.

As mentioned above, the particles were synthesized with two different PEG lengths (5000 and 7500 Da) corresponding to 110 and 170 oxyethylene (ethylene glycol) subunits. The thermogravimetric analysis of particles revealed a mass increase of 7.93 % and 8.48 % respectively after functionalization, meaning that each 100 g of MSNs have been covered by 1.586 and 1.13 mMol of PEG units.

According to the thermogravimetric analysis (see Figure 5.4, left) the NPs present a dense polymer brush of polyethylene glycol, with a ratio of one to ten peptides per polymer chain, and the estimated density was 1.5 and 0.7 PEG chains per square nanometre for PEG chains of 5000 and 7500 Da, respectively. Those values are in the limit of brush configuration. Polymers tethered on a surface can adopt two conformations: the mushroom or folded conformation occurs when the density is low, and polymer have a great degree of freedom to move. The brush conformation occurs when the density of polymers is high enough such the polymer is stretched out and extended without degree of freedom to move. The brush configuration avoid protein interaction and reduce opsonin mediated clearance of NPs.[143,220]

5.2.2. *In vitro* preliminary evaluation of Melanoma cell

The expression of p32 or gC1qR/C1QBP/HABP1 as a specific receptor for LinTT1 peptide was first evaluated in vitro.[221] The protein is overexpressed in the cell surface an inside the mitochondrial surface in certain cancer cells, and it is related with the oxidative phosphorylation metabolism, favouring the glycolysis instead of oxidative pathway even in aerobic condition (Warburg effect).

Confocal microscopy images (Figure 5.5) showed overexpressed p32 protein on the cell surface (in green; A images), and the capability of the free labelled (with a FAM fluorophore) peptide to reach the surface of the cell.

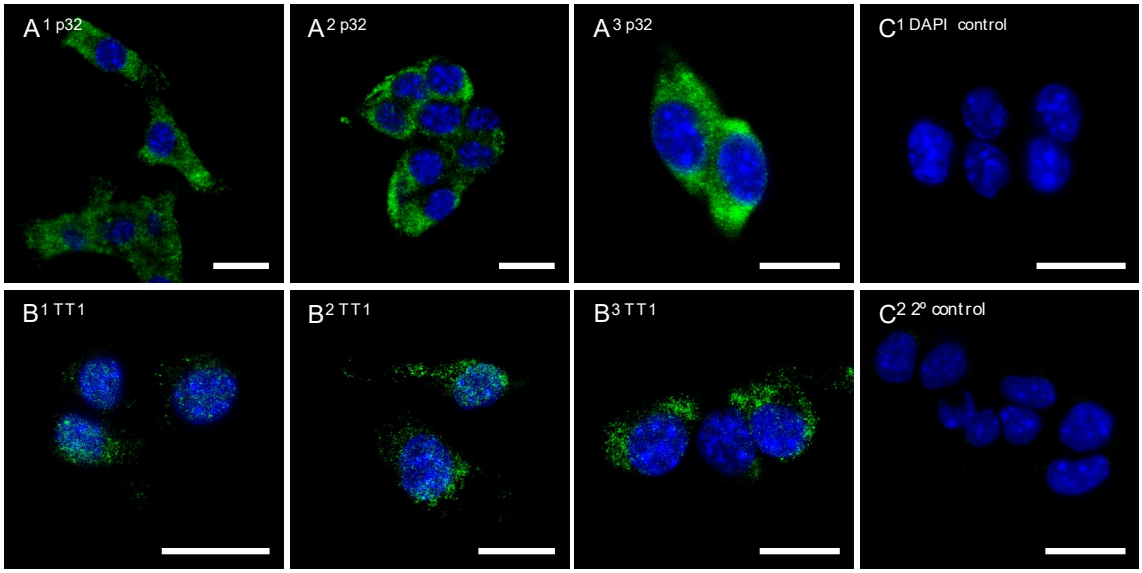

Figure 5.5. Confocal control images of melanoma cells, staining in green with *A*) p32 protein expressed in the membrane, *B*) free linear TT1 peptide labelled with FAM fluorophore and *C*) control of the secondary antibody; in blue channel the nucleus stained with DAPI. Scale bar of 20 µm.

After confirming the overexpression of p32 protein in the cell membrane, control experiments were carried to stablish the experimental set up for the evaluation of cell binding in the presence of NPs. With that aim, both NPs with and without the peptide were incubated for 10 min with the cells. NPs were synthetized with rhodamine in the porous structure to allow for proper visualization in subsequent microscopy evaluation.

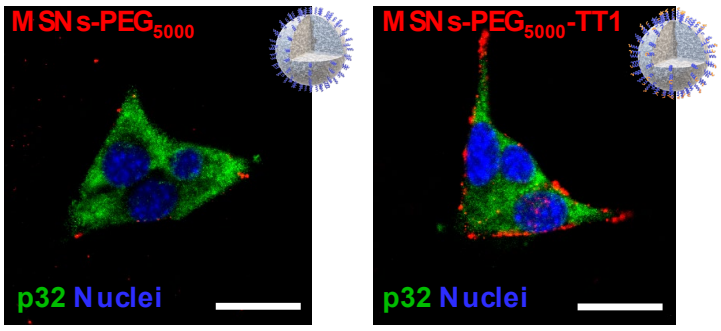

Figure 5.6. Confocal composition images of melanoma cells incubated with rhodamine labelled (*red*) MSN-PEG_{5000} and MSN-PEG_{5000}-TT1. P32 expression (*green*) Nuclei (*blue*). Scale bar 20 µm.

The images in Figure 5.6 shown in red the NPs (rhodamine), and in green the expression of p32 protein (Alexa 488). As can be seen in the right image the presence of Lin-TT1 in the NPs induces the attachment of the NPs to the cell, while the NPs without the peptide (left images) do not interact with the cell surface. These results confirm the active homing capacity of the peptide after attachment to MSNs.

5.2.3. Radiochemical incorporation and *in vitro* stability of ^{89}Zr in NPs core

After *in vitro* confirmation of selective attachment of NPs with TT1 to cells overexpressing p32 protein, we moved forward to the radiolabelling of silica NPs. Radiolabelling was assayed using two approaches: (i) labelling of the core of the mesoporous particles; and (ii) labelling of the targeting peptide

To label the core, we used the radiometal zirconium-89. Zirconium (IV) cation is an oxyphilic cation with large radii that forms stable complexes with oxygen ligands, being easily incorporated in the amorphous silica oxide mesoporous structure. Zirconium acts as hard Lewis's acid with the protonated silanol groups that act as hard donor groups. Hence, Zr can be incorporated into NPs without the need for a bifunctional chelator.[222] One approach for the incorporation of ^{89}Zr consists of mixing the oxalate salt with the silica precursor; in this case, the zirconium is widely diluted and stabilized with the SDA that is eliminated, resulting in incorporation yields below 1 %. By following this route, the zirconium is homogeneously distributed over all the structural amorphous silica, but the yield is too low to be applied to radiochemistry, particularly if *in vivo* studies need to be conducted. For that reason, the post synthetic route, based on incubation of already formed MSNs with ^{89}Zr, was assayed.

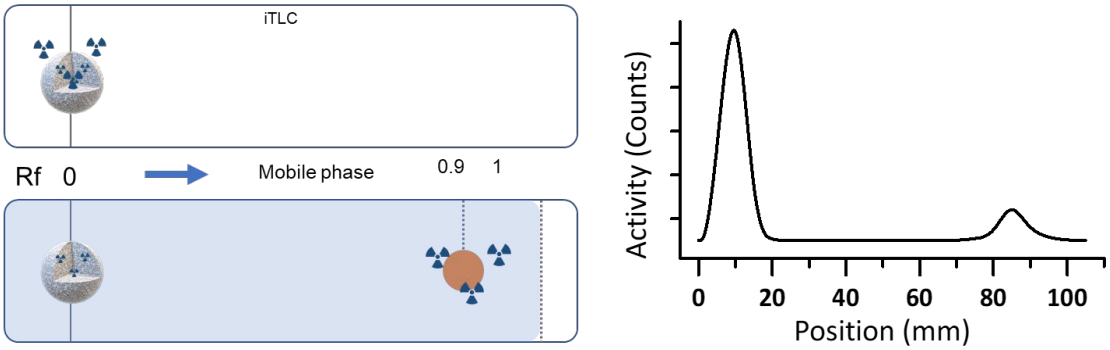

Figure 5.7. Scheme of radio-TLC measurements of ^{89}Zr-labelled MSNs. MSNs stay at the seeding spot, while ^{89}Zr migrates close to the solvent front.

While following the second synthetic route, the percentage of ^{89}Zr incorporated into the NP was monitored by radio-thin layer chromatography (radio-TLC). With that aim, aliquots (2 to 10 µl) were obtained during incubation and seeded on a silica-impregnated paper for chromatography (iTLC) and eluted (2:18 ACN:Citric Acid 20 mM, EDTA 60 mM at pH~5 as the mobile phase). Under these conditions, MSNs stay at the origin while ^{89}Zr is eluted almost with the solvent front (Rf = 0.9; see Figure 5.7), and the percentage of ^{89}Zr incorporated into the NPs can be directly calculated from chromatographic profiles.

To evaluate the effect of the presence of the PEG chain on the radiochemical yield of the reaction, ^{89}Zr incorporation was assayed both using bare and already PEGylated particles. The later was, a priori, perceived as more convenient, as labelling of bare particles would require the incorporation of the PEG functionalization after radiolabelling. Experimentally, bare and PEGylated particles were incubated for different times (from 20 to 90 min) and temperatures (from 25 to 90 °C).

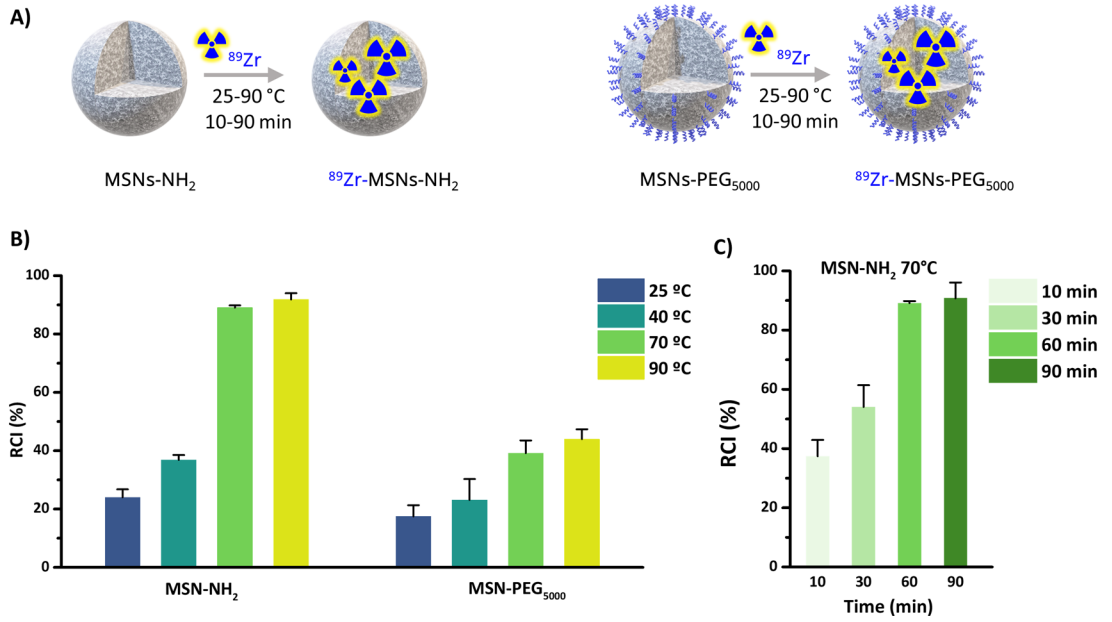

Figure 5.8. *A*) Scheme of labelling approach to optimize the radiolabelling before and after functionalization with PEG; *B*) values of radiochemical incorporation of ^{89}Zr at different temperatures for bare and PEGylated MSNs; and *C*) values of radiochemical incorporation of ^{89}Zr at different times for bare MSNs.

In general terms, incorporation of ^{89}Zr was higher for bare NPs irrespectively of the temperature (25, 40, 70 and 90 °C; 1 hour incubation; see Figure 5.8). In a second set of experiments, bare particles were incubated at 70 °C using different incubation times (10, 30, 60 and 90 min). The results showed that almost quantitative incorporation could be achieved in 60 min, with insignificant improvement at longer times.

Next, the radiochemical stability of ^{89}Zr-MSNs was evaluated *in vitro* by mimicking *in vivo* conditions. With that aim, MSNs at a concentration of 0.1 mg mL^{-1} (below silica solubility) were incubated in different media (Figure 5.9). Results showed a fast release of the radionuclide for bare MSNs, with > 50 % of the radioactivity released at 24 hours. For MSNs-PEG$_{5000}$, a slightly higher stability was found in SBF, but most of the radioactivity was released from the MSNs at t = 72 hours in both media. Contrarily, much higher radiochemical

stability was found when ^{89}Zr-MSNs were incubated at a concentration above 2 mg mL^{-1}, with up to 90 % of the radioactivity remaining in the MSNs at t = 72 h. The lack of stability at low concentrations could be due to the hydrolysis of the silica, which is expected at such a low concentration of NPs.

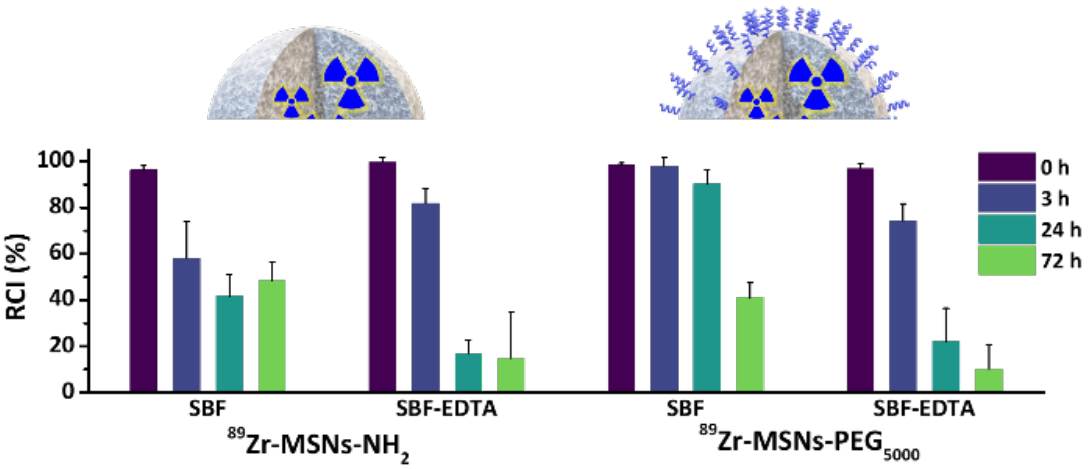

Figure 5.9. Radiochemical stability studies. Data bars show the percentage of remaining of ^{89}Zr labelled NPs incubated at 0.1 mg mL^{-1} silica at 37 °C in simulated body fluid (SBF) and SBF with EDTA.

At concentrations above the solubility limit of silica in water (0.145 mg mL^{-1} at 37 °C for silicic acid),[223] free silicon species saturation is quickly reached, and the silica begins to re-precipitate, apparently stopping the dissolution process. If the MSN concentration is below the solubility limit for silica, re-precipitation is avoided, and MSNs degrade in a few hours. It has been previously shown that at a concentration of 0.1 mg mL^{-1}, 85 % of the starting MSN material is dissolved in 2 hours in simulated body fluid (SBF) before re-precipitation occurs.[224]

5.2.4. Radiochemical incorporation and stability of ^{131}I in the shell of NPs

To evaluate the stability of peptide attached to the particle, the homing peptide was designed to include a tyrosine residue separated from the recognition site of the peptide, to enable radiolabelling using radioiodine.

There are established methods to incorporate iodine in proteins to the aromatic ring group of tyrosine amino acid residue via mild oxidative agents. The oxidizing agent 1,3,4,6-tetrachloro-3α,6α-diphenyl-glycoluril (Pierce™ Iodination Reagent, Iodogen) is a mild oxidizing agent that in the presence of iodine generates electrophilic iodine that undergoes electrophilic aromatic substitution on the aromatic ring of tyrosine.

To achieve radioiodination of the MSNs, PEGylated particles (two different PEG chain lengths) already functionalized with the TT1 peptide were incubated with ^{131}I at room temperature on a tube coated with Iodogen for 30 minutes with frequent shaking. The reaction was quenched by the addition of 10 µl of sodium thiosulphate 100 mM before analysis by radio-TLC to assess radiochemical incorporation. The NPs were centrifuged and washed three times with water and resuspended in PBS at a concentration of 1 - 2 mg ml^{-1}. The peptide was purified with a PD-10 column (Sephadex®) in PBS.

Radiochemical stability of the purified particles was evaluated at a concentration of 0.1 mg mL^{-1} (below silica critical concentration) in SBF, SBF-EDTA and freshly obtained mouse serum.

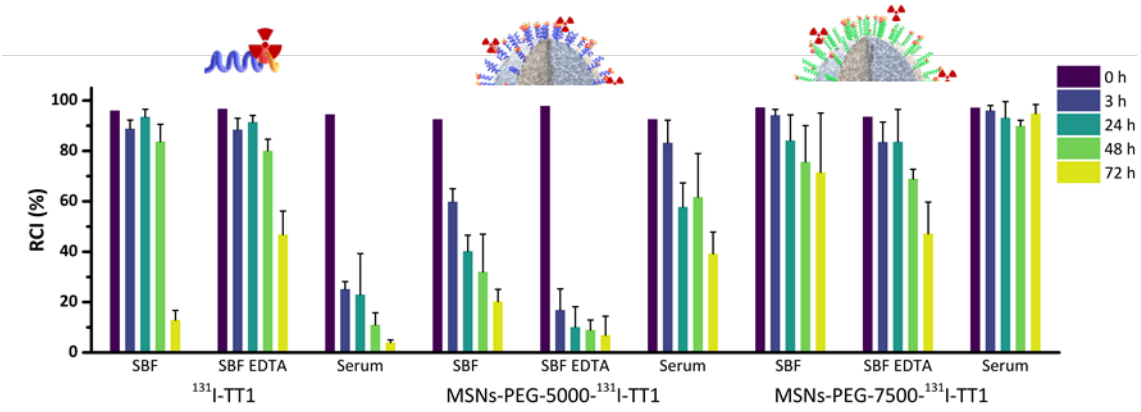

Figure 5.10. Radiochemical stability of ^{131}I TT1 labelled peptide free and attach to the nanoparticle at different medium and times under agitation at 37 °C.

In contrast with the ^{89}Zr, clear differences can be observed among the different systems regarding radioiodine stability. The free peptide presents a fast detachment of the radionuclide in serum, and to a less extent also in SBF-EDTA. The instability of iodine in the presence of serum is due the unspecific degradation of enzyme in pure serum.

The radiochemical stability was measured by radio-HPLC. In these experiments, the peak corresponding to the free, intact labelled peptide is integrated and the area under this peak is divided by the area of all peaks appearing in the chromatogram. Although the different species are not identified, they may represent free radioiodine or small labelled fragments of the peptide. The most relevant value is the decrease of the signal of the entire peptide.

The stability study of the peptide was also carried out by mass spectrometry. Experimentally, the peptide was incubated at 37 °C on a thermomixer at a concentration of 100 μg/ mL in serum. An aliquot of was obtained and mixed with 3 volumes of TFA:ACN 2 %, and subsequently analysed. The chromatograms observed under these conditions indicate that partial segmentation of all the peptides is produced by the enzymes present in serum in less than 2 h, and the initial signal decreases up to 50 % in 20 min (see Figure 5.11).

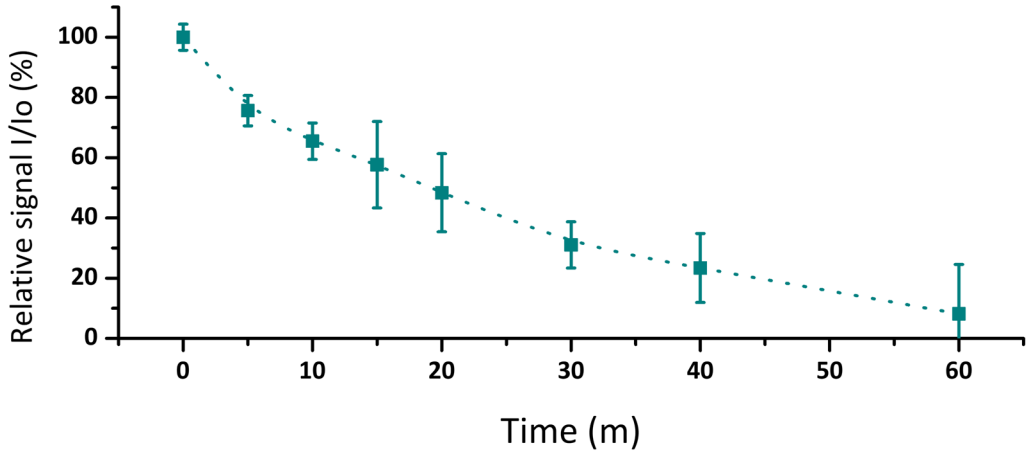

Figure 5.11. Relative intensities of mass spectrometer signal of peptide Lin-TT1 after incubation with serum and PBS at 37 °C, under agitation.

Contrarily to the free peptide, PEGylated particles display a longer radiochemical stability in serum media. We attribute this enhanced stability to the action of PEG, which avoids the interaction of particles with proteins and enzymes, thus protecting the peptide on the surface. The particles showing higher radiochemical stability were those functionalized with PEG 5000, probably due to the higher amount of PEG on the surface, as observed by TGA (Section 5.2.1). These particles were used in subsequent *in vivo* studies.

5.2.5. *In vivo* biodistribution of peptide labelled with a ^{18}F prosthetic group

A short half-lived isotope was used to determine the distribution of the labelled peptide. The biodistribution of the peptide was carried out by radiolabelling with ^{18}F through the primary amine of the germinal cysteine amino acid, following a previously described method[225] and using 6-[^{18}F]fluoronicotinic Acid 2,3,5,6-tetrafluorophenyl ester ([^{18}F]F-Py-TFP) as the labelling agent (see Figure 5.12). In brief, after azeotropic drying of the reactive ^{18}F-complex, 10 mg of the precursor solved in 0.5 mL tBuOH:ACN 4:1 was added and stirred at 40 °C for 20 minutes. The crude of the reaction was purified with a preparative column using 1 % TFA H_2O:ACN 25:75 as the mobile phase. The chromatographic peak

corresponding to the labelled prosthetic group (7.5 min) was collected, diluted with 30 mL of purified water, and concentrated by elution through a Sep-Pak® C-18 cartridge. The cartridge was rinsed with water and dried under helium flow for 5 minutes before final elution with 1 mL of ACN. The radiochemical purity of the labelling agent was determined by radio-HPLC. Total amount of activity obtained was in the range 4 to 8 GBq, with radiochemical purity above 99 %.

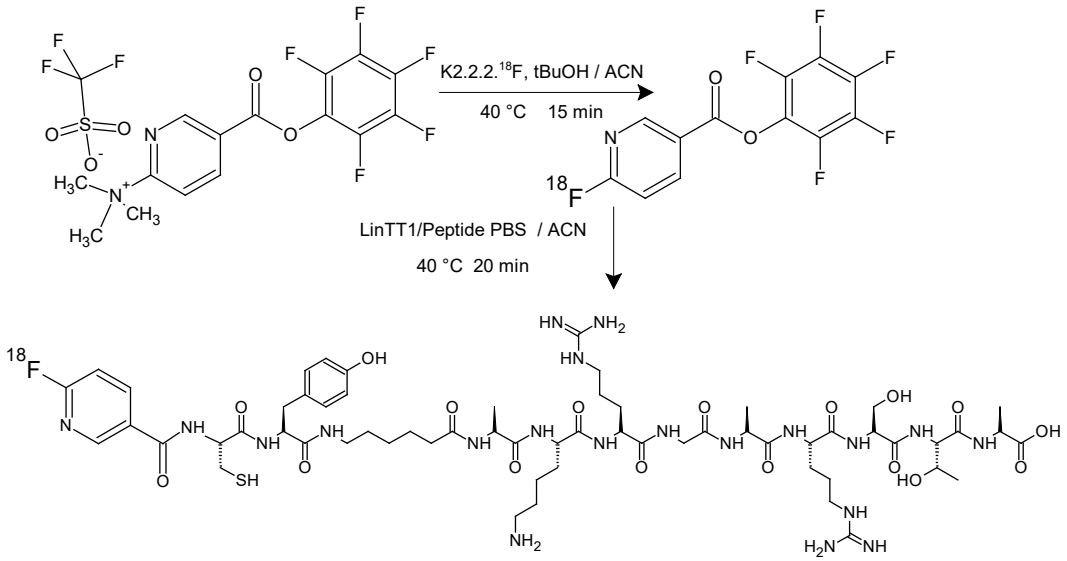

Figure 5.12. Scheme of the labelling of peptide TT1 with the isotope ^{18}F through the prosthetic group [^{18}F]F-Py-TFP.

Radiolabelling of the peptide was carried out by incubation of 200 µl (1 mg mL^{-1}) of the peptide in PBS with 37 MBq of [^{18}F]F-Py-TFP (dissolved in 5 µl of ACN) under shaking at 40 °C for 20 min. To follow the incorporation of the prosthetic group to the peptide, radio-TLC was used. Results showed 95 % incorporation. To purify the undesired species and remove organic solvent, a chromatographic PD−10 column was used. The radiochemical purity was 99 %, as determined by analytical HPLC. The fractions were collected and combined to prepare the dose for injection (5.7 MBq).

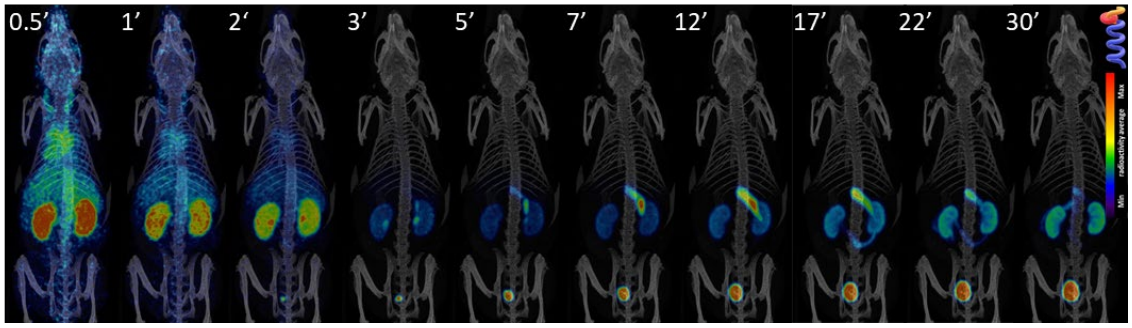

Figure 5.13. Representative Maximum Intensity Projection PET-CT images of the biodistribution of labelled peptide [^{18}F]F-Py-TFP-TT1 at different times points after intravenous administration in wild type animals (coronal views).

To perform imaging studies, mice were anesthetized, and the peptide biodistribution was followed for 2 hours after intravenous administration using PET-CT (see Figure 5.13 for representative images). As it can be seen in the figure, major clearance through the kidneys to the bladder was observed already at short time points, while a fraction of the radioactivity is captured by *Kupffer* cells and subsequently digested to the space of *Disse*, ending into the gallbladder, and gastrointestinal tract.

5.2.6. *In vivo* biodistribution studies in murine xenograft tumour model

Prior to the *in vivo* study imaging, melanoma cancer cells were inoculated subcutaneously in the presence of Matrigel® Matrix, which is a mixture of extracellular protein extracted from Holm Swarm mouse sarcoma cells, that mimics the extracellular environment found in tissues. When incubated at 37 °C the matrix polymerizes, creating a gelatinous matrix containing extracellular growth factor where melanoma cells can proliferate.

To produce the orthotopic xenograft melanoma tumour model, $3{\cdot}10^5$ cell B16F10 in 50 µl were mixed with 50 µl of Matrigel® and inoculated in the right flank of mice C57BL/6. Tumour volume was monitored for 10 days by measuring its size using the formula $V = (L \cdot W^2) / 2$, mm^3. Measuring the length (L) and

thickness (W) with a calliper. When a tumour volume of *ca.* 200 mm^3 was achieved, animals were submitted to imaging studies.

A. Evaluation of the perfusion in melanoma tumour tissue

The perfusion of the tumour was assessed by using the radiotracer $[^{13}N]NH_3$. Labelled ammonia is commonly used to evaluate the perfusion of a tissue of interest. Clinically, this tracer is used as diagnostic tool to evaluate tumour microenvironment and determine irrigation perfusion rates or necrotic regions.

The study was performed by acquiring 5 minutes static PET images at t = 20 minutes post-intravenous administration of 7.4 MBq of $[^{13}N]NH_3$ in saline solution at neutral pH. After PET image acquisition, CT images were acquired for anatomical localization of the radioactive signal.

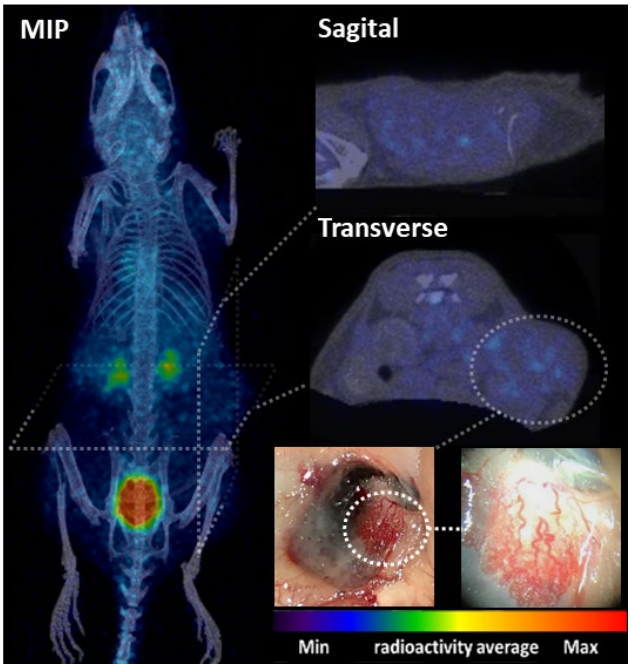

Figure 5.14. *Left*: Representative Maximum Intensity Projection PET-CT image of a tumour-bearing animal after administration of $[^{13}N]NH_3$ (coronal view); *right*: sections of tumour region and detailed microscope vasculature surrounding the tumour tissue.

Twenty minutes after intravenous administration, 95 % of the ammonia is eliminated through the kidney and the urine. The remaining activity corresponds

to the traces in blood and adsorbed metabolized ammonia in the different tissues.[226] Figure 5.14 reveals the presence of radioactivity in the tumour, thus suggesting a normal vascularization of the tissue. Optical microscopy confirmed the presence of the external vasculature draining the tumour, thus proving that the tumour tissue is well irrigated without necrotic regions and the MSNs can be transported by the blood torrent after intravenous administration.

B. Biodistribution of core labelled MSNs with ^{89}Zr by PET-CT

After proving the homing capacity of TT1-modified MSNs *in vitro* and correct perfusion of the tumour tissue, we extended our *in vivo* studies to the evaluation of the biodistribution of ^{89}Zr-MSNs-PEG$_{5000}$ and ^{89}Zr-MSNs-PEG$_{5000}$-TT1 systems synthetized as shown in Figure 5.15.

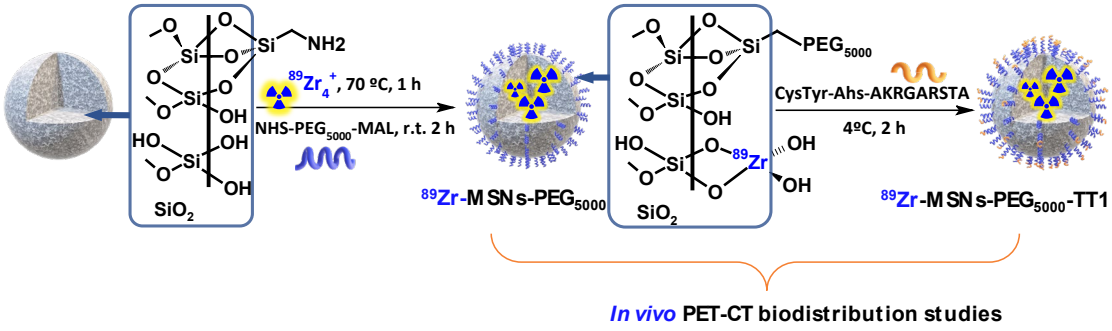

Figure 5.15. Scheme of the preparation route for ^{89}Zr-labelled MSNs used in PET-CT studies.

In brief, 2 mg of MSNs-NH$_2$ where incubated with 85 MBq of ^{89}Zr-oxalate in 200 µl of HEPES buffer at pH 7.4 at 70 °C for 1 h under magnetic stirring. After the incubation time the NPs were washed twice with HEPES and water (500 µL), resuspended in PBS and split to perform the PEGylation step of the different particles. Each fraction (1 mg) of ^{89}Zr-MSNs-NH$_2$ was incubated with MAL-PEG$_{5000}$-NHS or PEG$_{5000}$-NHS (12 µmol). The MSNs were purified by centrifugation and washed three times with PBS, and the ^{89}Zr-MSNs-PEG$_{5000}$-MAL were subsequently incubated with 26 µg of TT1 peptide (0.04 µmol, 1296 Da) at room temperature during 2 h under magnetic stirring. After reaction, the

particles were purified by centrifugation, washed three times with PBS, resuspended in 1 mL of PBS and prepared for injection.. In brief, 2 mg of MSNs-NH_2 where incubated with 85 MBq of ^{89}Zr-oxalate in 200 µl of HEPES buffer at pH 7.4 at 70 °C for 1 h under magnetic stirring. After the incubation time the NPs were washed twice with HEPES and water (500 µL), resuspended in PBS and split to perform the PEGylation step of the different particles. Each fraction (1 mg) of ^{89}Zr-MSNs-NH_2 was incubated with MAL-PEG_{5000}-NHS or PEG_{5000}-NHS (12 µmol). The MSNs were purified by centrifugation and washed three times with PBS, and the ^{89}Zr-MSNs-PEG_{5000}-MAL were subsequently incubated with 26 µg of TT1 peptide (0.04 µmol, 1296 Da) at room temperature during 2 h under magnetic stirring. After reaction, the particles were purified by centrifugation, washed three times with PBS, resuspended in 1 mL of PBS and prepared for injection.

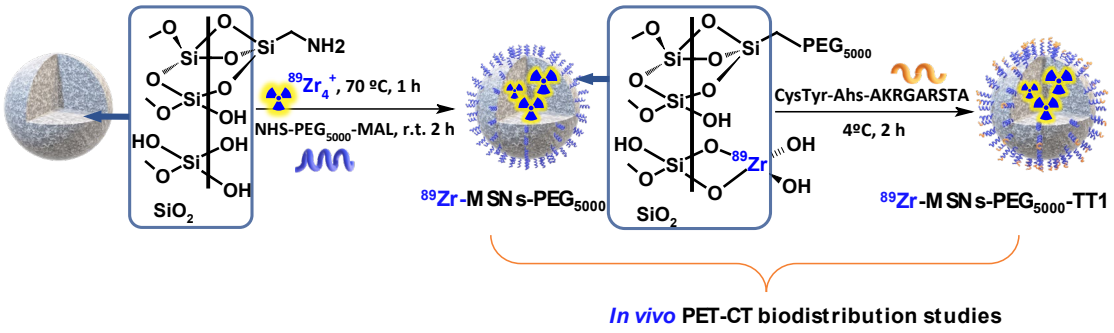

Figure 5.16. Scheme of the preparation route for ^{89}Zr-labelled MSNs used in PET-CT studies.

For in vivo imaging, animals (n = 3 per NP type) bearing tumours with an approximate volume of 200 mm^3 were intravenously injected with 3-5 MBq of ^{89}Zr-labelled MSNs (MSNs-PEG_{5000} and MSNs-PEG_{5000}-TT1; 100 µl; 1 mg mL^{-1}; dose = 5 mg kg^{-1}) and subjected to PET scans at 30 min, 8, 24, and 48 hours after administration.

To quantify the amount of radioactivity in each organ, PET-CT images were analysed by PMOD software. Volumes of interest (VOI) were delineated on the

CT images, the VOIs were transferred to PET images and the concentration of radioactivity in each VOI was determined.

Visual inspection of the images obtained after administration of ^{89}Zr-MSNs-PEG$_{5000}$ (Figure 5.16) confirms a biodistribution pattern of the MSNs with major accumulation in the liver and spleen, with presence of MSNs also in the lungs at short times after administration. This distribution pattern can be attributed to sequestration of the MSNs by the mononuclear phagocytic system. The accumulation of radioactivity in the bones, which is faster for the MSNs lacking the peptide, suggests a progressive release of the radionuclide due to silica dissolution.

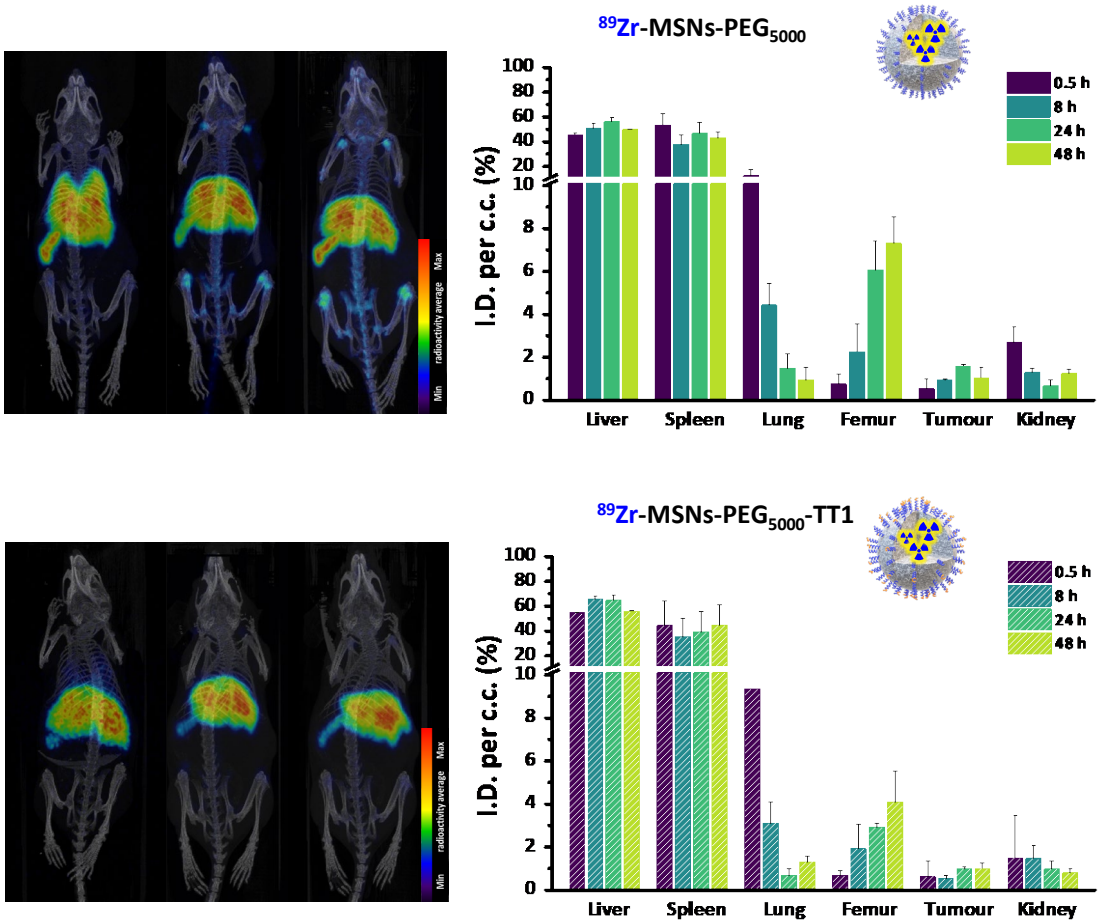

Figure 5.17. Maximum Intensity Coronal Projection (*left*) of PET-CT images showing the biodistribution of core labelled ^{89}Zr-MSNs-PEG$_{5000}$ (*top*) and ^{89}Zr-MSNs-PEG$_{5000}$-TT1 (*bottom*) after

intravenous administration on xerograph B16F10 melanoma tumour bearing mice. Percentage of injected dose per volume (I.D./cc.) of major organs at different times (*right column*) for the two types of NPs.

Quantification of the images confirmed significant accumulation in the liver (46–55 % ID/c.c.) and spleen (47–32 % ID/c.c.), some accumulation in the lungs (20–1 % ID/c.c.), and in femur (0.5–7.5 % ID/c.c.). Accumulation in liver and spleen is stable throughout the duration of the study, while the concentration of radioactivity in the lung decreases with time and a progressive increase is observed in the femur, due to the accumulation of ^{89}Zr cations in the cartilaginous joints of the femur (Figure 5.16 top). The increasing accumulation rate in bones indicates that the mesoporous structure of MSNs is slowly dissolved as shown in our previous work.[227] Accumulation in the tumour is low, around 1 % ID/c.c., and no significant differences were observed between ^{89}Zr-MSNs-PEG$_{5000}$ and ^{89}Zr-MSNs-PEG$_{5000}$-TT1. Overall, there are no major differences observed in the biodistribution of MSNs with or without the homing peptide. A statistical comparison between pairs of organs at each time point shows significant difference in femur at 24 and 48 h (α = 0.05, 95 %), while the other organs do not show differences. The lack of effect of the targeting moiety in terms of tumour accumulation might be due to the low residence time of the NPs in blood, as a consequence of the sequestration of the MSNs by the RES, or loss of the peptide during circulation (see below).

C. Biodistribution ex vivo studies of MSNs functionalized with ^{131}I-labelled TT1 peptide and free peptide

Since results from core labelling did not show major differences between ^{89}Zr-MSNs-PEG$_{5000}$ and ^{89}Zr-MSNs-PEG$_{5000}$-TT1, we hypothesized that this could be due to the loss of the peptide from MSNs during circulation, which would hinder targeting properties. Hence, we incorporated the radiolabel directly into the

tyrosine residue of the peptide. Peptides were anchored through the PEG chain to the MSN surface, and the labelling with ^{131}I was performed as indicated in Section 5.2.1.

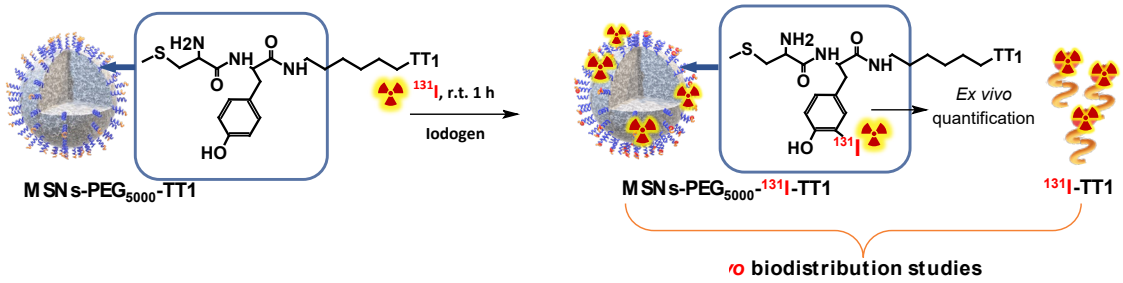

Figure 5.18. Synthetic route for the preparation of MSNs containing ^{131}I labelled TT1 peptide used for *ex vivo* studies.

Stability studies of ^{131}I labelling (Figure 5.10) show that in serum, iodine activity remains on the MSNs, but the free peptide suffers a progressive release of the radioactivity. In addition, the free peptide is rapidly degraded when incubated with blood serum (Figure 5.11). The purified MSNs were injected at least in triplicate to the same B16F10 melanoma tumour mouse model. Parallel experiments were performed with the free peptide. For quantitative data, *ex vivo* experiments were conducted. The same types of NPs with the peptide labelled with ^{131}I (MSNs-PEG$_{5000}$-^{131}I-TT1) and peptide, were administered to mice, which were subsequently sacrificed at predefined time points. At 4, 24 and 48 h after intravenous injection of MSNs, the animals were anesthetized and perfused. Organs were harvested, and the amount of radioactivity was determined by gamma (γ) counting (Figure 5.18). Results confirmed that the free peptide is eliminated through the kidneys and excreted in the urine and intestine over the first 4 hours. No presence of radioactivity could be detected in the thyroid gland, where free iodine tends to be accumulated, thus suggesting the radiochemical stability of the labelled peptide.

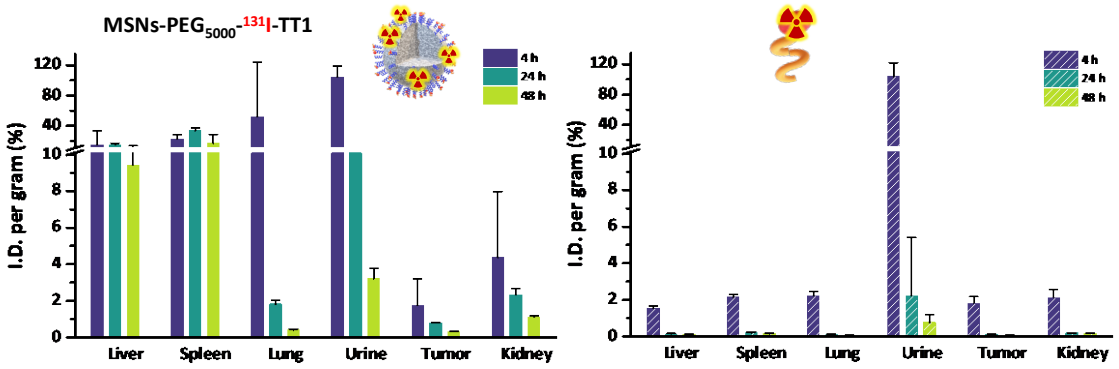

Figure 5.19. Results from *ex vivo* measurements by γ-counter represented quantification of injected dose per gram (I.D./g) of major organ after intravenous administration of MSN-PEG$_{5000}$-^{131}I-TT1 (*left*) and labelled peptide ^{131}I-TT1(*right)*.

NPs labelled through the TT1 peptide show a very different pattern from those labelled at the core. A rapid elimination of the radioactivity via urine was observed within the first 4 hours, with some accumulation in the bladder and in the liver. To a large extent the biodistribution of the labelled NPs resembles that of the free labelled peptide, which is also eliminated via urine within 4 hours following injection. For the NPs, up to 15 % of the injected dose was found in liver, and 30 % in spleen. However, no radioactivity was observed in spleen and liver in case of the free peptide, which leads to the conclusion that the observed biodistribution for the NPs labelled with the peptide probably reflects the fate of the NPs and free peptide simultaneously, as NPs are too big to be eliminated by urine. No radioactivity was observed in the femur, which confirms that the activity observed for the experiments with the labelled core comes from released ^{89}Zr or from degradation products from the NPs, but not from intact NPs, corroborating our hypothesis.[227] No activity for the free labelled peptide could be detected in the lungs, where a high activity for the core labelled NPs was detected. This also hints that ^{89}Zr is present in the lung as free species or associated with the degradation products, but not as NPs. ^{89}Zr interacts with phosphates, which is the reason why it accumulates in the femur, and could also

explain accumulation in the lungs, where there is a large concentration of lipids in the pulmonary surfactant.

For both core and peptide labelled NPs a limited uptake of NPs in tumours was observed. No significant differences due to incorporation of the peptide could be observed for core-labelled NPs. In part this can be understood by the hydrolysis and removal of the targeting peptide from the NPs, which reduces the potential targeting efficacy. It is also clear that NPs largely accumulate in liver/spleen and remain there, thus decreasing the bioavailability of the NPs to reach the tumour.

Results from core labelling show that the NPs degrade liberating ^{89}Zr or degradation products with the radionuclide, that accumulate preferentially in the bones or are eliminated by urine in short times. Radiolabelling of the peptide TT1 on the surface of the NPs shows that the peptide hydrolyses and is eliminated by urine but the biodistribution pattern shows that labelled NPs differ substantially from the free peptide in their fate, showing accumulation in liver and bladder.

Targeting functions as well as stealth coating are normally attached in post functionalization steps following NP synthesis using click chemistry reactions and involving the formation of amides. The efficacy of the NPs to target the desired tissue will finally depend on the stability of the coating around the NP. Despite this issue being fundamental in the design of NPs for biomedical applications, studying the stability of the coating is often neglected and limited to *in vitro* experiments, which may not fully represent the situation *in vivo*. A stable coating *in vitro* may not be so inside the body where circulation, translocation and the interaction with multiple biomolecules and cells can result in a faster and more effective detachment of molecules from the NP surface. The lack of studies on the stability of targeting molecules and stealth is in part due to

the difficulty to trace degradation of NPs *in vivo* and in general of tracing NPs in biological matrixes. Biodistribution studies based on either fluorescence or radiolabelling usually do not address these issues. Indeed, when the labelling is performed in the coating, such as through the targeting molecule, it is assumed that the label remains attached to the NP and that the results on the biodistribution and the efficacy of targeting correspond to the NPs when it is actually coming from the targeting molecules, which may be detached from the NP surface. Conversely, when the NP core is labelled, if the efficacy of targeting and the accumulation of NPs in the targeted tissue are low it is often assumed that the targeting molecule is not effective in directing the NPs, while it may simply be that the targeting molecule has detached.

5.3. Summary and Conclusions

In these chapter we present the synthesis and characterization of PEGylated mesoporous silica NPs (MSNs) with a homing peptide at the surface.

The *in vivo* biological fate of in the MSNs was investigated by incorporating the radiolabel either at the core structure and at the shell of the NPs, the latter by attachment of the radionuclide to the homing peptide. The labelling of the core of the NPs was performed by direct incubation of MSNs with ^{89}Zr. The labelling of the peptide was performed with ^{131}I in the presence of a mild oxidising agent. After radiochemical stability studies, fate studies were performed by *in vivo* PET-CT and *ex vivo* gamma counting, respectively.

The work performed in this chapter demonstrated that the biodistribution of the radiolabelled MSN core provides information of both the fate of the MSN and the products of degradation. By alternatively labelling a peptide attached for targeting MSNs to tumour tissue it has been possible to identify the patterns of

biodistribution that correspond to the MSN and its degradation products more clearly, showing an overwhelming accumulation of the MSNs in liver and spleen while products of degradation of the MSNs accumulate in the bones or are eliminated via urine.

We have also demonstrated that the targeting peptide is partially removed from the MSN and eliminated, which partly explains the practically absent targeting effect of the peptide, along with the rapid accumulation in the liver and spleen. Products of degradation of the MSNs, ^{89}Zr or silicate bearing the radionuclide but not intact MSNs, accumulate in the bones and probably in lung.

An important conclusion that can be reached here is that it is fundamentally important to choose the appropriate pathway for labelling a nanocarrier, as core labelling may provide different information from surface labelling on biodistribution, depending on the stability of the label and the component of the nanomaterials The detachment of the label from the nanoparticle may give a false location for the nanocarrier.

6. General conclusions

1. The preparation of BSA and PEI-stabilised PLGA NPs with hydrodynamic diameter size between 220 and 320 nm and ζ potential values of -20 mV and 35 mV, respectively, has been achieved using the nanoprecipitation method. Due to the long preparation time, this methodology is inappropriate for in vivo studies using nuclear imaging approaches.
2. Monomer ratios used during the preparation of PLGA NPs impact on the capacity of the NPs to entrap hydrophobic drugs. Higher hydrophobic character (greater composition of lactic than glycolic) leads to more efficient encapsulation yields.
3. The preparation of BSA- and PEI-stabilised PLGA NPs with hydrodynamic diameter size between 100 and 300 nm and ζ potential values of -20 mV and 35 mV, respectively, can be achieved using the emulsification method. This method is fast enough to find application in vivo using nuclear imaging approaches. The incorporation of the hydrophobic compound *o*-carborane in 15 % w/w composition leads to irregularities and significant aggregation of the particles.

4. ^{18}F-labelled *o*-carborane loaded into PLGA NPs accumulates in the liver and spleen, with progressive elimination via intestine after intravenous administration, and progressive release from the lungs after intratracheal administration.
5. BSA used as surfactant in the synthesis of the BSA-stabilised PLGA NPs is practically not exchanged by proteins from the media, neither for albumin nor for full plasma. The positively charged PEI binds larger amounts of protein resulting as well in a more stable hard corona around the NPs.
6. PET imaging is not a suitable technique, when used alone, to investigate the protein corona dynamics *in vivo*.
7. Biodistribution studies of peptide-functionalised MSNs radiolabelled at the core with ^{89}Zr and at the shell with ^{131}I provide information of both the fate of the MSN and the products of degradation. Imaging results show significant accumulation of the MSNs in liver and spleen, irrespectively of the labelling position, while products of degradation accumulate in the bones (^{89}Zr-labelled particles) or are eliminated via urine (both labelling approaches).
8. Low accumulation in the tumour of peptide-functionalised MSNs is due to: (i) partial detachment of the targeting peptide from the MSNs; and (ii) rapid accumulation of the MSNs in the liver and spleen, which decreases bioavailability of the nanosystem.

Appendix

A. Materials and Methods

Reagents. All syntheses were carried out with the following commercially available reagents used without further purification: aluminium chloride ($AlCl_3$), ammonium formate (NH_4HCO_2), 3-triethoxysilyl propylamine (APTES), bovine serum albumin (BSA, albumin), calcium chloride ($CaCl_2$), citric acid monohydrate ($C_6H_8O_7 \cdot H_2O$), ethylenediaminetetraacetic acid (EDTA), iodine monochloride (ICl), magnesium chloride hexahydrate ($MgCl_2 \cdot 6\ H_2O$), polyethyleneimine (PEI, branched poly-electrolyte; MW: 40 kDa), poly-lactide-co-glycolide (PLGA 50:50, 75:25 and 85:15; MW: 20, 40 and 50 kDa), potassium carbonate (K_2CO_3), potassium chloride (KCl), di-potassium hydrogen phosphate trihydrate ($K_2HPO_4 \cdot 3\ H_2O$), diethyl ether ($(C_2H_5)_2O$), sodium chloride (NaCl), sodium carbonate (Na_2CO_3), sodium hydrogen carbonate ($NaHCO_3$), sodium thiosulfate ($Na_2S_2O_3$), sodium sulphate (Na_2SO_4), tetraethyl orthosilicate (TEOS), tris-hydroxymethyl aminomethane ($(HOCH_2)_3CNH_2$, Tris), hydrochloric acid (HCl), Kryptofix®222, trifluoracetic acid (TFA) and HPLC grade organic solvents: dichloromethane (CH_2Cl_2, DCM, methylene dichloride), acetonitrile (CH_3CN , ACN, methyl cyanide), dimethyl sulfoxide ($(CH_3)_2SO$, DMSO), ethanol (EtOH), methanol (MeOH), 2-methyl-2-butanol ($CH_3CH_2C(CH_3)_2OH$) and tert-

butyl alcohol (tBuOH) were bought from Sigma-Aldrich (SA, Sant Louis, USA). *Closo-ortho*-carborane was bought from Katchem Ltd. (Prague, Czech Republic).

PEG-NH_2, NHS-PEG-NH_2 (MW 5000 and 7500 Da), Peptides LinTT1 sequence: Cys-Tyr-Ahx-AKRGARSTA, was bought from Peptides International (Louisville, USA) upon sequence demand order, including the incorporation of fluorescence molecule 6-Carboxyfluorescein (FAM) for fluorescence microscope studies.

Alumina and C18 Sep-Pak® cartridges were bought from Waters Corp. (Milford, USA). Prefilled Sephadex G-25® medium PD-10 columns were bought from General Electric (Boston, USA), glass microfiber chromatography paper impregnated with a silica gel (SG) for radio-TLC, was bought from Agilent (Santa Clara, USA)

Nanoprecipitation method. The PLGA polymer with the compound were dissolved in a total volume of 2 ml of organic solvent (acetonitrile/ dichloromethane or acetonitrile/dimethyl sulfoxide/dichloromethane) with a total content of 20 mg or both components. The polymer solution was placed in a syringe pump and dropwise over a 50 mL of anti-solvent aqueous solution of BSA or PEI, with magnetic agitation 800 rpm and immediately later of 80 mL were poured to the previous solution. The excess of solvent, was evaporated and NPs were centrifuged, washed up to five times and resuspended in 1 mL of ultrapure water and characterized.

Emulsification-Evaporation Solvent method. The PLGA polymer with the corresponding amounts of *o*-carborane were dissolved in a total volume of 1 ml of dichloromethane, the solution was place at the bottom of 5 mL flat bottom glass vial (11 x 30 mm) containing a magnetic stirrer (3 x 6 mm) with 3.5 mL aqueous solution of BSA or PEI and chilled at 4 °C before sonication. After 30 second of magnetic agitation at 800 rpm the sonication tip was introduce 12 mm below the level of the liquid and then the O/W emulsion was achieved by the

action of the sonication (Sonics, Vibracell VCX 500 and 750, 3 mm diameter tip, Connecticut, USA). Immediately after the end of sonication the liquid was poured over 80 mL of water under agitation. The excess of solvent, was evaporated and NPs were centrifuged, washed up to five times and resuspended in 1 mL of ultrapure water and characterized.

NMR studies. ^{1}H, ^{13}C, ^{10}B - NMR spectra were recorded on a Bruker AvanceIII 500 NMR (Bruker, Massachusetts, USA) spectrometer at 298 K. Data processing was carried out using Mnova software (Santiago de Compostela, Spain). NMR spectra were recorded in $CHCl_3$, and the chemical shifts were expressed relative to the water peak at 4.8 ppm.

Transmission electron images. TEM studies were conducted in a JEOL JEM−1400 and JEM-2011 (Tokyo, Japan) electron microscope operated at 120 and 200 kV, respectively. The samples were prepared by depositing a drop of nanoparticle suspension onto a copper specimen grid, coated with a holey carbon film, previously treated in a glow discharged chamber for 1 min, and allowing it to dry.

Scanning transmission electron images. STEM-EDX studies were conducted in a JEOL JEM-2011 coupled with an EDX-INCA Oxford Detector system. Energy Dispersive X-ray Spectroscopy (EDXS) of selected areas was carried out for 30 min, in which the sample displacement was automatically corrected every 2 min, by image analysis.

Scanning electron images. SEM studies were conducted in a JEOL JSM-6490. The samples were deposited onto the surface of double tape carbon conductive material, and gold sputtered under vacuum for 1 min, and subsequently placed in the microscopy to conduct the imaging operating at 10 to 20 keV at 10 mm of working distance using the backscattered electron detector.

Dynamic light Scattering and ζ-potential. Particle size analysis was performed using a NanoSizer (Malvern Nano-ZS and Master sizer 3000, Malvern, UK) with 173° scattering angle detector. Each sample was measured at least in triplicate (0.1 mg mL^{-1} in NaCl 10 mM). ζ-potential measurements were carried out with the same NanoSizer equipment at 25 °C and a cell drive voltage of 60 V using a Smoluchowski model.

Cell culture experiments. The B16-F10 (CRL-6475) skin melanoma cell line was bought from the American Type Culture Collection (ATCC®, Virginia, USA). Cells were cultured in RMPI 1640 (Lonza, Basel, Switzerland) supplemented with 10 % foetal bovine serum (FBS), 1 % penicillin/streptomycin and L-Glutamine (Gibco®, Massachusetts, USA) and kept in a humidified atmosphere of 5 % CO_2 at 37 °C. Cells were treated with trypsin-EDTA and seeded at 5000 cell per square centimetre until confluence.

Synthesis of MSNs-FAM-Lin-TT1. NPs used for *in vitro* studies have been conducted with the fluorescence tag molecule 6-Carboxyfluorescein (6-FAM) spaced by a hexanoic chain between from the active peptide sequence. Acrylate-PEG-SCN was incubated with the peptide in PBS and subsequently incubated in the presence of aminated NPs at 1 mg mL-1 for 2 hours at 4 °C and the particles were centrifuged and washed with PBS by triplicate.

Immunofluorescence cell culture experiments. 10^5 cells per well were seeded in 8 well plates for confocal light microscopes (Ibidi®, Bayer, Germany) in 0.2 mL of full RPMI medium. 24 hours later the supernatant was removed, and cells were washed twice with full RPMI. A suspension of 100 μg mL^{-1} of NPS was prepared in RPMI (FBS 1 %) and 100 μL (10 μg) were incubated for 2 hours at 37 °C (at 4 °C to evaluate membrane interaction) to the corresponding well plate. After the incubation time the supernatant was removed, and particles washed

twice with PBS. And the cell was fixated with 200 µl of formaldehyde (4 % in saline solution, pH 7.4) for 10 min, then washed twice with PBS.

Permeation of the cell membrane for fluorescence microscopy. After fixation the cells were incubated for 10 min with 200 µl of DPBST (Triton 0.1 % in DPBS) at room temperature. The supernatant was removed, and cells were washed twice with the same volume of DPBS.

Blocking and immunostaining. Cells were incubated for 1 hour with 2 % BSA in PBST. Then cells were incubated overnight with 1st antibody (antip32 (rabbit)) 1/300 in 1 % BSA in PBST. Washed twice with PBST and incubated 1 hour with the 2nd antibody (Goat anti Rabbit) labelled with the fluorophore 488 (490/525, green emission channel) against rabbit antibody. Then the cells were washed three times with PBST. For nuclei staining 200 µl of DAPI 0.3 µg mL^{-1} in PBS were incubated for 5 min, then washed twice with 200 µl of DPBS.

Sequential staining. The evaluation of the contribution of two different antigen in the same sample, require a double immunofluorescence procedure. In the first blocking step, the cells were incubated with blocking solution (10 % goat serum (secondary antibody), or 1 % gelatine or BSA) for 30 min at room temperature. Then the cells were incubated with the first primary antibody in BSA 1 % in PBST overnight at 4 °C. Cells were washed in triplicate with PBST, followed with the incubation of the first secondary antibody in BSA 1 % in PBST for 1 hour at room temperature. Later cells were washed three times and cells were incubated with anti-FAM 1/200 in BSA 1 % in PBST.

Fluorescence microscopy. Live cell fluorescence images were obtained using Zeiss Axio Observer wide field fluorescence microscope (Carl Zeiss, Germany). For Hoechst staining a Colibri LED module was used for fluorescence excitation at 365 nm and Fluorescence emission was collected using a high-efficiency multi-band pass Colibri filter set which included a 402-488 nm bandpass. A mercury

short-arc HXP lamp was used for the excitation of rhodamine B and the fluorescent emission was collected using an emission filter with a 570 to 640 nm bandpass. Brightfield and fluorescence images were collected and processed using Axio Vision software.

^{89}Zr production. The radionuclide was produced via the ^{89}Y(p,n)^{89}Zr reaction. Briefly, two enriched Yttrium-89 coins (ø = 10 mm x 2 mm), were place inside an aluminium capsule with a degrader (400 barns) case and, irradiated in a Cyclotron IBA 18/9 MeV for 2 h (20 μA). After irradiation the disk was extracted and poured in 3 mL HCl 6 M until dissolution. The obtained liquid was passed through a chemically modified hydroxamate resin solid-phase column[228] and washed with 5 mL of HCl 6 M to remove the excess of non-reactant species and yttrium. To recover the zirconium tree elution of 0.5 mL of HCL 2 M were passed through the cartridge, and the fraction were collected, evaporated, and resuspended with 0.5 mL fraction of Oxalic Acid 1 M.

Silica NPs radiolabelling with ^{89}Zr. 50 μl of ^{89}Zr (37 MBq) in oxalic acid 1 M was neutralized with 200 μl of sodium carbonate, until neutral pH. Suspension of 1 mg of Silica NPs (50 μl of HEPES 10 mM) were incubated with the previous solution for 1 h at 70 °C. The reaction crude was cooled down to room temperature, separated by centrifugation, and washed with 1 mL of HEPES, ultrapure Water and PBS buffer, the resuspended in 300 μl of PBS containing SCN-PEG-OH or SCN-PEG-LinTT1. The optimization of the incubation was performed incubating at different temperatures and time points. Small aliquot was taken to perform iTLC (instant thin layer chromatography), with a mobile phase of 1:9 ACN:(citric acid (20 mM), carbonate (20 mM), EDTA (65 mM) pH 5.0).

Animal's care. The animals have been cared for and handled in accordance with the Guidelines for Accommodation and Care of Animals (European

Convention for the Protection of Vertebrate Animals Used for Experimental and Other Scientific Purposes) internal guidelines, and experimental procedures previously approved by local authorities. Previously to the procedures, animals have been anesthetized with a mixture of 3 to 5 % isoflurane in O_2 for induction and reduced to 1 to 3 % by a nose cone mask, before intravenous injection. During PET-CT imaging acquisitions, rodents were anesthetized and kept at 37 °C using an electric blanket, set up at the base of the PET animal's bed. Subsequently, CT acquisitions were performed to provide anatomical information on each animal.

Tumour inoculation. C57BL/6 mice (6 to 8 weeks old) were used for all in vivo experiments. B16-F10 cells were used for the tumour inoculation and were previously cultured similarly to what described for the *in vitro* experiments. Prior to injecting in vivo, cells were tested for mycoplasma using the commercially available MYCOALERT Mycoplasma Detection Kit (Lonza). For tumour inoculation $3 \cdot 10^5$ cells per mouse were homogenized in Corning® Matrigel Basement Membrane Matrix High Concentration diluted in PSB (1:1 PBS:Matrigel®). All the material (tips, pipettes, syringes, and storage vials) and the cell suspension in Matrigel® were kept in ice until use. The suspension was then loaded in a syringe and 100 µl per mouse was injected into the right back side of the animals using a 26 G needle. Animals were monitored for tumour growth using an electronic digital calliper 779A series (Starrett, Massachusetts, USA) until the tumour size was appropriate to start the biodistribution studies (volume of 100 mm^3, or 6 to 9 days since tumour inoculation).

***In vivo* biodistribution studies by endotracheal insufflations**. Deep sedation was induced (n = 4) placing the animals in an induction chamber with a pure oxygen mixture containing 5 % of isoflurane. The endotracheal insufflations were carried out using a high-pressure syringe Penn-Century Microsprayer® Aerosolizer model FMJ-250 (Penn-Century. Inc. Wyndmoor, USA). The syringe

was loaded with a suspension of the NPs radio-labelled with the corresponding compound. A laryngoscope was used for correct visualization of vocal tract. The tip of the device was placed just above the carina and a pre-defined volume of 50 μL of saline NPs suspension was administered. Immediately after, rats were submitted to *in vivo* imaging acquisition.

***In vivo* biodistribution studies by intravenous administration**. Deep sedation was induced (n = 3) placing the animals in an induction chamber with a pure oxygen mixture containing 5 % of isoflurane. The animals were cannulated and moved to the tempered bed at the PET camera. Pure oxygen mixture containing 1 to 3 percent of isoflurane was administered through cone face mask. Once the stating imaging was initiated, 300-400 μL of labelled NPs suspension was administered.

***In vivo* biodistribution studies of melanoma model.** Tumour bearing mice C57BL/6 with an appropriate tumour volume have been injected with 3.7 MBq were injected with NPs in PBS solution intravenously (100 μL, 1mg mL^{-1}; 5 mg $_{NPs}$ $kg^{-1}{}_{mice}$), while animals where anesthetized PET images were obtained after IV administration of labelled NPs, for 40 min and 4, 8, 24, 48, 72 h after administration. The total radioactivity was measured in a CRC-25R dose calibrator (Calintec, USA) to determine the administered dose in each animal.

Imaging Acquisition. For administration of labelled particles, intravenous injection by the tail vein will be performed, measuring the remaining in the syringe before and after injection to determine the resulting injected activity. After the PET scan, the animal housing bed have been moved to the X-Cube to perform a computer tomography. The acquisition has been repeated at sequential times until the biodistribution profile was defined.

PET image acquisition. Molecubes β-CUBE PET (Gent, Belgium) scanner incorporates a block of thick monolithic LYSO (Lutetium Yttrium Orthosilicate)

scintillator of 25 x 25 x 8 mm coupled to an array of Hamamatsu Multi-Pixel Photon Counters of 3.2 x 3.2 mm. Each of the five rings are provided with nine detectors, generating a cylindrical camera chamber of 45 detectors. As the light function is known to vary upon the interaction depth, the SiPMs provide 5 levels of depth-of-interaction (DOI) measurement. The 45 PET detectors generate a total trans-axial field of view (FOV) of 7.3 cm and 13 cm on the axial plane. Attenuation map of 1 μm^3 voxel resolution is applied to the OSEM reconstruction, in which maximum likelihood clustering algorithm was thirty times iteratively applied, to reconstruct the 3D images according to each interaction with the PET detectors.

CT image acquisition. Molecubes X-CUBE CT is a dedicated micro-CT capable of performing spiral high-resolution computerized tomography of a rodent whole-body scan with a 6.5 cm transverse and 3.5 cm axial FOV, that takes less than 5 min scan per animal. Attenuation map of hard tissues was obtained after ten times Single Scatter Simulation (SSS) of OSEM reconstruction.

PET image reconstruction. CT image performed at 100 μm was used for performing PET attenuation and scatter corrections, to obtain a final PET reconstructed image with 1 mm resolution. After 30 iterations of iterative OSEM images were reconstructed into a 192 x 192 transverse matrix with cubic voxels of 0.4 mm. This equipment provides images with elevated sensitivity and volumetric spatial resolution *ca.* 1 mm^3 for all locations within the imaging FOV.

Nuclear image analyses. Images were reconstructed applying decay and CT-based attenuation correction, factor decay, and analysed by PMOD software (Zurich, Switzerland). Volumes of interest were manually drawn in the major organs, using CT images as anatomical reference. Volumes were transferred to PET images and the concentration of radioactivity have benen calculated for each organ. The values obtained were transformed in real activity (Bq cm^{-3}) and

normalized with injected dose, to obtain the percentage of the injected dose per volume unit of organ at each time.

***Ex vivo* quantification**. After 2, 24, and 48 h post injection of ^{131}I labelled NPs, animals were anesthetized, urine were extracted, and blood collected. To remove the blood from the tissues, heart puncture was performed with 20 mL of heparinized (5 UI mL^{-1}) in saline (NaCl 154 mM). All the organs were weighed and counted in 2470 WIZARD² Automatic Gamma Counter (Perkin Elmer, Massachusetts, USA) for ^{89}Zr activity. The percent injected dose per gram (% ID g^{-1}) for each organ was computed by normalization to the total activity injected (decay-corrected)

B. List of Figures

C. List of Tables

D. List of Contribution

María de los Ángeles Ramírez; Ángel Manuel Martínez-Villacorta; Vanessa Gómez-Vallejo; Patricia Andreozzi; Galo Soler-Illia; Jordi Llop S.E. Moya. Core *vs* surface labelling of mesoporous silica nanoparticles: advancing on understanding nanoparticle fate and on the design of labelling strategies. *Nanoscale Advances* (2022), in press, 10.1039/d1na00719j

Pulagam, Krishna; Henriksen-Lacey, Malou; B. Uribe, Kepa; Renero-Lecuna, Carlos; Kumar, Jatish; Charalampopoulou, Alexandra; Facoetti, Angelica; Protti, Nicoletta; Gómez-Vallejo, Vanessa; Baz, Zuriñe; Kumar, Vished; Sánchez-Iglesias, Ana; Altieri, Saverio; Cossío, Unai; Di Silvio, Desirè; Martínez-Villacorta, Ángel; Ruiz de Angulo, Ane; Rejc, Luka; Liz-Marzán, Luis; Llop, Jordi. In Vivo Evaluation of Multifunctional Gold Nanorods for Boron Neutron Capture and Photothermal Therapies. *ACS Applied Materials & Interfaces* (2021), 13, 42, 49589-49601. 10.1021/acsami.0c17575

S.C. Romero, H. Groult, O. Cañadas, B. Garcia-Fojeda, M. Azkargorta, I. Lloro, A.V. Lechuga-Vieco, Á. M. Martínez-Villacorta, F. Herranz, F. Elortza, C. Casals, J. Ruiz-Cabello. Protein Corona Induced by Lung Surfactant Interactions Determines the In Vivo Fate of Micellar Nanostructures Designed for Pulmonary Administration. *American Journal of Respiratory and Critical Care Medicine* (2020) 10.1164/ajrccm-conference.2020.201.1_MeetingAbstracts.A2292

Escobar, A., Muzzio, N. E.; Martínez, Á.; Abarrategi, A.; Grzelczak, M.; Bordoni, A. V, Sergio, E. (2019). Mesoporous Titania Coatings with carboxylated Pores for Complexation and slow Delivery of Strontium for osteogenic Induction. *Applied Surface Science*, **145172** (2019) 10.1016/j.apsusc.2019.145172

Wang, W.; Ciganda, R.; Wang, C.; Escobar, A.; Martinez-Villacorta, Á. M.; Ramirez, M. D. L. … A.; Astruc, D. High catalytic activity of Rh nanoparticles

generated from cobaltocene and RhCl3 in aqueous solution. *Inorganic Chemistry Frontiers*, **6**(10), 2704–2708 (2019) 10.1039/c9qi00742c

Escobar, A.; Muzzio, N.; Angelomé, P. C.; Bordoni, A. V.; Martínez, Á.; Bindini, E.; … Moya, S. E. Strontium Titanate (SrTiO3) Mesoporous Coatings for Enhanced Strontium Delivery and Osseointegration on Bone Implants. *Advanced Engineering Materials*, **21**(7), 1–8 (2019) 10.1002/adem.201801210

Coneo Rodríguez, R.; Yate, L.; Coy, E.; Martínez-Villacorta, Á. M.; Bordoni, A. V.; Moya, S.; & Angelomé, P. C. (2019). Copper nanoparticles synthesis in hybrid mesoporous thin films: Controlling oxidation state and catalytic performance through pore chemistry. *Applied Surface Science*, ***471***, 862–868 (2018) 10.1016/j.apsusc.2018.12.068

Vilela, D.; Cossío, U.; Parmar, J.; Martínez-Villacorta, A. M.; Gómez-Vallejo, V.; Llop, J.; & Sánchez, S. Medical Imaging for the Tracking of Micromotors. *ACS Nano*, ***12***(2), 1220–1227 (2018) 10.1021/acsnano.7b07220

Wang, Q.; Fu, F.; Martinez-Villacorta, A. M.; Moya, S.; Salmon, L.; Vax, A.; Astruc, D. Electron Flow in Large Metallomacromolecules and Electronic Switching of Nanoparticle Stabilization: Click Ferrocenyl Dentromers that Reduce AuIII to Au Nanoparticles. *Chemistry - A European Journal*, **24**(48), 12686–12694 (2018) 10.1002/chem.201802289

Fu, F.; Wang, C.; Wang, Q.; Martinez-Villacorta, A. M.; Escobar, A.; Chong, H.; Astruc, D. Highly Selective and Sharp Volcano-type Synergistic Ni2Pt@ZiF-8-Catalyzed Hydrogen Evolution from Ammonia Borane Hydrolysis. *Journal of the American Chemical Society*, ***140***(31), 10034–10042 (2018) 10.1021/jacs.8b06511

Fu, F.; Ciganda, R.; Wang, Q.; Tabey, A.; Wang, C.; Escobar, A.; Martínez-Villacorta, Á. M.; Astruc, D. Cobaltocene Reduction of Cu and Ag Salts and

Catalytic Behaviour of the Nanoparticles Formed. *ACS Catalysis*, 8100–8106 (2018) 10.1021/acscatal.8b02338

Fu, F.; Martínez, Á.; Wang, C.; Ciganda, R.; Yate, L.; Escobar, A.; Astruc, D. Exposure to air boosts CuAAC reactions catalyzed by PEG-stabilized Cu nanoparticles. *Chemical Communications*, ***53***(39), 5384–5387 (2017) 10.1039/c7cc02504a

Ciganda, R.; Gu, H.; Hernandez, R.; Escobar, A.; Martínez, Á.; Yates, L.; Astruc, D. Electrostatic Assembly of Functional and Macromolecular Ferricinium Chloride-Stabilized Gold Nanoparticles. *Inorganic Chemistry*, ***56***(5), 2784–2791 (2017) 10.1021/acs.inorgchem.6b02850

Fu, F.; Martínez-Villacorta, Á. M.; Escobar, A.; Irigoyen, J.; Moya, S.; Fouquet, E.; Astruc, D. Synthesis of late transition-metal nanoparticles by Na naphthalenide reduction of salts and their catalytic efficiency. *Inorganic Chemistry Frontiers*, ***4***(12), 2037–2044 (2017) 10.1039/c7qi00530j

Díez-Martínez, R.; García-Fernández, E.; Manzano, M.; Martínez, Á.; Domenech, M.; Vallet-Regí, M.; García, P. Auranofin-loaded nanoparticles as a new therapeutic tool to fight streptococcal infections. *Scientific Reports*, ***6***, 19525 (2016) 10.1038/srep19525

Liu, X.; Gregurec, D.; Irigoyen, J.; Martínez, Á.; Moya, S.; Ciganda, R.; Astruc, D. Precise localization of metal nanoparticles in dendrimer nanosnakes or inner periphery and consequences in catalysis. *Nature Communications*, **7**, 13152 (2016) 10.1038/ncomms13152

E. References

1. Taniguchi, N. On the basic concept of Nanotechnology. in *Proceedings of the International Conference on Production Engineering* 18–23 (1974).
2. Feynman, R. P. There is plenty of room at the bottom for innovation. *J.*

micro-electromechanical Syst. **1**, 60–66 (1992).

3. Barber, D. J. & Freestone, I. C. An investigation of the origin of the colour of the Lycurgus Cup by analytical transmission electron microscopy. *Archaeometry* **32**, 33–45 (1990).
4. Sánchez del Río, M. *et al.* The Maya Blue Pigment. in *Developments in Clay Science* vol. 3 453–481 (2011).
5. Ouellet-Plamondon, C. *et al.* The Maya blue nanostructured material concept applied to colouring geopolymers. *RSC Adv.* **5**, 98834–98841 (2015).
6. Volle, N. *et al.* Maya Blue as natural coloring fillers in a multi-scale polymer-clay nanocomposite. *Compos. Sci. Technol.* (2011) doi:10.1016/j.compscitech.2011.07.009.
7. Radu, D. R., Lai, C.-Y., Wiench, J. W., Pruski, M. & Lin, V. S.-Y. Gatekeeping Layer Effect: A Poly(lactic acid)-coated Mesoporous Silica Nanosphere-Based Fluorescence Probe for Detection of Amino-Containing Neurotransmitters. *J. Am. Chem. Soc.* **126**, 1640–1641 (2004).
8. Ashby, M. F., Ferreira, P. J. & Schodek, D. L. *Nanomaterials, Nanotechnologies and Design*. *Nanomaterials, Nanotechnologies and Design* (2009). doi:10.1016/B978-0-7506-8149-0.00013-1.
9. Wang, G. Nanotechnology: The New Features. *ArXiv* **1812.04939**, (2018).
10. Pita, R., Ehmann, F. & Papaluca, M. Nanomedicines in the EU—Regulatory Overview. *AAPS J.* **18**, 1576–1582 (2016).
11. Farokhzad, O. C. & Langer, R. Impact of nanotechnology on drug delivery. *ACS Nano* **3**, 16–20 (2009).
12. Prokop, A. & Davidson, J. Nanovehicular intracellular delivery systems. *J. Pharm. Sci.* **97**, 3518–3590 (2008).
13. Fadeel, B. Nanosafety: towards safer design of nanomedicines. *J. Intern. Med.* **274**, 578–580 (2013).
14. Drmota, A., Drofenik, M., Koselj, J. & nidari, A. Microemulsion Method for Synthesis of Magnetic Oxide Nanoparticles. *Microemulsions - An Introd. to Prop. Appl.* (2012) doi:10.5772/36154.
15. García, M. C., Aloisio, C., Onnainty, R. & Ullio-Gamboa, G. *Self-assembled nanomaterials*. *Nanobiomaterials: Nanostructured Materials for Biomedical Applications* (Elsevier Ltd., 2018). doi:10.1016/B978-0-08-100716-7.00003-9.
16. Xi, J. & Talaat, M. Nanoparticle deposition in rhythmically moving acinar models with interalveolar septal apertures. *Nanomaterials* **9**, (2019).

17. Minelli, C., Lowe, S. B. & Stevens, M. M. Engineering nanocomposite materials for cancer therapy. *Small* **6**, 2336–2357 (2010).

18. Tee, J. K. *et al.* Nanoparticles' interactions with vasculature in diseases. *Chem. Soc. Rev.* **48**, 5381–5407 (2019).

19. Villegas, M. R., Baeza, A. & Vallet-Regí, M. Nanotechnological Strategies for Protein Delivery. *Molecules* **23**, 1008 (2018).

20. Lin, C. Y., Javadi, M., Belnap, D. M., Barrow, J. R. & Pitt, W. G. Ultrasound sensitive eLiposomes containing doxorubicin for drug targeting therapy. *Nanomedicine Nanotechnology, Biol. Med.* **10**, 67–76 (2014).

21. M.Hiller, A., W.Lloy, A. & Swarbrick, J. *Drug Delivery and Targeting. For Pharmacists and Pharmaceutical Scientists*. (2001).

22. Vallet-Regí, M., Ruiz-Hernández, E., González, B. & Baeza, A. Design of smart nanomaterials for drug and gene delivery. *J. Biomater. Tissue Eng.* **1**, 6–29 (2011).

23. Nel, A. E. *et al.* Understanding biophysicochemical interactions at the nano-bio interface. *Nat. Mater.* **8**, 543–557 (2009).

24. Lazarovits, J., Chen, Y. Y., Sykes, E. A. & Chan, W. C. W. Nanoparticle-blood interactions: The implications on solid tumour targeting. *Chem. Commun.* **51**, 2756–2767 (2015).

25. Papini, E., Tavano, R. & Mancin, F. Opsonins and Dysopsonins of Nanoparticles: Facts, Concepts, and Methodological Guidelines. *Front. Immunol.* **11**, 1–19 (2020).

26. Soo Choi, H. *et al.* Renal clearance of quantum dots. *Nat. Biotechnol.* **25**, 1165–1170 (2007).

27. Alexis, F., Pridgen, E., Molnar, L. K. & Farokhzad, O. C. Factors affecting the clearance and biodistribution of polymeric nanoparticles. *Mol. Pharm.* **5**, 505–515 (2008).

28. Stepien, G. *et al.* Effect of Surface Chemistry and Associated Protein Corona on the Long-Term Biodegradation of Iron Oxide Nanoparticles In Vivo. *ACS Appl. Mater. Interfaces* **10**, 4548–4560 (2018).

29. Owens III, D. E. & Peppas, N. A. Opsonization, biodistribution, and pharmacokinetics of polymeric nanoparticles. *Int. J. Pharm.* **307**, 93–102 (2006).

30. Zhao, P. *et al.* Paclitaxel loaded folic acid targeted nanoparticles of mixed lipid-shell and polymer-core: In vitro and in vivo evaluation. *Eur. J. Pharm. Biopharm.* **81**, 248–256 (2012).

31. Ghotbi, Z. *et al.* Active targeting of dendritic cells with mannan-decorated PLGA nanoparticles. *J. Drug Target.* **19**, 281–292 (2011).

32. Falvo, E. *et al.* Improved Doxorubicin Encapsulation and Pharmacokinetics of Ferritin–Fusion Protein Nanocarriers Bearing Proline, Serine, and Alanine Elements. *Biomacromolecules* **17**, 514–522 (2016).

33. Deng, Y. *et al.* The effect of hyperbranched polyglycerol coatings on drug delivery using degradable polymer nanoparticles. *Biomaterials* **35**, 6595–6602 (2014).

34. Das, P. & Jana, N. R. Highly colloidally stable hyperbranched polyglycerol grafted red fluorescent silicon nanoparticle as bioimaging probe. *ACS Appl. Mater. Interfaces* **6**, 4301–4309 (2014).

35. Kavitha, A. & Parambath, A. Polyacrylamide and related polymers. in *Engineering of Biomaterials for Drug Delivery Systems* 229–253 (Elsevier, 2018). doi:10.1016/B978-0-08-101750-0.00008-8.

36. Bergese, P. & Hamad-Schii, K. *Nanomaterial Interfaces in Biology Methods and Protocols Methods in Molecular Biology 1025*.

37. Ulbrich, K. & Šubr, V. Structural and chemical aspects of HPMA copolymers as drug carriers. *Adv. Drug Deliv. Rev.* **62**, 150–166 (2010).

38. Estephan, Z. G., Jaber, J. A. & Schlenoff, J. B. Zwitterion-Stabilized Silica Nanoparticles: Toward Nonstick Nano. *Langmuir* **26**, 16884–16889 (2010).

39. Adams, N. & Schubert, U. S. Poly(2-oxazolines) in biological and biomedical application contexts. *Adv. Drug Deliv. Rev.* **59**, 1504 (2007).

40. Mero, A. *et al.* Synthesis and characterization of poly(2-ethyl 2-oxazoline)-conjugates with proteins and drugs: Suitable alternatives to PEG-conjugates? *J. Control. Release* **125**, 87–95 (2008).

41. Ashley, C. E. *et al.* Delivery of Small Interfering RNA by Peptide-Targeted Mesoporous Silica Nanoparticle-Supported Lipid Bilayers. *ACS Nano* **6**, 2174–2188 (2012).

42. Liang, Y., Duan, L., Lu, J. & Xia, J. Engineering exosomes for targeted drug delivery. *Theranostics* vol. 11 3183–3195 (2021).

43. Mazur, F. & Chandrawati, R. Membrane Fusion Models for Bioapplications. *ChemNanoMat* vol. 7 223–237 (2021).

44. Bulbake, U., Doppalapudi, S., Kommineni, N. & Khan, W. Liposomal formulations in clinical use: An updated review. *Pharmaceutics* **9**, 1–33 (2017).

45. Kianfar, E. Protein nanoparticles in drug delivery: animal protein, plant

proteins and protein cages, albumin nanoparticles. *Journal of Nanobiotechnology* vol. 19 (2021).

46. Chung, Y. H., Cai, H. & Steinmetz, N. F. Viral nanoparticles for drug delivery, imaging, immunotherapy, and theranostic applications. *Advanced Drug Delivery Reviews* vol. 156 214–235 (2020).

47. Wiesner, M. R., Lowry, G. V., Alvarez, P., Dionysiou, D. & Biswas, P. Assessing the risks of manufactured nanomaterials. *Environmental Science and Technology* vol. 40 4336–4345 (2006).

48. Sahay, G., Alakhova, D. Y. & Kabanov, A. V. Endocytosis of nanomedicines. *J. Control. Release* **145**, 182–195 (2010).

49. Fornaguera, C. & García-Celma, M. J. Personalized nanomedicine: A revolution at the nanoscale. *J. Pers. Med.* **7**, 14–21 (2017).

50. Choi, Y. H. & Han, H. K. Nanomedicines: current status and future perspectives in aspect of drug delivery and pharmacokinetics. *J. Pharm. Investig.* **48**, 43–60 (2018).

51. Anselmo, A. C. & Mitragotri, S. Nanoparticles in the clinic: An update. *Bioeng. Transl. Med.* **4**, 1–16 (2019).

52. Abdellatif, A. A. H. & Alsowinea, A. F. Approved and marketed nanoparticles for disease targeting and applications in COVID-19. *Nanotechnol. Rev.* **10**, 1941–1977 (2021).

53. Hua, S., de Matos, M. B. C., Metselaar, J. M. & Storm, G. Current trends and challenges in the clinical translation of nanoparticulate nanomedicines: Pathways for translational development and commercialization. *Front. Pharmacol.* **9**, 1–14 (2018).

54. Singer, A., Markoutsa, E., Limayem, A., Mohapatra, S. & Mohapatra, S. S. Nanobiotechnology Medical Applications: Overcoming Challenges Through Innovation. *EuroBiotech J.* **2**, 146–160 (2018).

55. Bueno, C. Z., Oliveira, C. A. & Rangel-Yagui, C. O. Polymeric and liposomal nanomaterials. in *Nanobiomaterials* 437–464 (Elsevier, 2018). doi:10.1016/B978-0-08-100716-7.00017-9.

56. Conn, J., Oyasu, R., Welsh, M. & Beal, J. M. Vicryl (polyglactin 910) synthetic absorbable sutures. *Am. J. Surg.* **128**, 19–23 (1974).

57. Sugar, H. S., Lorfel, R. & Summer, D. Polyglycolic acid (Dexon) sutures in cataract surgery. *Am. J. Ophthalmol.* **77**, 178–180 (1974).

58. Chatterjee, S. Comparative trial of Dexon (polyglycolic acid), collagen, and silk sutures in ophthalmic surgery. *Br. J. Ophthalmol.* **59**, 736–740 (1975).

59. Trimaille, T., Gurny, R. & Möller, M. Synthesis and properties of novel poly(hexyl-substituted lactides) for pharmaceutical applications. *Chimia (Aarau).* **59**, 348–352 (2005).

60. Nihant, N., Schugens, C., Grandfils, C., Jerome, R. & Teyssie, P. Polylactide microparticles prepared by double emulsion-evaporation. II. Effect of the poly(lactide-co-glycolide) composition on the stability of the primary and secondary emulsions. *J. Colloid Interface Sci.* **173**, 55–65 (1995).

61. Schnettler, R. *et al.* Glycerol-l-lactide coating polymer leads to delay in bone ingrowth in hydroxyapatite implants. *J. Control. Release* **106**, 154–161 (2005).

62. Makadia, H. K. & Siegel, S. J. Poly Lactic-co-Glycolic Acid (PLGA) as Biodegradable Controlled Drug Delivery Carrier. *Polymers (Basel).* **3**, 1377–1397 (2011).

63. Wiggins, J. S., Hassan, M. K., Mauritz, K. A. & Storey, R. F. Hydrolytic degradation of poly(d,l-lactide) as a function of end group: Carboxylic acid vs. hydroxyl. *Polymer (Guildf).* **47**, 1960–1969 (2006).

64. Tsuji, H., Mizuno, A. & Ikada, Y. Properties and morphology of poly(L-lactide). III. Effects of initial crystallinity on long-termin vitro hydrolysis of high molecular weight poly(L-lactide) film in phosphate-buffered solution. *J. Appl. Polym. Sci.* **77**, 1452–1464 (2000).

65. Schliecker, G., Schmidt, C., Fuchs, S., Wombacher, R. & Kissel, T. Hydrolytic degradation of poly(lactide-co-glycolide) films: effect of oligomers on degradation rate and crystallinity. *Int. J. Pharm.* **266**, 39–49 (2003).

66. Silva, A. T. C. R., Cardoso, B. C. O., Silva, M. E. S. R. e, Freitas, R. F. S. & Sousa, R. G. Synthesis, Characterization, and Study of PLGA Copolymer <i>in Vitro</i> Degradation. *J. Biomater. Nanobiotechnol.* **6**, 8–19 (2015).

67. Miladi, K., Sfar, S., Fessi, H. & Elaissari, A. *Polymer Nanoparticles for Nanomedicines*. (Springer International Publishing, 2016). doi:10.1007/978-3-319-41421-8.

68. Lagreca, E. *et al.* Recent advances in the formulation of PLGA microparticles for controlled drug delivery. *Prog. Biomater.* **9**, 153–174 (2020).

69. Singh, S. & Singha, P. Effect of Modifications in Poly (Lactide-co-Glycolide) (PLGA) on Drug Release and Degradation Characteristics: A Mini Review. *Curr. Drug Deliv.* **18**, 1378–1390 (2021).

70. Yoo, J. & Won, Y. Y. Phenomenology of the Initial Burst Release of Drugs

from PLGA Microparticles. *ACS Biomaterials Science and Engineering* vol. 6 6053–6062 (2020).

71. Andhariya, J. V. *et al.* In vitro-in vivo correlation of parenteral PLGA microspheres: Effect of variable burst release. *J. Control. Release* **314**, 25–37 (2019).

72. Rodrigues de Azevedo, C. *et al.* Modeling of the burst release from PLGA micro- and nanoparticles as function of physicochemical parameters and formulation characteristics. *Int. J. Pharm.* **532**, 229–240 (2017).

73. Tacheva, B. *et al.* Drug Exchange between Albumin Nanoparticles and Erythrocyte Membranes. *Nanomaterials* **9**, 47 (2019).

74. Makriyannis, A., Guo, J. & Tian, X. Albumin enhances the diffusion of lipophilic drugs into the membrane bilayer. in *Life Sciences* vol. 77 1605–1611 (2005).

75. Campardelli, R., Oleandro, E. & Reverchon, E. Supercritical assisted injection in a liquid antisolvent for PLGA and PLA microparticle production. *Powder Technol.* **287**, 12–19 (2016).

76. Alexis, F. Factors affecting the degradation and drug-release mechanism of poly(lactic acid) and poly[(lactic acid)-co-(glycolic acid)]. *Polym. Int.* **54**, 36–46 (2005).

77. Ali, M. E. & Lamprecht, A. Spray freeze drying for dry powder inhalation of nanoparticles. *Eur. J. Pharm. Biopharm.* **87**, 510–517 (2014).

78. Lu, L., Garcia, C. A. & Mikos, A. G. In vitro degradation of thin poly(DL-lactic-co-glycolic acid) films. *J. Biomed. Mater. Res.* **46**, 236–244 (1999).

79. Verma, V., Ryan, K. M. & Padrela, L. Production and isolation of pharmaceutical drug nanoparticles. *Int. J. Pharm.* **603**, 120708 (2021).

80. Lü, J. M. *et al.* Current advances in research and clinical applications of PLGA-based nanotechnology. *Expert Review of Molecular Diagnostics* vol. 9 325–341 (2009).

81. Rezvantalab, S. & Keshavarz Moraveji, M. Microfluidic assisted synthesis of PLGA drug delivery systems. *RSC Adv.* **9**, 2055–2072 (2019).

82. Fessi, H., Puisieux, F., Devissaguet, J. P., Ammoury, N. & Benita, S. Nanocapsule formation by interfacial polymer deposition following solvent displacement. *Int. J. Pharm.* **55**, 1–4 (1989).

83. D'Addio, S. M. & Prud'homme, R. K. Controlling drug nanoparticle formation by rapid precipitation. *Adv. Drug Deliv. Rev.* **63**, 417–426 (2011).

84. Neppiras, E. A. Physical principles of ultrasonic technology. *Ultrasonics* **14**,

138–139 (1976).

85. Lepoint, T., Pauw, D. De, Goldman, M. & Goldman, A. Sonoluminescence : An alternative '" electrohydrodynamic "'. *J. Acoust. Soc. Am.* **101**, 2012–2030 (1997).

86. Niemczewski, B. A comparison of ultrasonic cavitation intensity in liquids. *Ultrasonics* **18**, 107–110 (1980).

87. Kresge, C. T., Leonowicz, M. E., Roth, W. J., Vartuli, J. C. & Beck, J. S. Ordered mesoporous molecular sieves synthesized by a liquid-crystal template mechanism. *Nature* **359**, 710–712 (1992).

88. Rahmat, N., Abdullah, A. Z. & Mohamed, A. R. A review: Mesoporous Santa Barbara amorphous-15, types, synthesis and its applications towards biorefinery production. *Am. J. Appl. Sci.* **7**, 1579–1586 (2010).

89. Qiao, Z. a, Zhang, L., Guo, M. Y., Liu, Y. L. & Huo, Q. S. Synthesis of Mesoporous Silica Nanoparticles via Controlled Hydrolysis and Condensation of Silicon Alkoxide. *Chem. Mater.* **21**, 3823–3829 (2009).

90. Zhang, H., Wu, J., Zhou, L., Zhang, D. & Qi, L. Facile synthesis of monodisperse microspheres and gigantic hollow shells of mesoporous silica in mixed water-ethanol solvents. *Langmuir* **23**, 1107–13 (2007).

91. Yamada, H., Urata, C., Ujiie, H., Yamauchi, Y. & Kuroda, K. Preparation of aqueous colloidal mesostructured and mesoporous silica nanoparticles with controlled particle size in a very wide range from 20 nm to 700 nm. *Nanoscale* **5**, 6145 (2013).

92. Yan, Z., Meng, H., Shi, L., Li, Z. & Shen, P. K. Synthesis of mesoporous hollow carbon hemispheres as highly efficient Pd electrocatalyst support for ethanol oxidation. *Electrochem. commun.* **12**, 689–692 (2010).

93. Sun, J. & Bao, X. Textural manipulation of mesoporous materials for hosting of metallic nanocatalysts. in *Chemistry - A European Journal* vol. 14 7478–7488 (2008).

94. Serrano, E., Linares, N., Garcia-Martinez, J. & Berenguer, J. R. Sol-Gel Coordination Chemistry: Building Catalysts from the Bottom-Up. *ChemCatChem* vol. 5 844–860 (2013).

95. Sangvanich, T. *et al.* Novel oral detoxification of mercury, cadmium, and lead with thiol-modified nanoporous silica. *ACS Appl. Mater. Interfaces* **6**, 5483–5493 (2014).

96. Yantasee, W. *et al.* Functionalized nanoporous silica for the removal of heavy metals from biological systems: Adsorption and application. *ACS Appl. Mater. Interfaces* **2**, 2749–2758 (2010).

97. Walcarius, A. & Mercier, L. Mesoporous organosilica adsorbents: Nanoengineered materials for removal of organic and inorganic pollutants. *J. Mater. Chem.* **20**, 4478–4511 (2010).

98. He, Q. & Shi, J. Mesoporous silica nanoparticle based nano drug delivery systems: synthesis, controlled drug release and delivery, pharmacokinetics and biocompatibility. *J. Mater. Chem.* **21**, 5845 (2011).

99. Ma'Mani, L. *et al.* Curcumin-loaded guanidine functionalized PEGylated I3ad mesoporous silica nanoparticles KIT-6: Practical strategy for the breast cancer therapy. *Eur. J. Med. Chem.* **83**, 646–654 (2014).

100. Slowing, I. I., Vivero-Escoto, J. L., Wu, C.-W. & Lin, V. S.-Y. Mesoporous silica nanoparticles as controlled release drug delivery and gene transfection carriers. *Adv. Drug Deliv. Rev.* **60**, 1278–88 (2008).

101. Shadjou, N. & Hasanzadeh, M. Silica-based mesoporous nanobiomaterials as promoter of bone regeneration process. *Journal of Biomedical Materials Research - Part A* vol. 103 3703–3716 (2015).

102. Vallet-Regí, M., Colilla, M. & Izquierdo-Barba, I. Bioactive mesoporous silicas as controlled delivery systems: Application in bone tissue regeneration. *Journal of Biomedical Nanotechnology* vol. 4 1–15 (2008).

103. Escobar, A. *et al.* One-Step Synthesis of Mesoporous Silica Thin Films Containing Available COOH Groups. *ACS Omega* **2**, 4548–4555 (2017).

104. Martínez, Á. *et al.* Mesoporous Silica Nanoparticles Decorated with Carbosilane Dendrons as New Non-viral Oligonucleotide Delivery Carriers. *Chem. - A Eur. J.* **21**, 15651–15666 (2015).

105. Radu, D. R. *et al.* A Polyamidoamine Dendrimer-Capped Mesoporous Silica Nanosphere-Based Gene Transfection Reagent. *J. Am. Chem. Soc.* **126**, 13216–13217 (2004).

106. Lin, Y.-S. *et al.* Well-Ordered Mesoporous Silica Nanoparticles as Cell Markers. *Chem. Mater.* **17**, 4570–4573 (2005).

107. Stöber, W., Fink, A. & Bohn, E. Controlled growth of monodisperse silica spheres in the micron size range. *J. Colloid Interface Sci.* **26**, 62–69 (1968).

108. Huo, Q. *et al.* Organization of Organic Molecules with Inorganic Molecular Species into Nanocomposite Biphase Arrays. *Chem. Mater.* **6**, 1176–1191 (1994).

109. Huo, Q. *et al.* Generalized synthesis of periodic surfactant/inorganic composite materials. *Nature* **368**, 317–321 (1994).

110. Escobar, A. *et al.* Strontium Titanate (SrTiO 3) Mesoporous Coatings for

Enhanced Strontium Delivery and Osseointegration on Bone Implants. *Adv. Eng. Mater.* **21**, 1801210 (2019).

111. Soler-Illia, G. J. a a & Azzaroni, O. Multifunctional hybrids by combining ordered mesoporous materials and macromolecular building blocks. *Chem. Soc. Rev.* **40**, 1107–50 (2011).

112. Vallet-Regi, M., Rámila, A., del Real, R. P. & Pérez-Pariente, J. A New Property of MCM-41: Drug Delivery System. *Chem. Mater.* **13**, 308–311 (2001).

113. Rosenholm, J. M. & Lindén, M. Towards establishing structure-activity relationships for mesoporous silica in drug delivery applications. *J. Control. Release* **128**, 157–164 (2008).

114. Hoffmann, F., Cornelius, M., Morell, J. & Fröba, M. Silica-Based Mesoporous Organic–Inorganic Hybrid Materials. *Angew. Chemie Int. Ed.* **45**, 3216–3251 (2006).

115. Lin, V. S. Y., Lai, C.-Y., Huang, J., Song, S.-A. & Xu, S. Molecular Recognition Inside of Multifunctionalized Mesoporous Silicas: Toward Selective Fluorescence Detection of Dopamine and Glucosamine. *J. Am. Chem. Soc.* **123**, 11510–11511 (2001).

116. Vallet-Regí, M., Balas, F. & Arcos, D. Mesoporous materials for drug delivery. *Angewandte Chemie - International Edition* vol. 46 7548–7558 (2007).

117. Patil, A., Chirmade, U. N., Slipper, I., Lamprou, D. A. & Urquhart, A. Encapsulation of water insoluble drugs in mesoporous silica nanoparticles using supercritical carbon dioxide. *J. Nanomed. Nanotechnol.* **2**, (2011).

118. He, Q., Ma, M., Wei, C. & Shi, J. Mesoporous carbon@silicon-silica nanotheranostics for synchronous delivery of insoluble drugs and luminescence imaging. *Biomaterials* **33**, 4392–4402 (2012).

119. Colilla, M., González, B. & Vallet-Regí, M. Mesoporous silicananoparticles for the design of smart delivery nanodevices. *Biomater. Sci.* **1**, 114–134 (2013).

120. Abstiens, K., Maslanka Figueroa, S., Gregoritza, M. & Goepferich, A. M. Interaction of functionalized nanoparticles with serum proteins and its impact on colloidal stability and cargo leaching. *Soft Matter* **15**, 709–720 (2019).

121. Lee, Y. K., Choi, E. J., Webster, T. J., Kim, S. H. & Khang, D. Effect of the protein corona on nanoparticles for modulating cytotoxicity and immunotoxicity. *Int. J. Nanomedicine* **10**, 97–113 (2014).

122. Fleischer, C. C. & Payne, C. K. Nanoparticle-cell interactions: Molecular

structure of the protein corona and cellular outcomes. *Acc. Chem. Res.* **47**, 2651–2659 (2014).

123. Piella, J., Bastús, N. G. & Puntes, V. Size-dependent protein-nanoparticle interactions in citrate-stabilized gold nanoparticles: The emergence of the protein corona. *Bioconjug. Chem.* **28**, 88–97 (2017).

124. Marichal, L. *et al.* Protein-Nanoparticle Interactions: What Are the Protein-Corona Thickness and Organization? *Langmuir* **35**, 10831–10837 (2019).

125. Waegeneers, N. *et al.* Short-term biodistribution and clearance of intravenously administered silica nanoparticles. *Toxicol. Reports* **5**, 632–638 (2018).

126. Longmire, M., Choyke, P. L. & Kobayashi, H. Clearance properties of nano-sized particles and molecules as imaging agents: considerations and caveats. *Nanomedicine* **3**, 703–717 (2008).

127. Zhang, Y.-N., Poon, W., Tavares, A. J., McGilvray, I. D. & Chan, W. C. W. Nanoparticle–liver interactions: Cellular uptake and hepatobiliary elimination. *J. Control. Release* (2016) doi:10.1016/j.jconrel.2016.01.020.

128. Kermanizadeh, A., Balharry, D., Wallin, H., Loft, S. & Møller, P. Nanomaterial translocation-the biokinetics, tissue accumulation, toxicity and fate of materials in secondary organs-A review. *Crit. Rev. Toxicol.* **45**, 837–872 (2015).

129. Partikel, K. *et al.* Effect of nanoparticle size and PEGylation on the protein corona of PLGA nanoparticles. *Eur. J. Pharm. Biopharm.* **141**, 70–80 (2019).

130. Roig, J. L., Gómez-Vallejo, V. & Gibson, P. N. *Isotopes in Nanoparticles*. *Isotopes in Nanoparticles: Fundamentals and Applications* (Jenny Stanford Publishing, 2016). doi:10.1201/b19950.

131. Budinger, T. F. & Jones, T. *History of Nuclear Medicine and Molecular Imaging*. *Comprehensive Biomedical Physics* (Elsevier B.V., 2014). doi:10.1016/b978-0-444-53632-7.00101-5.

132. Sgouros, G., Bodei, L., McDevitt, M. R. & Nedrow, J. R. Radiopharmaceutical therapy in cancer: clinical advances and challenges. *Nat. Rev. Drug Discov.* **19**, 589–608 (2020).

133. Alsharef, S., Alanazi, M., Alharthi, F., Qandil, D. & Qushawy, M. Review about radiopharmaceuticals: Preparation, radioactivity, and applications. *Int. J. Appl. Pharm.* **12**, 8–15 (2020).

134. International Atomic Energy Agency. Cyclotron Produced Radionuclides : Physical Characteristics and Production Methods. TRS-468. *October* 279 (2009).

135. Dawidczyk, C. M. *et al.* State-of-the-art in design rules for drug delivery platforms: Lessons from FDA-approved nanomedicines. *J. Control. Release* **187**, 133–144 (2014).

136. Wischke, C. & Schwendeman, S. P. Principles of encapsulating hydrophobic drugs in PLA/PLGA microparticles. *Int. J. Pharm.* **364**, 298–327 (2008).

137. Presentato, A. *et al.* Formulation of Mesoporous Silica Nanoparticles for Controlled Release of Antimicrobials for Stone Preventive Conservation. *Front. Chem.* **8**, (2020).

138. Danhier, F. *et al.* PLGA-based nanoparticles: An overview of biomedical applications. *J. Control. Release* **161**, 505–522 (2012).

139. Miyajima, M. The effects of drug physico-chemical properties on release from copoly (lactic/glycolic acid) matrix. *Int. J. Pharm.* **169**, 255–263 (1998).

140. Takeuchi, I., Nomura, K. & Makino, K. Hydrophobic boron compound-loaded poly(l-lactide-co-glycolide) nanoparticles for boron neutron capture therapy. *Colloids Surfaces B Biointerfaces* **159**, 360–365 (2017).

141. Harley, B. A. C. & Yannas, I. V. In Vivo Synthesis of Tissues and Organs. in *Principles of Tissue Engineering* 325–355 (Elsevier, 2014). doi:10.1016/B978-0-12-398358-9.00018-5.

142. Therapies, A. Reflection paper on classification of advanced therapy medicinal products. *Therapy* **44**, 1–19 (2012).

143. Walkey, C. D., Olsen, J. B., Guo, H., Emili, A. & Chan, W. C. W. Nanoparticle Size and Surface Chemistry Determine Serum Protein Adsorption and Macrophage Uptake. *J. Am. Chem. Soc.* **134**, 2139–2147 (2012).

144. Daglar, B., Ozgur, E., Corman, M. E., Uzun, L. & Demirel, G. B. Polymeric nanocarriers for expected nanomedicine: current challenges and future prospects. *RSC Adv.* **4**, 48639–48659 (2014).

145. Bivas-Benita, M., Romeijn, S., Junginger, H. E. & Borchard, G. PLGA-PEI nanoparticles for gene delivery to pulmonary epithelium. *Eur. J. Pharm. Biopharm.* **58**, 1–6 (2004).

146. Wu, C. *et al.* New strategy of efficient inhibition of cancer cells by carborane carboxylic acid-CdTe nanocomposites. *Nanomedicine Nanotechnology, Biol. Med.* **8**, 860–869 (2012).

147. Issa, F., Kassiou, M. & Rendina, L. M. Boron in Drug Discovery: Carboranes as Unique Pharmacophores in Biologically Active Compounds. *Chem. Rev.* **111**, 5701–5722 (2011).

148. Piñón-Segundo, E. *et al.* The emulsification-diffusion method to obtain polymeric nanoparticles. in *Nanoscale Fabrication, Optimization, Scale-Up and Biological Aspects of Pharmaceutical Nanotechnology* 51–83 (Elsevier, 2018). doi:10.1016/B978-0-12-813629-4.00002-4.

149. Leites, L. A. *Vibrational Spectroscopy of Carboranes and Parent Boranes and Its Capabilities in Carborane Chemistry*. *Chemical Reviews* vol. 92 (American Chemical Society, 1992).

150. Rieberer, S. & Norian, K. H. Analytical electron microscopy of Nafion ion exchange membranes. *Ultramicroscopy* **41**, 225–233 (1992).

151. Laskin, A., Cowin, J. P. & Iedema, M. J. Analysis of individual environmental particles using modern methods of electron microscopy and X-ray microanalysis. *J. Electron Spectros. Relat. Phenomena* **150**, 260–274 (2006).

152. Scimeca, M., Bischetti, S., Lamsira, H. K., Bonfiglio, R. & Bonanno, E. Energy Dispersive X-ray (EDX) microanalysis: A powerful tool in biomedical research and diagnosis. *Eur. J. Histochem.* **62**, 89–99 (2018).

153. Fankuchen, I. The Encyclopedia of X-Rays and Gamma Rays. George L. Clark, Ed. Reinhold New York; Chapman and Hall, London, 1963. xxviii + 1149 pp. Illus. $ 35. *Science (80-.).* **142**, 943–943 (1963).

154. Robinson, J. W. *Practical Handbook of Spectroscopy*. *Practical Handbook of Spectroscopy* (Routledge, 2017). doi:10.1201/9780203742433.

155. Henke, B. L., Gullikson, E. M. & Davis, J. C. X-Ray Interactions: Photoabsorption, Scattering, Transmission, and Reflection at E = 50-30,000 eV, Z = 1-92. *At. Data Nucl. Data Tables* **54**, 181–342 (1993).

156. Jeon, J. Review of Therapeutic Applications of Radiolabeled Functional Nanomaterials. *Int. J. Mol. Sci.* **20**, 2323 (2019).

157. Pérez-Medina, C., Teunissen, A. J. P., Kluza, E., Mulder, W. J. M. & van der Meel, R. Nuclear imaging approaches facilitating nanomedicine translation. *Adv. Drug Deliv. Rev.* **154–155**, 123–141 (2020).

158. Gona, K. B., Gómez-Vallejo, V., Padro, D. & Llop, J. [18F]Fluorination of o-carborane via nucleophilic substitution: towards a versatile platform for the preparation of 18F-labelled BNCT drug candidates. *Chem. Commun.* **49**, 11491 (2013).

159. Zheng, Z., Jiang, W., Zinn, A., Knobler, C. & Hawthorne, M. Facile Electrophilic Iodination of Icosahedral Carboranes - Synthesis of Carborane Derivatives with Boron Carbon Bonds Via the Palladium-Catalyzed Reaction of Diiodocarboranes with Grignard-Reagents. *Inorg.*

Chem. **34**, 2095–2100 (1995).

160. Kryska, A. & Skulski, L. One-pot preparations of diaryliodonium bromides from iodoarenes and arenes, with sodium perborate as the oxidant. in *Molecules* vol. 6 875–880 (2001).

161. Llop, J. *et al.* Visualising dual radiolabelled poly (lactide-co-glycolide) nanoparticle degradation in vivo using energy-discriminant SPECT. *J. Mater. Chem. B* 14–16 (2015) doi:10.1039/C5TB01157D.

162. Pérez-Campaña, C. *et al.* Production of 18 F-Labeled Titanium Dioxide Nanoparticles by Proton Irradiation for Biodistribution and Biological Fate Studies in Rats. *Part. Part. Syst. Charact.* **31**, 134–142 (2014).

163. Pérez-Campaña, C. *et al.* Tracing nanoparticles in vivo: a new general synthesis of positron emitting metal oxide nanoparticles by proton beam activation. *Analyst* **137**, 4902–4906 (2012).

164. Bindini, E. *et al.* In Vivo Tracking of the Degradation of Mesoporous Silica through 89Zr Radio-Labeled Core–Shell Nanoparticles. *Small* **17**, (2021).

165. Llop, J. *et al.* In vivo stability of protein coatings on poly lactic co glycolic nanoparticles. *MRS Adv.* **1**, 3767–3773 (2016).

166. Derakhshandeh, K., Karimi, M., Hemati Azandaryani, A., Bahrami, G. & Ghanbari, K. Pharmacokinetic study of furosemide incorporated PLGA microspheres after oral administration to rat. *Iran. J. Basic Med. Sci.* **19**, 1049–1055 (2016).

167. El-Sherbiny, I. M. & Smyth, H. D. C. Controlled release pulmonary administration of curcumin using swellable biocompatible microparticles. *Mol. Pharm.* **9**, 269–280 (2012).

168. Jensen, D. K. *et al.* Design of an inhalable dry powder formulation of DOTAP-modified PLGA nanoparticles loaded with siRNA. *J. Control. Release* **157**, 141–148 (2012).

169. Falciani, C. *et al.* Antimicrobial peptide-loaded nanoparticles as inhalation therapy for Pseudomonas aeruginosa infections. *Int. J. Nanomedicine* **15**, 1117–1128 (2020).

170. Liang, Z., Ni, R., Zhou, J. & Mao, S. Recent advances in controlled pulmonary drug delivery. *Drug Discovery Today* vol. 20 380–389 (2015).

171. Ungaro, F., D'Angelo, I., Miro, A., La Rotonda, M. I. & Quaglia, F. Engineered PLGA nano- and micro-carriers for pulmonary delivery: Challenges and promises. *J. Pharm. Pharmacol.* **64**, 1217–1235 (2012).

172. Yıldız-Peköz, A. & Ehrhardt, C. Advances in pulmonary drug delivery.

Pharmaceutics vol. 12 1–7 (2020).

173. Cossío, U. *et al.* Preclinical evaluation of aerosol administration systems using Positron Emission Tomography. *Eur. J. Pharm. Biopharm.* **130**, 59–65 (2018).

174. Navascuez, M. *et al.* COSAN-stabilised omega-3 oil-in-water nanoemulsions to prolong lung residence time for poorly water soluble drugs. *Chem. Commun.* **56**, 8972–8975 (2020).

175. van der Weide, H. *et al.* Therapeutic Efficacy of Novel Antimicrobial Peptide AA139-Nanomedicines in a Multidrug-Resistant Klebsiella pneumoniae Pneumonia-Septicemia Model in Rats. *Antimicrob. Agents Chemother.* **64**, (2020).

176. Goszczyński, T. M., Fink, K., Kowalski, K., Leśnikowski, Z. J. & Boratyński, J. Interactions of Boron Clusters and their Derivatives with Serum Albumin. *Sci. Rep.* **7**, 9800 (2017).

177. Zaias, J., Mineau, M., Cray, C., Yoon, D. & Altman, N. H. Reference values for serum proteins of common laboratory rodent strains. *J. Am. Assoc. Lab. Anim. Sci.* **48**, 387–390 (2009).

178. He, X. M. & Carter, D. C. Atomic structure and chemistry of human serum albumin. *Nature* **358**, 209–215 (1992).

179. Roche, M., Rondeau, P., Singh, N. R., Tarnus, E. & Bourdon, E. The antioxidant properties of serum albumin. *FEBS Letters* vol. 582 1783–1787 (2008).

180. Garrett, R. H. & Grisham, C. M. *Biochemistry*. *Pressure Vessel Design Manual* (2013). doi:10.1016/B978-0-12-387000-1.01001-9.

181. Pashos, N. . *et al.* Characterization of an Acellular Scaffold for a TE approach to NAC reconstruction. *Cells Tissues Organs* **203**, 183–193 (2017).

182. Bhattacharya, A. A., Grüne, T. & Curry, S. Crystallographic analysis reveals common modes of binding of medium and long-chain fatty acids to human serum albumin 1 1Edited by R. Huber. *J. Mol. Biol.* **303**, 721–732 (2000).

183. Van Beers, B. E., Pastor, C. M. & Hussain, H. K. Primovist, eovist: What to expect? *J. Hepatol.* **57**, 421–429 (2012).

184. Mouthon, L. *et al.* Mechanisms of action of intravenous immune globulin in immune-mediated diseases. *Clin. Exp. Immunol. Suppl.* **104**, 3–9 (1996).

185. Laurens, N., Koolwijk, P. & De Maat, M. P. M. Fibrin structure and wound healing. *J. Thromb. Haemost.* **4**, 932–939 (2006).

186. Chen, Y. Y., Syed, A. M., MacMillan, P., Rocheleau, J. V. & Chan, W. C. W.

Flow Rate Affects Nanoparticle Uptake into Endothelial Cells. *Adv. Mater.* **32**, 1–7 (2020).

187. Klingberg, H., Loft, S., Oddershede, L. B. & Møller, P. The influence of flow, shear stress and adhesion molecule targeting on gold nanoparticle uptake in human endothelial cells. *Nanoscale* **7**, 11409–11419 (2015).

188. Han, J. *et al.* Flow shear stress differentially regulates endothelial uptake of nanocarriers targeted to distinct epitopes of PECAM-1. *J. Control. Release* **210**, 39–47 (2015).

189. Ovais, M. *et al.* Recent advances in the analysis of nanoparticle-protein coronas. *Nanomedicine* **15**, 1037–1061 (2020).

190. Chen, F. *et al.* Complement proteins bind to nanoparticle protein corona and undergo dynamic exchange in vivo. *Nat. Nanotechnol.* **12**, 387–393 (2017).

191. Arima, Y., Kawagoe, M., Toda, M. & Iwata, H. Complement Activation by Polymers Carrying Hydroxyl Groups. *ACS Appl. Mater. Interfaces* **1**, 2400–2407 (2009).

192. Toda, M., Kitazawa, T., Hirata, I., Hirano, Y. & Iwata, H. Complement activation on surfaces carrying amino groups. *Biomaterials* (2008) doi:10.1016/j.biomaterials.2007.10.005.

193. Merle, N. S., Noe, R., Halbwachs-Mecarelli, L., Fremeaux-Bacchi, V. & Roumenina, L. T. Complement system part II: Role in immunity. *Front. Immunol.* **6**, 1–26 (2015).

194. Salacinski, P. R. P., McLean, C., Sykes, J. E. C., Clement-Jones, V. V. & Lowry, P. J. Iodination of proteins, glycoproteins, and peptides using a solid-phase oxidizing agent, 1,3,4,6-tetrachloro-3α,6α-diphenyl glycoluril (Iodogen). *Anal. Biochem.* **117**, 136–146 (1981).

195. Markwell, M. A. K. A new solid-state reagent to iodinate proteins. I. Conditions for the efficient labeling of antiserum. *Anal. Biochem.* **125**, 427–432 (1982).

196. Tolan, D. R. *et al.* Radioiodination of microgram quantities of ribosomal proteins from polyacrylamide gels. *Anal. Biochem.* (1980) doi:10.1016/0003-2697(80)90243-2.

197. Abu Lila, A. S., Shimizu, T. & Ishida, T. PEGylation and anti-PEG antibodies. in *Engineering of Biomaterials for Drug Delivery Systems* 51–68 (Elsevier, 2018). doi:10.1016/B978-0-08-101750-0.00003-9.

198. Shimizu, T. *et al.* Intravenous Administration of Polyethylene Glycol-Coated (PEGylated) Proteins and PEGylated Adenovirus Elicits an Anti-

PEG Immunoglobulin M Response. *Biol. Pharm. Bull.* **35**, 1336–1342 (2012).

199. Hashimoto, Y. *et al.* Generation, characterization and in vivo biological activity of two distinct monoclonal anti-PEG IgMs. *Toxicol. Appl. Pharmacol.* **277**, 30–38 (2014).

200. Vroman, L. & Adams, A. L. Findings with the recording ellipsometer suggesting rapid exchange of specific plasma proteins at liquid/solid interfaces. *Surf. Sci.* **16**, 438–446 (1969).

201. Hirsh, S. L. *et al.* The Vroman effect: Competitive protein exchange with dynamic multilayer protein aggregates. *Colloids Surfaces B Biointerfaces* **103**, 395–404 (2013).

202. Fornaguera, C. *et al.* Interactions of PLGA nanoparticles with blood components: Protein adsorption, coagulation, activation of the complement system and hemolysis studies. *Nanoscale* **7**, 6045–6058 (2015).

203. Mohammad-Beigi, H. *et al.* Strong interactions with polyethylenimine-coated human serum albumin nanoparticles (PEI-HSA NPs) alter α-synuclein conformation and aggregation kinetics. *Nanoscale* **7**, 19627–19640 (2015).

204. Vilela, D. *et al.* Medical Imaging for the Tracking of Micromotors. *ACS Nano* **12**, 1220–1227 (2018).

205. Feiner, I. V. J. *et al.* Pre-targeting with ultra-small nanoparticles: boron carbon dots as drug candidates for boron neutron capture therapy. *J. Mater. Chem. B* **9**, 410–420 (2021).

206. Colilla, M., Balas, F., Manzano, M. & Vallet-Regí, M. Novel method to synthesize ordered mesoporous silica with high surface areas. *Solid State Sci.* (2008) doi:10.1016/j.solidstatesciences.2007.12.009.

207. Slowing, I. I., Trewyn, B. G., Giri, S. & Lin, V. S.-Y. Mesoporous Silica Nanoparticles for Drug Delivery and Biosensing Applications. *Adv. Funct. Mater.* **17**, 1225–1236 (2007).

208. Rosenholm, J. M., Sahlgren, C. & Linden, M. Towards multifunctional, targeted drug delivry systeems using mesoporous silica nanoparticles--opportunities & challenges. *Nanoscale* **2**, 1870–1883 (2010).

209. Karimi, M., Mirshekari, H., Aliakbari, M., Sahandi-Zangabad, P. & Hamblin, M. R. Smart mesoporous silica nanoparticles for controlled-release drug delivery. *Nanotechnol. Rev.* **5**, 195–207 (2016).

210. Tang, C., Russell, P. J., Martiniello-Wilks, R., J. Rasko, J. E. & Khatri, A. Concise review: Nanoparticles and cellular carriers-allies in cancer imaging and cellular gene therapy? *Stem Cells* **28**, 1686–1702 (2010).

211. Floor, S. L., Dumont, J. E., Maenhaut, C. & Raspe, E. Hallmarks of cancer: of all cancer cells, all the time? *Trends Mol. Med.* **18**, 509–15 (2012).

212. Zwicke, G. L., Mansoori, G. A. & Jeffery, C. J. Targeting of Cancer Nanotherapeutics. *Nano Rev.* **1**, 1–11 (2012).

213. Gao, H. *et al.* Ligand modified nanoparticles increases cell uptake, alters endocytosis and elevates glioma distribution and internalization. *Sci. Rep.* **3**, 2534 (2013).

214. Argyo, C., Weiss, V., Bräuchle, C. & Bein, T. Multifunctional mesoporous silica nanoparticles as a universal platform for drug delivery. *Chem. Mater.* **26**, 435–451 (2014).

215. Tornesello, A. L., Tagliamonte, M., Tornesello, M. L., Buonaguro, F. M. & Buonaguro, L. Nanoparticles to improve the efficacy of peptide-based cancer vaccines. *Cancers* vol. 12 (2020).

216. Zhuravlev, L. T. The surface chemistry of amorphous silica. Zhuravlev model. *Colloids Surfaces A Physicochem. Eng. Asp.* **173**, 1–38 (2000).

217. Rahman, I. A., Jafarzadeh, M. & Sipaut, C. S. Synthesis of organo-functionalized nanosilica via a co-condensation modification using γ-aminopropyltriethoxysilane (APTES). *Ceram. Int.* (2009) doi:10.1016/j.ceramint.2008.10.028.

218. Cauda, V., Argyo, C. & Bein, T. Impact of different PEGylation patterns on the long-term bio-stability of colloidal mesoporous silica nanoparticles. *J. Mater. Chem.* **20**, 8693–8699 (2010).

219. He, Q. *et al.* The effect of PEGylation of mesoporous silica nanoparticles on nonspecific binding of serum proteins and cellular responses. *Biomaterials* **31**, 1085–1092 (2010).

220. Shen, Z., Fisher, A., Liu, W. K. & Li, Y. PEGylated 'stealth' nanoparticles and liposomes. in *Engineering of Biomaterials for Drug Delivery Systems: Beyond Polyethylene Glycol* 1–26 (Elsevier, 2018). doi:10.1016/B978-0-08-101750-0.00001-5.

221. Simón-Gracia, L. *et al.* Application of polymersomes engineered to target p32 protein for detection of small breast tumors in mice. *Oncotarget* **9**, 18682–18697 (2018).

222. Shi, S. *et al.* Chelator-Free Labeling of Layered Double Hydroxide Nanoparticles for in Vivo PET Imaging. *Sci. Rep.* **5**, (2015).

223. Pham, A. L.-T., Sedlak, D. L. & Doyle, F. M. Dissolution of mesoporous silica supports in aqueous solutions: Implications for mesoporous silica-based water treatment processes. *Appl. Catal. B Environ.* **126**, 258–264

(2012).

224. He, Q., Shi, J., Zhu, M., Chen, Y. & Chen, F. The three-stage in vitro degradation behavior of mesoporous silica in simulated body fluid. *Microporous Mesoporous Mater.* **131**, 314–320 (2010).

225. Olberg, D. E. *et al.* One Step Radiosynthesis of 6-[18 F]Fluoronicotinic Acid 2,3,5,6-Tetrafluorophenyl Ester ([18 F]F-Py-TFP): A New Prosthetic Group for Efficient Labeling of Biomolecules with Fluorine-18. *J. Med. Chem.* **53**, 1732–1740 (2010).

226. Carvajal-Juarez, I., Monroy-Gonzalez, A., Espinola-Zavaleta, N., Meave-Gonzalez, A. & Alexanderson-Rosas, E. PET/CT with ^{13}N-ammonia. *Ann. Nucl. Cardiol.* **5**, 63–68 (2019).

227. Bindini, E. *et al.* In Vivo Tracking of the Degradation of Mesoporous Silica through 89Zr Radio-Labeled Core–Shell Nanoparticles. *Small* **2101519**, 1–10 (2021).

228. Holland, J. P., Sheh, Y. & Lewis, J. S. Standardized methods for the production of high specific-activity zirconium-89. *Nucl. Med. Biol.* **36**, 729–739 (2009).

Agradecimientos

La curiosidad ha sido desde que recuerdo el motor de mi existencia, la semilla la que mis padres plantaron en mi cabeza y que ha hecho que viva con actitud reflexiva, con curiosidad por el conocimiento cuando encontraba la incertidumbre, tratando de descubrir y desenmarañar la información subyacente en la vida cotidiana. A vosotros os debo este empeño en intentar aportar un pequeño grano de conocimiento, aunque más os debo el cariño, la bondad y el esfuerzo que me siempre habéis transmitido y del cual sois ejemplo de vida. Poco a poco y sin saber muy bien porqué, la cotidianidad fue dejando paso a la Ciencia y más concretamente a la Química, la Biología y la Ciencia de los Materiales.

Me gustaría agradecer a Aitziber López Profesor y a Luis Liz Marzán cp,p Directores Científicos de CIC biomaGUNE por facilitarme poder realizar este trabajo de tesis en estas magníficas instalaciones, por el tremendo esfuerzo realizado para crear este espacio potenciador de talento profesional, científico y personal.

Quiero agradecer sinceramente a mis supervisores de investigación el Dr. Sergio Moya y el Dr. Jordi Llop, por haberme dado la oportunidad de ser parte de vuestro equipo y sobre todo de vuestra familia investigadora, en la cual siempre me he sentido arropado, potenciado y sobre todo motivado para tratar de dar lo mejor de mí. Me he sentido liderado por vosotros, que sois increíbles investigadores a los que admiro por ser ejemplos de inspiración y crecimiento, además de vuestro extenso conocimiento de la ciencia y saber hacer.

Además, me gustaría reflejar mi agradecimiento más profundo a todas las personas que me han acompañado en esta tan duradera aventura. Empezando con aquellas que me han transmitido la ilusión y la pasión del descubriendo. Y esto se remonta a bastantes años atrás, desde mis comienzos en investigadores

en el CBMSO, en el que Gema, Juan, Altea, Kike, Gretel, Marina y Marisa me enseñaron los misterios de la Biología Molecular. Continuando por la Química de los dendrones con Beatriz, y que después continué con mis queridas Blanca y Ana en la Facultad de Farmacia, las cuales considero mis grandes mentoras. Sin olvidarme de la familia del departamento: Eduardo, Marta, Juanlu, Marina, Gonzalo, Fernando, Alejandro, Vicky, Olga, Nati… Gracias de corazón, gracias de viernes en Deportes, de balcones en ca'Fer y los lunes al sol del patio trasero.

También quiero agradecer a todos los compañeros de los laboratorios de Soft Matter y de Radiochemistry y de la sala de "estudio", en especial a Elefthería, Nikos, Echeve, Ane, Angie, Marta, Elisa, Desiré, Zuriñe, Unai, Marcos, Krishna, Ane, Susana, Elena, Idoia, Alessandro, Zuriñe, ... Gracias por acogerme, crear equipo y comunidad que se arropa, se cuida y ser compañeros que crecen y se ayudan.

Con especial cariño, a mis amadas Magdalenas a las que os llevo dentro, por compartir nuestras vidas, nuestros proyecto, ilusiones, retos y lágrimas en la distancia. Y agradezco de todo corazón a todes les amiges del: Colegio, Guadalupe, UCM, UAM, CBMSO… que me habéis acompañado y motivado durante este tiempo, que se os habéis preocupado por mi cuando entendisteis que entre líneas y párrafos perdí el sentido, el rumbo y el tino, mientras mi mente soñaba con días sin pantallas, sin rutinas ni esperanza, y sin embargo ante el insistente titileo de las lámparas, la voluntad empujaba sin apenas saberlo en la hastiada vivencia del día a día. Sois muchos los que me habéis cuidado y os tengo a todos presentes, gracias.

Y termino con mis querides Gema, Jon, Conchita, Tamara, María, Edu, Marta, Oscar y Jose, no tengo palabras para vosotros, nos sobran las cervezas, las miradas, las risas y los abrazos.

A Luismi y a mi Familia.

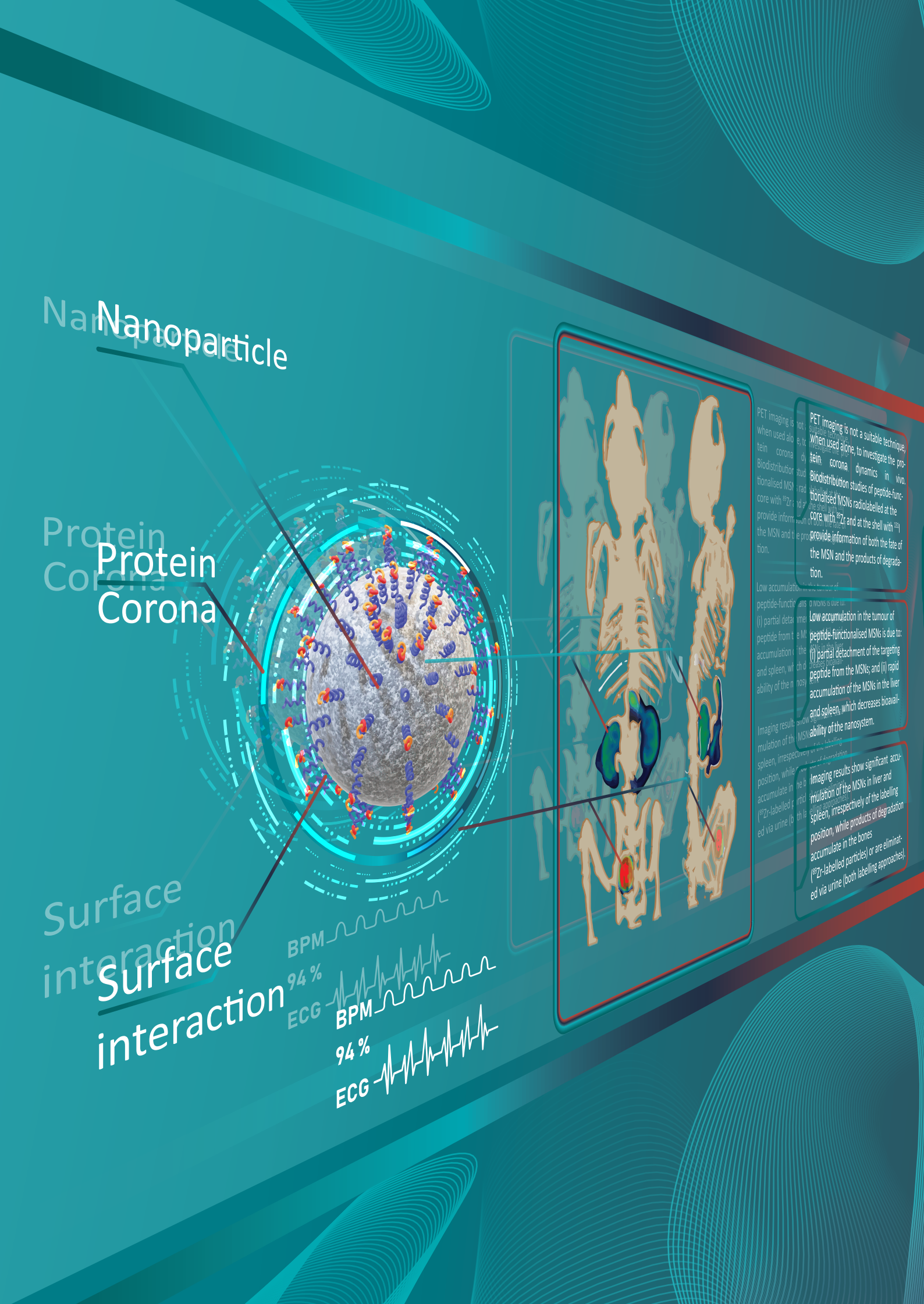
Nanoparticle
Protein Corona
Surface interaction
PET imaging is not a suitable technique, when used alone, to investigate the protein corona dynamics in vivo. Biodistribution studies of peptide-functionalised MSNs radiolabelled at the core with ^{89}Zr and at the shell with ^{131}I provide information of both the fate of the MSN and the products of degradation.
Low accumulation in the tumour of peptide-functionalised MSNs is due to: (i) partial detachment of the targeting peptide from the MSNs; and (ii) rapid accumulation of the MSNs in the liver and spleen, which decreases bioavailability of the nanosystem.
Imaging results show significant accumulation of the MSNs in liver and spleen, irrespectively of the labelling position, while products of degradation accumulate in the bones (^{89}Zr-labelled particles) or are eliminated via urine (both labelling approaches).
BPM
94 %
ECG